Politecnico di Milano
School of Industrial and Information Engineering
Master of Science in Space Engineering
Department of Aerospace Science and Technology

Transferring an Earth Based Adaptive Optics Technology to Space

Advisor: Prof. Lorenzo DOZIO
Co-Advisor: Prof. Paolo MANTEGAZZA

Graduation Thesis of:
Marco BEVILACQUA Matr. 799322

Academic Year 2013-2014

Il lavoro non mi piace, non piace a nessuno,
ma a me piace quello che c'è nel lavoro:
la possibilità di trovare se stessi.

Joseph Conrad

Abstract

The increasing sizes of optical elements in space born telescopes as long as the always higher shape precision requirements have increased the interest in Earth based adaptive optics technologies to be transferred to space field. Active optics for space born telescopes mainly consist of the application of deformable mirror technologies to actively compensate mirrors imperfections and lack of damping, while keeping limited system mass and relaxing surface quality requirements. In the present work a contactless voice-coil actuation technology is adapted and applied to an hypothetical space telescope secondary mirror. Due to the negligible structural damping encountered at cryogenic temperatures, the usual coils current drive has been substituted with voltage one, to provide damping augmentation by means of eddy currents. The control law applied to the surface positioning system is based on a partially centralized Hybrid feedforward term, supported with a decentralized suboptimal feedback. Implementable hardware solutions have been designed and their ability to meet scientific goals has been proved under relevant space environment, overcoming damping and precise positioning problems.

Keywords: voice-coils, voltage drive, damping augmentation, space telescope, suboptimal control, vibration control.

Sommario

Negli ultimi anni le sempre maggiori dimensioni e i sempre più stringenti requisiti di precisione di forma richiesti agli elementi ottici montati su telescopi spaziali hanno fatto aumentare l'interesse verso le tecnologie dell'ottica adattiva, ampiamente utilizzata negli osservatori terrestri, per essere trasferite all'ambito spaziale. L'utilizzo di ottiche "attive" su telescopi orbitanti consiste principalmente nell'utilizzo di specchi a deformazione controllabile per compensare attivamente imperfezioni di forma e sopperire alla quasi assenza di smorzamento strutturale, allo stesso tempo limitando la massa degli specchi stessi e rilassandone i requisiti di finitura superficiale. Nel qui presente lavoro, una tecnologia basata su attuatori elettromagnetici contactless è stata adattata ed applicata ad un ipotetico specchio secondario per telescopio spaziale. A causa della quasi totale assenza di smorzamento strutturale riscontrabile a temperature criogeniche, il consueto controllo in corrente delle bobine degli attuatori è stato sostituito da quello in tensione per sfruttare la dissipazione generata dalle correnti parassite indotte attraverso il moto dello specchio. La legge di controllo utilizzata nel sistema di posizionamento è costituita dal un termine "Ibrido" in anello aperto, parzialmente centralizzato, affiancato da una retroazione sub-ottimale diretta delle misure, totalmente decentralizzata. Sono infine riportati progetti e simulazioni di tre possibili implementazioni elettroniche del sistema di controllo con prestazioni tali da soddisfare i requisiti scientifici posti, sotto condizioni a contorno rappresentative dell'ambiente spaziale, in grado di raggiungere un buon livello di smorzamento indotto ed ottenere un preciso posizionamento della superficie riflettente.

Parole Chiave: attuazione elettromagnetica, controllo in tensione, telescopio spaziale, controllo sub-ottimale, controllo delle vibrazioni.

Contents

List of Figures

List of Tables

Chapter 1

Introduction

This chapter contains a general overview of so-called Active Optics and why it is now considered a key technology for in-space observatories. Then, it follows a bit more detailed explanation of the practical realization of active optics devices, the different available solutions and their operating principle. Finally, the specific problem under investigation in this thesis is presented along with an overview of the adopted design.

1.1 Active optics for space applications

The needs of space observation have pushed towards telescopes with larger apertures. Indeed, this would lead to an increased collecting power and to a wider angular resolution [1], allowing finer observations capable to help scientists answering the more and more numerous questions about the Universe. Two main approaches followed until now in building observatories rely on Earth-based and space-born telescopes [2]. They are briefly described in the following.

The first approach enables the construction of huge optical structures, without tight weight, size or power constraints. Nonetheless, Earth-based telescopes have intrinsic limitations in their observing capabilities due to the presence of the atmosphere that filters all kind of radiation coming from outside and produces electromagnetic waves distortion due to its turbulent nature. Actively deformed optics has been largely studied in this context with two aims:

- correcting static and low frequency deformations caused by extended reflective surfaces subjected to gravity force and wind action;
- rapidly compensating errors in the light wavefront propagating through

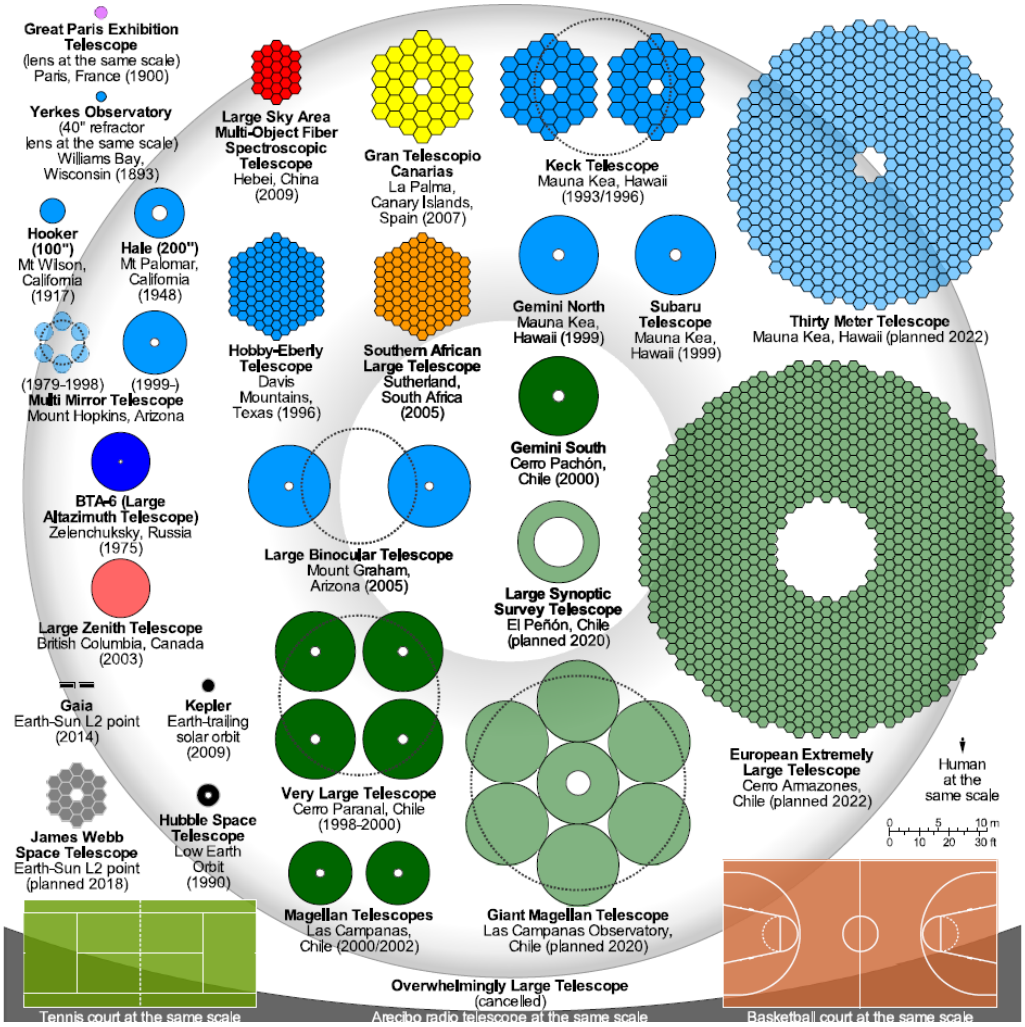

Figure 1.1: Existing and future telescopes size comparison

a turbulent atmosphere.

The control technique is conceptually rather simple. It is based on using a wave front sensor which identifies the level of image distortion. Then an algorithm computes the optimal shape to counteract the phase shifts in the light front. Finally, the corrective shape is applied to the optical surface through an inner control loop governing a set of actuators attached on the rear side of the deformable mirror.

It is clear that the second approach based on space telescopes does not suffer from the above problems since the observatory is outside the atmosphere. On the other hand, this solution presents all typical limitations of space systems. The limited mass that could be launched and inserted in

orbit, as well as the maximum dimensions of spacecrafts allowed by the fairing size of available launchers [3], require advanced technological solutions in order to reach large aperture telescopes. Even if many features of ground based adaptive optics can be exploited in space observatories, it is not always straight forward to adapt them both to the most extreme space operational conditions and to the related more stringent and tight system requirements in terms of reliability, maintainability, radiation tolerance, mass and power consumption. It should be also highlighted that the active control of space telescopes is not only considered as a way of achieving higher demanding performances, but also as an effective solution for relaxing the passive design requirements in terms of polishing of the surfaces and rigidity and thickness of the mirror or for reducing the outage period of missions caused, e.g., by Sun baffle intrusions or eclipses altering the thermal conditions within the instrument. Also this work of thesis can be considered part of the on going development process, presenting the application and adaptation to space environment of Earth based optics control techniques.

Trying to increase the size of the optics, while keeping compactness and low system mass, produces lightweight flexible structures that nevertheless have to maintain their nominal shape, within some prescribed tolerances, in order to guarantee the desired image quality which meets the scientific goals of the mission [1, 4, 5]. In addition, as far as the radiation bandwidth of scientific interest moves towards short wavelengths, the surface tolerances get more and more stringent, reaching nanometric levels. Space environment as well as manufacturing processes and in-space release act against this target by distorting the reflective shell. Furthermore, internal vibrations generated by spacecraft components, thermo-elastic effects arising from changes in the radiation environment, low frequency and static deformations induced by maneuvers or by the passage from a 1g to a micro-gravity condition are all factors that have to be compensated to guarantee the theoretical image quality that an optical system of a certain dimension should ideally achieve [4, 5]. It is anyway necessary to underline that all the above mentioned aberration sources present quite different frequency contents with respect to Earth typical atmospheric turbulence. Indeed, the frequency bandwidth of interest can be reduced from tens of kilo hertz to few hertz. Even the most famous large space observatory, the Hubble Space Telescope, despite it has been designed and developed many years ago, is equipped with a set of 24 force actuators arranged in two concentric circles to make small corrections to the image figure [6].

The limited size of the launcher fairings brought also to the development of deployable and segmented mirrors, which are folded during ascent to orbit and then opened once in space. This is the case of the James Webb Tele-


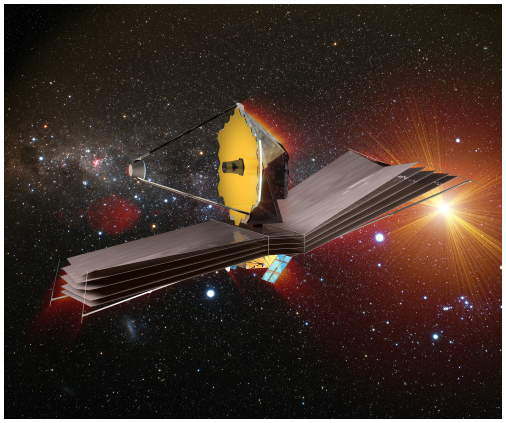

Figure 1.2: Hubble Space Telescope and James Webb Space Telescope

scope, planned to be launched in 2018, which is composed of 18 beryllium segments [7]. Unfortunately, the segmented or deployable solution adds error sources to the correct positioning and shaping of the optical surfaces [3]. All these factors strongly limit the effectiveness of a full passive design and lead to a mixed passive-active approach to shrink the system and obtain at the same time the desired optics stability. A good choice of materials is useful to reduce the mass and limit the thermal deformations, while actuators behind the optical surface keep its shape under control [4].

In the general field of active optics, two main solutions has been found to deal with the image aberrations deriving from non ideal optical surfaces. The first approach involves an active deformation of the primary mirror with a high number of actuators, producing a definitely finer control of the reflected wave front. The second approach, which corresponds to a simpler solution, consists of inserting a secondary pupil actively deformed to compensate the errors generated on the primary surface [4]. The smaller size of the secondary optic system, despite the advantage of requiring a lower number of actuators, introduces challenging volume constraints on the positioning of the mechanisms to actuate the mirror, demanding for smarter and more compact technological solutions.

1.2 Deformable mirrors technology

After providing a general idea of active optics in the previous section, a quick overview of some of the existing hardware technologies that can be and has been used is here presented.

A first classification of continuous facesheet flexible mirrors divides them into monolithic, discrete arrays and bimorph. This classification is strongly linked to the type of actuation used to control the shape, which could be classified into piezoelectric/electrostrictive, electrostatic and electromagnetic [8].

The structure of a monolithic mirror is composed by a thin reflecting surface bonded to the upper side of a single piezoelectric disk. The actuators are defined by an electrode network introduced inside the piezoelectric monolithic disk [9]. The advantages of this solutions are the compactness and the good optical flatness. The main drawback is the low stroke which limits the application of this mirror only to small telescopes. Lead zirconate titanate (PZT) and lead magnesium niobate (PMN) are respectively the most commonly used piezoelectric and electrostrictive materials. Both types of materials present disadvantages; the former shows high hysteresis while the latter nonlinear response and high temperature sensitivity. Both are also used as stack actuators made of individual plates or disks of ferroelectrics material. Further readings on piezoelectric/electrostrictive principle and applications to actuation technologies are suggested to interested readers [10, 11].

In a discrete array deformable mirror the reflective optical plate is assembled on an array of stacked actuators lying on a rigid base plate. This solution is the most widely used. There is a large variety of this kind of mirrors, developed using different actuation technologies. The main characteristics are the number of actuators, the spacing between them, the actuators stroke and voltage and the mirror thickness. The drawbacks of this technology are the large bundles of cables in case of a large number of actuators, the creep inherent to the ferroelectric material, a long lead time and the cost. However, their high reliability, large stroke, excellent accuracy and flexibility in actuators geometry are making this technology the most attractive [12]. The use of discrete and concentrated actuation posed sometimes problems related to local deformations induced on the reflective surface. A solution has been already proposed to avoid those effects by collocating actuators couples on the mirror edges and exploiting torques generated [1, 4]. Within all discrete actuation solutions, electromagnetic actuators are worth to be mentioned. They employ an electric current to generate a magnetic field that reacts against a permanent magnet producing a force. Generally speaking, electromagnetic actuators are built in both linear (voice-coil) and rotational (stepper motor) configurations. Voice-coil deformable mirrors are based on the use of a thin optical shell "floating" on a magnetic field created by a dense array of voice-coil actuators. This is made possible by gluing permanent magnets on the rear face of the thin shell. The actuators are attached on a metallic plate, passing through a thick and very stable glass plate (reference body)

and are facing the magnets attached to the thin shell. To control the shell in position, there is a local contactless capacitive sensor associated with each actuator that measures locally the distance between the rear face of the thin shell and the front face of the reference body. An interesting property of this actuator technology is that, in case of failure of a single actuator, the surrounding ones take over the control of the shell without introducing any print-through effect in the pupil. Intrinsic advantages of this voice-coil actuation concept are: mechanical de-coupling and relaxed tolerances between correcting mirror and reference structure, large stroke, and hysteresis-free behavior. Weak points have been found in the overall complexity, the power consumption, the manufacturing risks, a very long lead time and the cost [12]. However, constant research and development have offered the possibility to largely tackle these problems bringing to energetically efficient solutions and to a robust design [13]. Indeed, in the last decades, voice-coil actuation has been adopted in several AO systems for present and future telescopes (MMT, LBT, VLT, GMT, E-ELT), proving the effectiveness and the advantages of the technology and gaining the high quality standards necessary to deal with the system complexity. Results reached with voice-coil actuation make this technology a promising perspective also for space applications.

Finally, bimorph mirrors are combinations of two materials, the relative sizes of which can be varied through temperature or voltage. They mainly consists of two piezoelectric ceramic wafers, which are bonded together and opposite polarized, parallel to their axis. An array of electrodes is deposited between the two wafers and the application of a voltage changes the area of the electrodes, resulting in a spherical bending of faceplate. The deformation is produced within the plate itself, which needs only to be simply supported to avoid introducing constraints and degrading its deformation capabilities. Bimorph mirrors are sensitive to dimensional changes, including temperature variations and aging. Moreover their structure can not assume a generic shape without changing the boundary conditions [8, 12].

1.3 Voice-coil actuated deformable mirrors for space active optics

The present thesis is focused on the design of a control scheme for the shaping of a voice-coil actuated deformable mirror to be used in a space environment. The aim of the controller is to achieve desired closed-loop performance in terms of surface positioning and response time.

Previous research works [2], part of the ANTASME project, represented

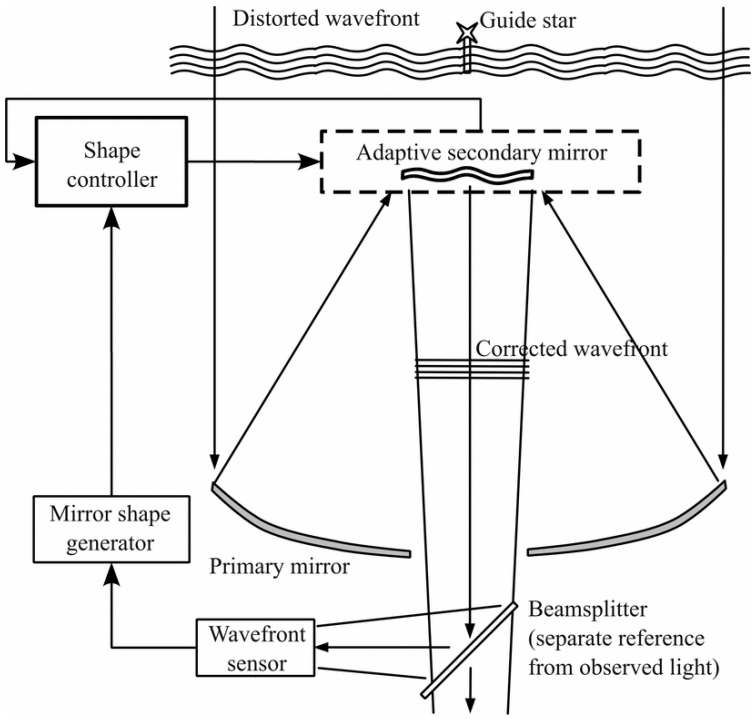

Figure 1.3: An example of adaptive optic control scheme

a solid base for the approach and development of the present project. Indeed the use of adaptive optics has already been integrated in advanced telescopes concepts, despite with different actuation technology. It this sense the present work could be seen as a continuation of these researches.

It is noted that the active image control of mirrors is a wider and more complex system than the present one, since it includes a wave front sensor and a mirror shape generator to drive the control action applied to the shell, as shown in figure 1.3. Should be also said that the development of space telescopes is typically carried out in an integrated and multidisciplinary software environment, because of the strong coupling between all the satellite subsystems and the tight constraints imposed by the extreme scientific goals. The image quality is reached by tuning all the elements of the telescope and exploiting the benefits of different control system and passive design solutions.

According to what mentioned above, this work should be placed at a subsystem level. The aim is to design the inner control loop that forces the mirror to follow the correct shape determined by the mirror shape generator, while ensuring overall system stability and while damping spacecraft internal disturbances, that might not be perceived by the wave front sensor.

To identify plausible system performances and to set realistic goals, the European Space Agency (ESA) announcement for Active Optics development has been taken as reference. It is indeed possible to infer design constraints and objectives from the pertaining documentation [14]. According to ESA, an active optics control system should be capable of correcting typical wavefront errors and reducing the residual error to less than 10 nm rms over the light front. An effective representation of the wavefront and its related errors is through the Zernike modes, widely used in optics, that are simply a sequence of polynomials, orthogonal over the unit circle, expressed in the circular coordinate system. Data from past missions reported typical optical aberrations the system should be able to act against. These data will be further detailed in the following chapter. The European Space Agency also asked for a system capable of applying the correction sequence once a month, but also which is able to generate a continuous correction, with a frequency of 10 Hz, during observation time for L2 missions. The overall system should also guarantee correct operation at cryogenic temperatures. The extrapolated information not only constitutes a benchmark for the system development process, but also assures a concrete perspective for a possible class of applications.

The design of an accurate shape control system for a large deformable structure requires many and distributed control points. As a result, the corresponding control solution is not a trivial task. Since a typical secondary mirror is characterized by a high modal density, the problem becomes even more complex. Contactless force actuators represent also a loss of rigidity on the system. The nature of the problem would suggest the adoption of a centralized control solution. Unfortunately, such physical solution is hard to be achieved in practice when the number of actuator points is large. Indeed, the time required to acquire, process and send back such a high number of channels limits the applicability of a similar scheme, especially if we consider the additional constraints imposed by the space environment on the on-board electronics with respect to both computing capacity of space ready hardware and to power consumption required to perform many computations at a prescribed control frequency.

A simple but effective idea is to properly combine a relatively low-frequency fully or partially centralized feedforward control system with a high-frequency decentralized feedback control law. The feedforward term assures positioning capacity and short time response. The feedback control improves the system stability as well as maintaining a simple and compact realization. Improvements of this control logic has already been proposed by adding dynamic cancellation to the feedforward term to enhance transient behavior during the commanded steps and introducing a hybrid feedforward-feedback

formulation to sharpen the static positioning of the the mirror at the end of the command [15, 16, 17]. The implementation of such scheme should be promising, but its suitability to a space born telescope mirror has to be verified.

The most critical point of such a technological transfer is the always negligible intrinsic structural damping, which is practically nihil at, or closed to, cryogenic temperatures. The absence of an atmosphere makes it miss the possibility to exploit the dissipation effect arising from the air film within the thin free space existing between the mirror and the backshell. It is therefore necessary to find alternatives to introduce damping. The basic idea of this research is to damp out excited modes changing commonly used current-driven voice-coils into voltage-driven ones. The advantage lies in the exploitation of eddy currents induced by the magnets moving with the mirror and not constrained by the current regulator. This solution transforms the voice-coil circuit into a low pass filter, introducing limits on actuation band. Earth based telescopes coils, relying on the air induced damping, opt for current drive [13] in order to obtain the high frequency response required by the turbulence effect, but the space environment lower frequency requirements make this necessity falling. It is thus possible to adopt voltage-drive in space-born telescopes, provided an actuators bandwidth including the interested dynamics.

Chapter 2

Modeling Aspects

This chapter presents the assumptions adopted to derive an adequately reliable mathematical model of the problem under investigation. The first section reports the dynamic model of the mirror structure, coupled with actuators and sensors. The second section deals with the generation of the commands representing the output of an optical correction loop fed back to the shape controller. Finally, a shaping procedure limiting structural dynamics excitation is discussed.

2.1 Dynamic model

One of the first steps has been the development of a suitable numerical model[1] for the simulation of the dynamic behavior of the controlled-uncontrolled mirror response. Since the control design follows a model-based approach, the validity of the shown results is strongly related to the correctness and accuracy of the models used to represent the actual dynamics of the real system and to the real hardware and software implementation. However, it is clear that inevitable approximations have been introduced with respect to the real-life situation. Thus, some modeling solutions have been taken so to allow the identification of borderline and critical cases through an intensive simulation activity. In fact, if the designed control system could meet the given specifications for those critical cases, the actual controller will likely provide further improved results in nominal or less demanding conditions, thus showing acceptable robustness against the more significant modeling uncertainties.

[1] system modeled in MATLAB environment

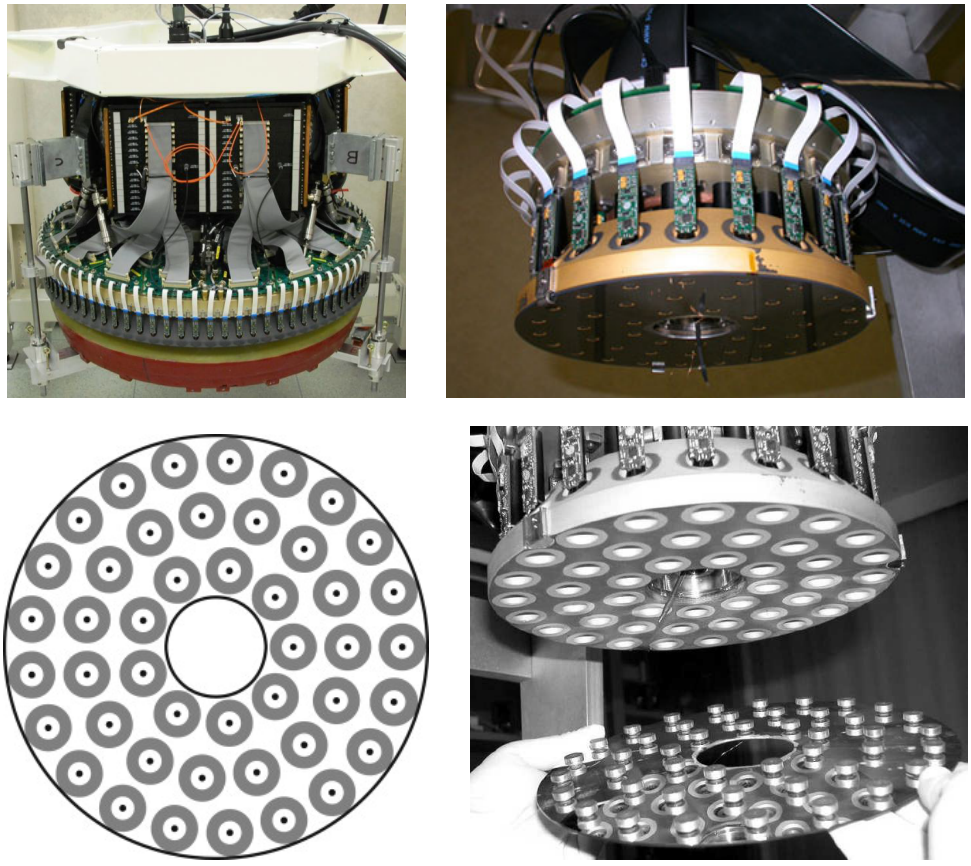

Figure 2.1: P45 prototype [13, 18]

2.1.1 The P45 secondary mirror

The mirror considered in this work is the P45. It is a prototype designed by Microgate and ADS in 2003 during the development phase of LBT672 adaptive secondaries for the LBT telescope. The P45 is a reduced size secondary mirror used to test new technologies, yet it is well representative of the dynamics of a real deformable optic. The mirror is indeed part of an extensive research on voice-coil actuation applied to deformable secondary mirrors for Earth based telescopes and thus of the related development phase. Due to the solution complexity, these applications required the development of sophisticated simulation codes [8, 15, 16, 17, 18]. The possibility to transfer this technology to space telescopes imposes to further extend these simulations in order to properly tackle space characteristic problems. Engineering modeling techniques adopted in these researches constitute a basis for the present work, which aims at adapting them to simulate the mirror behavior

$Material:$	$Zerodur$
$Actuators:$	45
$R_{curvature}:$	2 m
$D_{out}:$	24 cm
$D_{in}:$	$5,67$ cm
$t_{nominal}:$	$1,61$ mm
$M_{mirror}:$	$174,57$ g
$M_{magnets}:$	45 x $2,725$ g

Table 2.1: P45 physical properties

when actuated by voltage-driven voice-coils and without the possibility to exploit the aerodynamic damping effect. In this perspective this thesis could be considered as an extension of the aforementioned works.

The mirror is a thin Zerodur [19] shell with a hole in its center. Zerodur has been widely used for telescope applications due to its low coefficient of thermal expansion, as well as its good structural and optical properties. The shell is actuated by 45 contactless voice-coil motors distributed in 3 concentric circles as shown in figure 2.1. The inner ring has a radius of $4,4$ cm and it is composed of 9 actuators. The middle one counts 15 units and it is placed at $7,58$ cm from the center. Finally, the remaining 21 voice-coils lie on a $10,57$ cm circumference. The nominal design thickness is $1,61$ mm, but manufacturing errors made it growing radially moving towards the outer side. Thus, the mirror has a measured thickness that goes from its nominal value, registered on the innermost part, up to $1,618$ mm on the outer border. The prototype is supported by a membrane connecting it to the backplate at the inner edge. The outer edge is instead free. General properties and characteristics of P45 are summarized in table 2.1.

FEM Model

A detailed Finite Element Model of P45 (fig.2.2) has been already developed in previous studies [8]. The Zerodur shell is modeled in NASTRAN with 8530 triangular plate elements (CTRIA3) defined by 4425 nodes. The different thickness of the mirror has been taken into account by applying different shell properties (PSHELL) to concentric rings of elements. In addition, 45 concentrated masses have been inserted at actuators' positions to represent the glued magnets load effect. The model has been radially constrained at the inner edge to avoid in-plane singularity problems and to well describe the first piston mode frequency of the structure [8]. Vertical elastic elements have been added on the inner edge nodes to represent the stiffness of the central

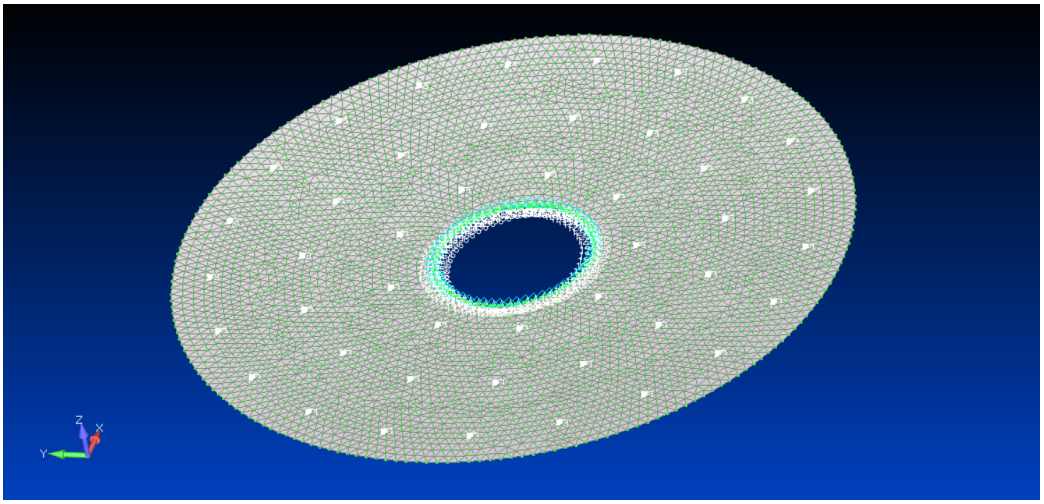

Figure 2.2: FEM model of P45

membrane for a total value of 3660 N/m. The FEM model has been useful to obtain mass and stiffness data to be imported in MATLAB to simulate the structural dynamic behavior of the mirror.

Dynamic model

After denoting as n the number of grid points and n_g the number of degrees of freedom, corresponding to $6 \times n$, a representation of the mirror dynamics in physical coordinates is expressed using matrix notation as follows

$$\mathbf{M}\ddot{\mathbf{s}} + \mathbf{C}\dot{\mathbf{s}} + \mathbf{K}\mathbf{s} = \mathbf{B}_a(\mathbf{f}_c^a + \mathbf{f}_d) \tag{2.1}$$

where $\mathbf{M}$ is the $(n_g \times n_g)$ mass matrix, $\mathbf{C}$ is the $(n_g \times n_g)$ damping matrix, $\mathbf{K}$ is the $(n_g \times n_g)$ stiffness matrix, $\mathbf{f}_c^a$ is the $(n_a \times 1)$ control force vector containing the forces exerted by each actuator at the n_a actuation points and $\mathbf{f}_d$ is the $(n_a \times 1)$ vector containing the disturbance forces condensed at the actuation points. Finally, $\mathbf{B}_a$ is the $(n_g \times n_a)$ force influence matrix projecting the force vectors onto the physical set of degrees of freedom. It should be noted that mass and stiffness matrices could be easily imported from NASTRAN, whereas $\mathbf{C}$ matrix has to be defined properly. In general, the modeling of $\mathbf{C}$ is not a simple problem, but we are lucky enough because it will be almost neglected.

An accurate FE model implies a considerable number of degrees of freedom. Thus, a procedure is necessary to reduce the size of the problem to a computationally acceptable one, especially in view of a control system design. The reduced model should preserve the dynamic content in a prescribed

frequency range such that the system can be simulated in its operational conditions and the presence or absence of spillover effects can be checked. There is a wide variety of condensation techniques available [20, 21], each one having its own advantages and drawbacks.

For the problem at hand, a modal condensation scheme is followed. Provided that some assumptions are verified (see later), this technique allows also a simplified acceptable modeling of the structural damping. Accordingly, the dynamic equations expressed in (2.1) can be written as follows

$$\ddot{q}_i + 2\xi_i\omega_i\dot{q}_i + \omega_i^2 q_i = f_c^{m_i} + f_d^{m_i} \qquad i = 1 : n_g \tag{2.2}$$

where q_i is the i^{th} generalized modal coordinate, ω_i is the i^{th} natural frequency, ξ_i is the damping coefficient associated to the i^{th} mode, while $f_c^{m_i}$ and $f_d^{m_i}$ are respectively the projections of the control and disturbance forces onto the i^{th} mode. Eq. (2.2) is a set of uncoupled equations where unit modal mass has been assumed. If the whole set of modal equations is considered the size of the problem remains unchanged, while the truncation of their number instead leads to a reduced model that can represent, with an adequate accuracy, the system dynamics in a limited frequency range. Considering only n_m modes in the modal transformation, the physical displacement is approximated as

$$\mathbf{s} \simeq \mathbf{\Phi}_g \mathbf{q} \tag{2.3}$$

where $\mathbf{q}$ is the $(n_m \times 1)$ set of n_m selected generalized modal coordinates and Φ_g is the $(n_g \times n_m)$ modal shape matrix of the undamped system. The $(n_m \times 1)$ modal control and disturbance force vectors, $\mathbf{f}_c^m$ and $\mathbf{f}_d^m$, are given, respectively, by

$$\mathbf{f}_c^m = \mathbf{\Phi}_g^T \mathbf{B}_a \mathbf{f}_c^a = \mathbf{\Phi}^T \mathbf{f}_c^a \tag{2.4}$$

$$\mathbf{f}_d^m = \mathbf{\Phi_g}^T \mathbf{B}_a \mathbf{f}_d = \mathbf{\Phi}^{\boldsymbol{T}} \mathbf{f}_d \tag{2.5}$$

where $\mathbf{\Phi}$ is the condensed mode shape matrix. It should be noted that the (i, j) component of this matrix is the displacement of the i^{th} actuator associated to the j^{th} normal mode. It is thus straightforward to write the displacement at the actuation points as

$$\mathbf{u} \simeq \mathbf{\Phi q} \tag{2.6}$$

According to what just explained, a modal analysis in NASTRAN was carried out to extract the natural frequencies and mode shapes at the actuation points. The first 100 modes of the system were thus determined, covering a bandwidth from DC up to 8540 Hz, which is considered to be large enough to verify possible spillovers. The results of this analysis are

reported in table 2.2. The entire set of modes has been used only to simulate both the controlled and the uncontrolled system behavior, whereas a reduced set has been considered for the control design.

Relying on these modal data and after a proper choice of the damping ratio of each mode, the following state space representation of the system in generalized coordinates can be obtained:

$$\begin{Bmatrix} \dot{\mathbf{q}} \\ \ddot{\mathbf{q}} \end{Bmatrix} = \begin{bmatrix} \mathbf{0} & \mathbf{I} \\ -[\diagdown \omega_i^2 \diagup] & -[\diagdown 2\xi_i\omega_i \diagup] \end{bmatrix} \begin{Bmatrix} \mathbf{q} \\ \dot{\mathbf{q}} \end{Bmatrix} + \begin{bmatrix} \mathbf{0} \\ \mathbf{\Phi}^T \end{bmatrix} \mathbf{f}_c^a + \begin{bmatrix} \mathbf{0} \\ \mathbf{\Phi}^T \end{bmatrix} \mathbf{f}_d \tag{2.7}$$

Note that this form is ready for implementation, simulation and control design.

Damping coefficient

One of the most critical issues in structural dynamics is the modeling of damping, i.e., the formulation of damping matrix $\mathbf{C}$ in Eq. (2.1) or the evaluation of the modal damping coefficients ξ_i in Eq. (2.2). There exists an extensive literature about structural damping [22], but only the adopted solution is here reported.

The modeling approach consists of directly imposing a lightly damped structure so that the modal damping matrix becomes a diagonal matrix of this form

$$\mathbf{C}_q = [\diagdown 2\xi_i\omega_i \diagup] \tag{2.8}$$

where the damping coefficient ξ_i is associated with the i^{th} mode. This method has the advantage of introducing a dissipation effect directly on the modal representation. Furthermore, the set of damping parameters ξ can be estimated experimentally through a modal testing procedure.

The code implemented in this work allows a modal damping representation, by setting a unique damping coefficient ξ for all modes.

Regarding the P45 model, it is a rather difficult task to find a reliable value for the damping coefficients, as no experimental data are available. Furthermore, even if an estimation of damping was available from ground modal testing data, the corresponding damping values would result useless since the absence of atmosphere in space environment drastically changes the dissipation effects in the problem under investigation.

The adopted solution was to directly introduce modal damping by estimating its value with Zener damping theory. According to the literature, it is known that the Zener theory can produce good estimates of damping levels only at room temperature. The estimation is more and more inaccurate as the temperature decreases [23, 24, 25]. Very little information is today

Mode	**Freq.** [Hz]	**Mode**	**Freq.** [Hz]	**Mode**	**Freq.** [Hz]
1	5.75	35	2474.92	69	5447.50
2	5.75	36	2699.34	70	5450.45
3	17.61	37	2699.79	71	5973.51
4	130.08	38	2768.21	72	5974.79
5	130.09	39	2840.73	73	6237.61
6	313.67	40	2841.38	74	6241.41
7	313.71	41	3022.05	75	6325.64
8	479.10	42	3022.88	76	6326.87
9	551.80	43	3467.33	77	6340.13
10	551.89	44	3468.03	78	6340.70
11	623.27	45	3477.55	79	6413.08
12	623.39	46	3491.72	80	6414.43
13	845.38	47	3492.33	81	7020.22
14	845.59	48	3710.65	82	7021.06
15	942.26	49	3711.20	83	7138.37
16	942.38	50	4146.36	84	7139.44
17	1193.02	51	4148.57	85	7265.18
18	1193.15	52	4428.86	86	7268.18
19	1237.49	53	4430.10	87	7455.27
20	1352.48	54	4542.73	88	7457.08
21	1352.55	55	4545.16	89	7930.99
22	1488.95	56	4775.26	90	7932.77
23	1489.05	57	4776.56	91	7961.73
24	1590.37	58	4868.22	92	7964.06
25	1590.47	59	4869.85	93	7993.23
26	1853.53	60	5124.74	94	7998.73
27	1853.81	61	5136.11	95	8018.92
28	2027.68	62	5136.36	96	8021.11
29	2028.05	63	5259.05	97	8089.83
30	2028.49	64	5260.22	98	8202.86
31	2028.84	65	5412.90	99	8204.88
32	2411.91	66	5413.57	100	8538.90
33	2412.56	67	5429.99		
34	2474.24	68	5431.62		

Table 2.2: First 100 modes of P45 fem model

available on cryogenic effects on damping in materials, yet the interest is rapidly growing since new generation telescopes are going to work at such temperatures. What is commonly known is that the material damping could be several order of magnitude lower at few Kelvin than at room temperature [26], thus could be assumed practically null. To enhance the knowledge in this field, the Jet Propulsion Laboratory (JPL) built a Cryogenic Material Damping Testbed, whose aim is to find materials exhibiting a relevant damping level at low temperatures, rather than to characterize directly the damping values. Indeed, the damping level of a structure is not only associated to the material, but is related to the shape of the components, their assembly and joints. It would thus be unrealistic trying to find a damping value without having a representative model or prototype to be tested in realistic environment [23, 24, 25]. The results, apart from confirming the bad Zener theory accuracy at low temperatures, evidenced that, even the highest values found remained a negligible fraction of a useful structural damping level. Indeed these studies, e.g., reported values of ξ between 2×10^{-5} and 8×10^{-5} for beryllium, between 0.74×10^{-5} and 1.8×10^{-5} for Alloys and between 1.9×10^{-5} and 6.7×10^{-5} for Silicon/Silicon Carbide foams [23, 25].

Zener theory relates damping coefficient ξ to temperature, material properties, thickness of the sample, and vibration frequency as follows

$$\xi = \frac{\alpha^2 E T}{2 C_p \rho} \left[\frac{\omega \tau}{1 + (\omega \tau)^2} \right] \tag{2.9}$$

with

$$\tau = \frac{C_p h^2 \rho}{k \pi^2}$$

were α is the coefficient of thermal expansion [1/K], h is specimen thickness [m], E is the elastic modulus [N/m^2], T is temperature [K], C_p is specific heat [J/kg/K], k is thermal conductivity [W/m/K], ρ is density [kg/m^3], $\omega = 2\pi f$ is the vibration frequency [rad/s] and τ is the relaxation time [s/rad].

Since the above formulation is a fast way of recovering a plausible value of ξ and the structural damping is for sure lower than a desired value and several order of magnitude lower than the electric damping introduced by the voltage-driven voice-coil actuators (see later), the result of Zener theory has been considered only as a representative estimate of a negligible damping. Taking all needed information from Zerodur datasheet [19] and recovering data from FE mirror model it has been possible to set structural damping to $\xi = 1.5835 \times 10^{-8}$, that is even a conservative value. It is anyway evident the necessity to exploit alternative ways to damp vibrations.

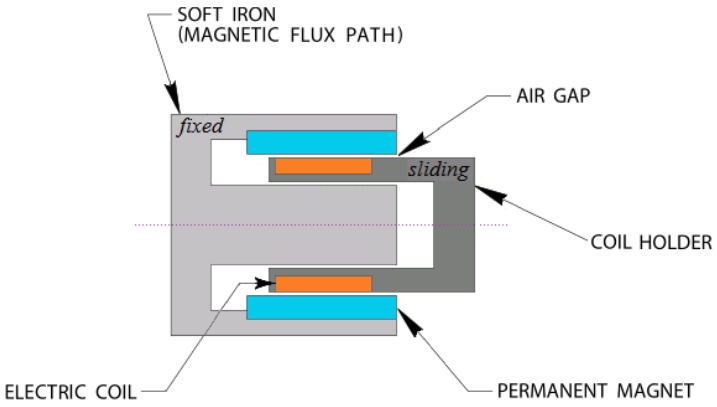

Figure 2.3: Typical voice-coil section

2.1.2 Voice-coil linear actuators

Voice-coils are very simple and smart linear force actuators, based on electromagnetic principles. The basic idea is to create a force by submitting a current-carrying conductor to a magnetic field. In its simplest form, a voice-coil is nothing more than a tubular winding of wire situated within a radially oriented magnetic field [27]. The force generated will be proportional to the number and length of turns of the wire, as well as to the current flowing and to the magnetic filed strength.

Another important effect is that a conductor moving in a magnetic field will be also subjected to a voltage difference across its length. This actually happens also in voice-coils. The coil motion, either it is induced by Lorentz force or by an outside mechanical action, produces what is commonly known as counter-electromotive force (emf). Despite the name, it is a voltage per unit speed.

The current flow in the coil causes also heat generation by joule effect, that has to be dissipated. The ratio of the force exerted by the actuator and the power lost gives an estimate of the motor efficiency. The parameter expressing this ratio is called motor constant.

In the actuation field, the voice-coil technology shows many advantages compared to other solutions such as zero hysteresis behavior, direct drive and thus absence of backlash, low moving mass, very good force linearity and high precision positioning. The main drawbacks are limited stroke, need for cooling of the circuit, the need to keep a current flowing [28].

A design solution commonly adopted in voice-coil motors involves a permanent magnet generating a magnetic field which is driven by a ferromagnetic path to orient radially in the free gap where the coil is included, as

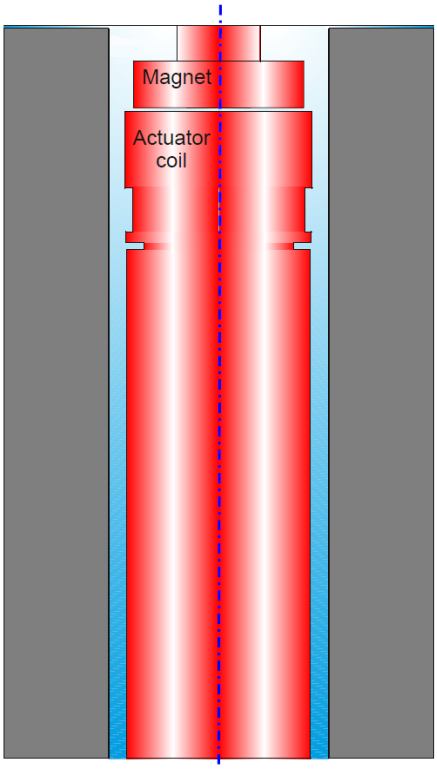

Figure 2.4: Adopted actuator scheme

L	2 mH
R	40 Ω
ω_{cut}	20000 rad/s
F	± 0.1 N
K_m	0.4 N/$\sqrt{\text{W}}$
K_t	2.53 N/A

Table 2.3: Actuator data

shown in figure 2.3. The coil is mounted on a cylindrical support. Forcing a current flowing in the winding produces a force exchange between the coil support the magnet mounting.

The configuration here proposed, used in massively actuated mirrors, exhibits instead a compact design. The magnet is directly glued on the rear face of the mirror and the winding are mounted on a tapered stick fixed to the reference body (fig 2.4). The magnetic field distribution has been studied to cross the coil with correct orientation around a nominal position, despite this solution clearly limits the linear behavior to small displacements. The backplate acts also as heat sink for power dissipation.

To describe the actuation performances and the electrical and physical characteristics of such a class of devices, the following parameters must be introduced:

- S the stroke [m]
- F the maximum force [N]

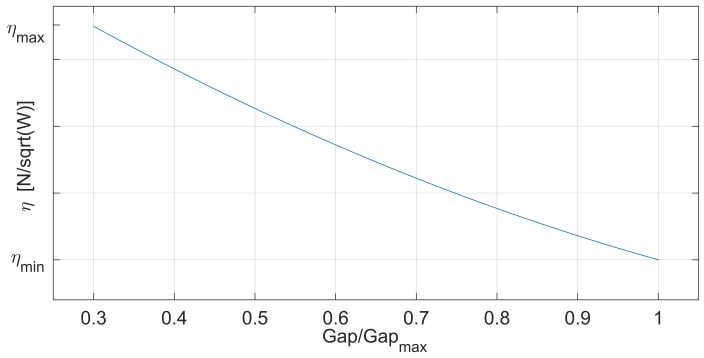

Figure 2.5: Efficiency vs Gap

- K_t the force constant [N/A]
- K_e the back emf constant [Vs/m]
- R the terminal resistance [Ω]
- L the terminal inductance [H]
- P_l the power losses [W]
- $K_m = F/\sqrt{P_l} = K_t/\sqrt{R} = \eta$ the motor constant (or efficiency) [N/$\sqrt{\text{W}}$]

Most of these characteristics are usually expressed at the mid stroke, but their value changes with position, so modifying the actuator performance along its stroke. The efficiency trend, e.g., is reported in figure 2.5.

The circuit representing the electric dynamics of the device is reported in figure 2.6 and its mathematical model is described in the following scalar equations:

$$L\frac{di}{dt} + Ri + K_e\dot{u} = V \tag{2.10}$$

$$F = K_t i \tag{2.11}$$

The actuator data are reported in Table 2.3. When the voice-coil actuator is current-driven, the electrical dynamics of the actuator is by-passed. As a result, the amplitude of the forcing current directly controls the intensity of the actuator force, due to the proportionality relation expressed in Eq. (2.11).

In this thesis, a voltage-driven solution is proposed. The electric circuit acts as a low pass filter with a cutoff frequency equal to

$$f_{cut} = \frac{R}{2\pi L} \tag{2.12}$$

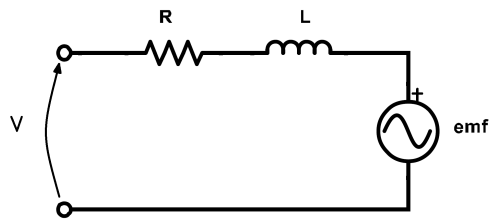

Figure 2.6: Voice-coil circuit

that anyway does not constitute a limitation due to the low command bandwidth in space telescopes. Furthermore, the back emf introduces a sort of feedback voltage, that dynamically represents an additional damping term on the mirror structure. The Laplace transform of Eq. (2.10) brings to

$$i = \frac{1}{L\,s + R}\left[-K_e \dot{u} + V\right] \tag{2.13}$$

Neglecting for a while the command voltage V it can be noticed how from the presence of RL filter in front of the velocity term, back emf action results dominated by damping at low frequencies, but constitutes a stiffness term at the higher ones.

Approximating the transfer function with a quasi-static representation it is possible to write the expansion

$$\frac{1}{L\,s + R} \approx \frac{1}{R} - \frac{L}{R^2}\,s + \frac{L^2}{R^3}\,s^2 + ... \tag{2.14}$$

that could be truncated at the desired order.

It has thus been possible verifying, by means of a residualization procedure, the electric dynamics dominant term. Eq. (2.14) allows thus the approximation of the current flowing to

$$i \approx -\frac{K_t}{R}\dot{u} + \frac{K_t L}{R^2}\ddot{u} + \frac{1}{L\,s + R}\,V \tag{2.15}$$

where the control voltage has been kept in its exact form, in order to avoid complicated pseudo-derivatives of the incoming signal, whereas the back emf approximation has been arrested to the first order to avoid a third order differential equation. It is immediate observing that the introduced damping is definitely greater than the structural damping available. System response to smooth voltage step sequences have been simulated for two different approximation orders of the current expression terms and compared to the response of a system containing the exact electrical dynamics. The results, reported

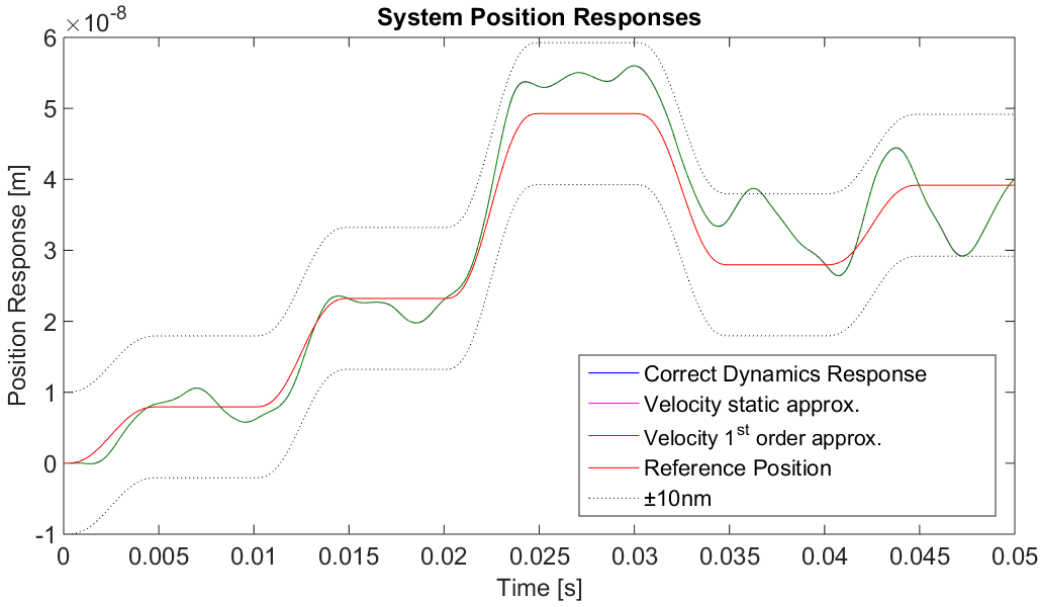

Figure 2.7: Approximate and exact system responses

in figures 2.7 and 2.8, clearly evidence how the the velocity feedback could be mainly represented with its static expression, being the relative error less than 0.1nm, that is sufficiently below the resolution level investigated in this thesis. In addition, a first order expansion seems not presenting greater accuracy. This proves that the interested structural dynamic lays largely below the circuit cutoff frequency. It is thus admissible approximating the equivalent force action as

$$\mathbf{f}_{emf} \approx -\frac{K_t^2}{R}\dot{\mathbf{u}} = -\eta^2\dot{\mathbf{u}}$$

This expression can be used in Eq. (2.1), that can be then divided by the concentrated mass m_i, equivalent to the relative fraction of mirror mass augmented by the mass of a magnet.

$$m_i = \frac{M_{mirr}}{n_{act}} + m_{mgn} = \frac{174,57\text{g}}{45} + 2,73\text{g} = 6,61\text{g}$$

Exploiting then a mass normalized modal transformation, under the assumption of lightly damped structure, it is possible to arrive to the approximate system

$$\ddot{\mathbf{q}} + [\diagdown 2\xi_i\omega_i \diagup]\,\dot{\mathbf{q}} + \left[\diagdown\, \eta^2/m_i \diagup\right]\dot{\mathbf{q}} + [\diagdown \omega_i^2 \diagup]\mathbf{q} = \mathbf{\Phi}^T\mathbf{f} \tag{2.16}$$

where also the induced modal damping matrix has been assumed diagonal and proportional to the ratio η^2/m_i. Considering only the dominant contri-

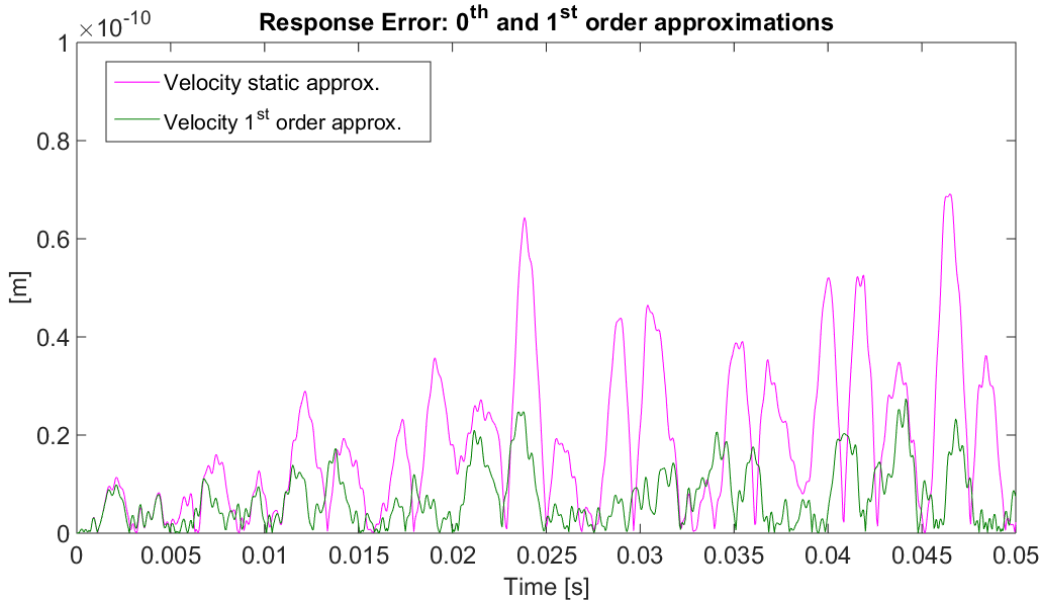

Figure 2.8: Solution error for different approximation orders

bution of the induced damping matrix, from structural damping expression it derives

$$\xi_{emf} = \frac{\eta^2}{2\omega_i m_i} = \frac{\eta^2}{4\pi f_i m_i} \tag{2.17}$$

that shows a linear trend decreasing with frequency. It is thus possible to quantitatively find an estimated value for the damping produced by the eddy currents. Conservatively taking the lower value of η (figure 2.5), it can be found

$$\xi_{emf} = \frac{(0,35)^2}{4\pi\ 0,00661}\frac{1}{f_i} = \frac{1,47}{f_i}$$

This trend shows a damping level of about $\xi = 0.147$ at a frequency of 10Hz, that linearly decrease to $\xi = 0.0147$ at 100Hz and to $\xi = 1,47\times10^{-3}$ at 1kHz. These values, even if found using rough approximations, put in evidence the relevant increase in the damping value, at least in the low interested frequency range, that could be obtained by exploiting voltage-driven voice-coils. The behavior of ξ_{emf} imposes to verify the absence of spillover in high frequency modes that take less advantage from the eddy currents effect. These passages constitute thus a relevant basis for starting a control design process.

Finally in the state space representation of the overall system, the follow-

ing equations were added

$$\begin{aligned} d\mathbf{i}/dt &= -[\tfrac{R}{L}]\,\mathbf{i} - \tfrac{K_e}{L}\,\mathbf{\Phi}\,\dot{\mathbf{q}} + [\tfrac{1}{L}]\,\mathbf{V} \\ \mathbf{f}_c^a &= [K_t]\,\mathbf{i} \end{aligned} \tag{2.18}$$

where the vectors $\mathbf{i}$ and $\mathbf{V}$ contains respectively the currents flowing and the voltages applied at each actuator.

2.1.3 Sensors and signal processing

One of the key aspects of using force actuators to control in closed loop the correct shape of the mirror is the intrinsic need for a position measure. The sensors chosen for this application are capacitive sensors.

This technology fits well with voice-coil actuators as it is contactless too. Each actuator has a co-located coupled sensor. Due to space limitation, the measure cannot be physically taken in the same exact location of the actuation point. The solution adopted in practice involves a capacitive element in the form of a circular corona placed around the actuation point. This realization induces errors due to the non precise co-location of the measure and the actuation and also to the distributed nature of the capacitive elements, that suffers from spatial sampling errors when wavy spatial deformations are commanded. As these aspects can be considered just as small errors in the measurement process with respect to an ideal co-located point measure, for the sake of simplicity both co-location and point wise measurements have been assumed in the model, which was then subjected to measurement noise representing the above mentioned discrepancies with respect to the ideal case.

The sensor dynamics has been approximated as a first order filter, that in Laplace domain is given by

$$u_m = \frac{b}{b+s}\,u \tag{2.19}$$

where u_m is the measured position at the actuation point and b is the pole of the transfer function, which can be a design parameter. Actually, the distributed nature of the annular capacitive sensor acts as a filter on the ideal position measures [8]. The cutoff frequency has to be selected high enough to follow the system response, but not too high in order to help avoiding spillover effects on high frequency structural modes. In the time domain, the state space representation of the array of capacitive sensors is

$$\begin{aligned} \dot{\mathbf{u}}_m &= -[b]\,\mathbf{u}_m + [b]\,\mathbf{u} \\ \mathbf{y}_u &= \mathbf{I}\,\mathbf{u}_m + \mathbf{I}\,\mathbf{n} \end{aligned} \tag{2.20}$$

where $\mathbf{y}_m$ is the vector of sensors outputs and $\mathbf{n}$ is the measurements noise vector.

Once a measure of position is available, it is possible to compute also its derivative and integral, thus implementing a PID controller. Broadly speaking, it is thus possible to feedback both the position variable to increment the structural stiffness of the system, and the corresponding velocity variable to introduce a damping effect. The integral term could help in reducing the steady state error.

The derivative action has been introduced via a pseudo differentiator of this form

$$y_v = \frac{a\,s}{a+s} = y_u \tag{2.21}$$

where a is the differentiator pole. Also in this case, the parameter a represents a design variable that affects the control system performance. To switch to a state space representation, it is necessary to introduce an additional state variable z such that

$$\frac{y_v}{y_u} = \frac{y_v}{z}\frac{z}{y_u} = s\frac{a}{a+s}$$

This yields

$$\begin{aligned} \dot{z} &= -az + ay_u \\ y_v &= \dot{z} \end{aligned} \tag{2.22}$$

Then, grouping all the signals,

$$\begin{aligned} \dot{\mathbf{z}} &= -[\diagdown a \diagup]\,\mathbf{z} + [\diagdown a \diagup]\,\mathbf{y}_u \\ \mathbf{y}_v &= -[\diagdown a \diagup]\,\mathbf{z} + [\diagdown a \diagup]\,\mathbf{y}_u \end{aligned} \tag{2.23}$$

Following the same procedure as for the differentiator, the integral of position is first expressed as

$$J = \int y_u\,dt$$

Deriving this equation yields

$$\dot{J} = y_u \tag{2.24}$$

which is written in the Laplace domain as

$$J = \frac{1}{s}\,y_u \tag{2.25}$$

The corresponding state space representation of the grouped signals is given by

$$\begin{aligned} \dot{\mathbf{J}} &= \mathbf{I}\,\mathbf{y}_u \\ \mathbf{y}_i &= \mathbf{I}\,\mathbf{J} \end{aligned} \tag{2.26}$$

2.1.4 State space representation

The overall state space model results from collecting all the elements introduced in the previous sections. Using Eqs. (2.7), (2.6), (2.18), (2.20), (2.23) and (2.26), the state space representation reads

$$\begin{Bmatrix} \dot{\mathbf{q}} \\ \ddot{\mathbf{q}} \\ d\mathbf{i}/dt \\ \dot{\mathbf{u}}_m \\ \dot{\mathbf{z}} \\ \dot{\mathbf{J}} \end{Bmatrix} = \begin{bmatrix} \mathbf{0} & \mathbf{I} & \mathbf{0} & \mathbf{0} & \mathbf{0} & \mathbf{0} \\ -[\diagdown \omega_i^2 \diagup] & -[\diagdown 2\xi_i\omega_i \diagup] & K_t\mathbf{\Phi}^T & \mathbf{0} & \mathbf{0} & \mathbf{0} \\ \mathbf{0} & -\frac{K_e}{L}\mathbf{\Phi} & -[\diagdown \frac{R}{L} \diagup] & \mathbf{0} & \mathbf{0} & \mathbf{0} \\ b\mathbf{\Phi} & \mathbf{0} & \mathbf{0} & -[\diagdown b \diagup] & \mathbf{0} & \mathbf{0} \\ \mathbf{0} & \mathbf{0} & \mathbf{0} & [\diagdown a \diagup] & -[\diagdown a \diagup] & \mathbf{0} \\ \mathbf{0} & \mathbf{0} & \mathbf{0} & \mathbf{I} & \mathbf{0} & \mathbf{0} \end{bmatrix} \begin{Bmatrix} \mathbf{q} \\ \dot{\mathbf{q}} \\ \mathbf{i} \\ \mathbf{u}_m \\ \mathbf{z} \\ \mathbf{J} \end{Bmatrix} + \\ + \begin{bmatrix} \mathbf{0} \\ \mathbf{0} \\ [\diagdown \frac{1}{L} \diagup] \\ \mathbf{0} \\ \mathbf{0} \\ \mathbf{0} \end{bmatrix} \mathbf{V} + \begin{bmatrix} \mathbf{0} \\ \mathbf{\Phi}^T \\ \mathbf{0} \\ \mathbf{0} \\ \mathbf{0} \\ \mathbf{0} \end{bmatrix} \mathbf{f}_d + \begin{bmatrix} \mathbf{0} \\ \mathbf{0} \\ \mathbf{0} \\ \mathbf{0} \\ [\diagdown a \diagup] \\ \mathbf{I} \end{bmatrix} \mathbf{n}$$

$$\begin{Bmatrix} \mathbf{y}_u \\ \mathbf{y}_v \\ \mathbf{y}_i \end{Bmatrix} = \begin{bmatrix} \mathbf{0} & \mathbf{0} & \mathbf{0} & \mathbf{I} & \mathbf{0} & \mathbf{0} \\ \mathbf{0} & \mathbf{0} & \mathbf{0} & [\diagdown a \diagup] & -[\diagdown a \diagup] & \mathbf{0} \\ \mathbf{0} & \mathbf{0} & \mathbf{0} & \mathbf{0} & \mathbf{0} & \mathbf{I} \end{bmatrix} \begin{Bmatrix} \mathbf{q} \\ \dot{\mathbf{q}} \\ \mathbf{i} \\ \mathbf{u}_m \\ \mathbf{z} \\ \mathbf{J} \end{Bmatrix} + \begin{bmatrix} \mathbf{I} \\ [\diagdown a \diagup] \\ \mathbf{I} \end{bmatrix} \mathbf{n} \tag{2.27}$$

In a more compact matrix notation, it can be expressed as follows

$$\begin{aligned} \dot{\mathbf{x}} &= \mathbf{A}\mathbf{x} + \mathbf{B}\mathbf{V} + \mathbf{B}_d\mathbf{f}_d + \mathbf{B}_n\mathbf{n} \\ \mathbf{y} &= \mathbf{C}\mathbf{x} + \mathbf{D}_n\mathbf{n} \end{aligned} \tag{2.28}$$

The matrices $\mathbf{A}$, $\mathbf{B}$, $\mathbf{B}_d$, $\mathbf{B}_n$, $\mathbf{C}$, and $\mathbf{D}_n$ are required both to simulate the open-loop and closed-loop time response of the space mirror and to design the control system.

2.2 Mirror shape generator

The last block of the model of the system involves a generator of random shapes to be imposed to the mirror shell. Actually, the optical control loop

Mode	**Max. Amplitude (rms) [nm]**
Coma3	300
Astigmatism3	200
Spherical3	75
Trefoil5	50
Astigmatism5	50
Tetrafoil7	50
Trefoil7	50
Pentafoil9	50
Tetrafoil9	50

Table 2.4: Typical optical aberrations registered

is not entirely modeled in this work and representative reference input corresponding to reference shapes of the mirror have to be somehow introduced to test the effectiveness of the proposed control architecture.

A MATLAB script capable of producing a desired command history to each actuator has been coded. Inside the code, it is possible to set the command frequency, which should be 10Hz as required by ESA. However, the command rate can be increased or decreased to test the limiting capabilities of the control system.

Another important option which can be selected is the space and time correlation between the different reference inputs, that is the characteristic of the sequence of imposed shapes. Also in this case, the program offers various alternatives spacing from purely random shapes to single mode shape excitation. A completely random distribution of positions would be for sure the worst excitation case as it would involve all the modal shapes. Another possibility is to generate a monotonically growing sequence of random steps. This would emphasize steady state errors proportional to the amplitude of the input. Alternatively, a command sequence oscillating between two positions is an input that tries to force the system to oscillate. It is also possible to feed the mirror with a single step to verify the step response. Otherwise, as previously mentioned, a single modal shape can be forced by taking its characteristics from modal analysis. Finally, the most realistic input is constituted by a random linear combination of Zernike polynomials with amplitudes tuned to typical distributions of optical aberrations [14]. These latter data, recorded by previous missions, are summarized in table 2.4. As Zernike modes resemble the structural modes of a circular shell, the latter has been used by looking for the equivalence between the two set of spatial forms (fig. 2.9).

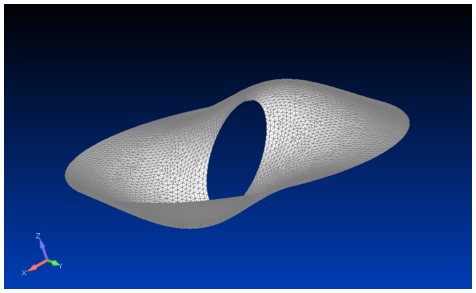

(a) $Modes 11, 12$ (623Hz) $\simeq Coma3$

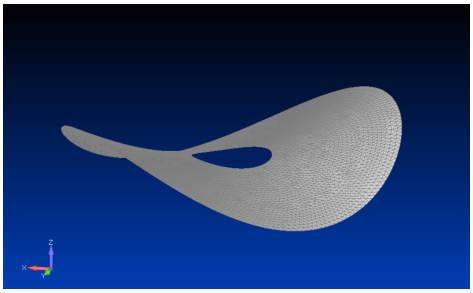

(b) $Modes\ 4, 5$ (130Hz) $\simeq Astigm.3$

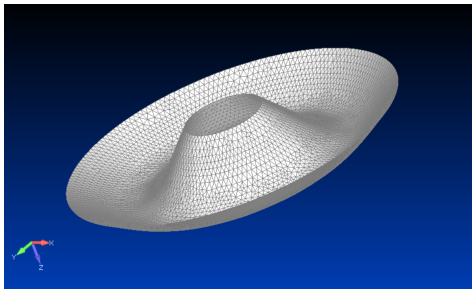

(c) $Mode\ 19$ (1237Hz) $\simeq Spherical3$

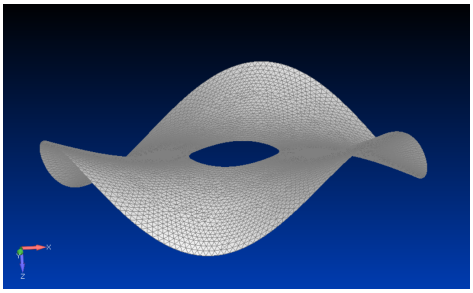

(d) $Modes\ 6, 7$ (313Hz) $\simeq Trefoil5$

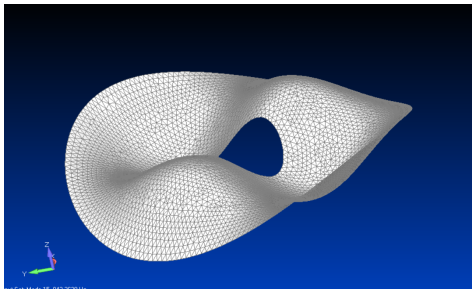

(e) $Modes\ 15, 16$ (942Hz) $\simeq Astigm.5$

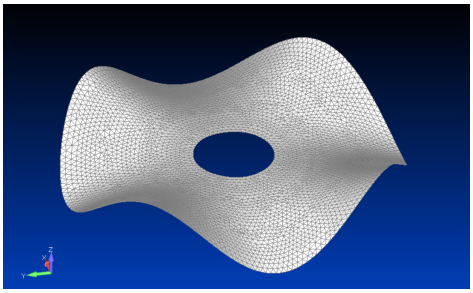

(f) $Modes\ 9, 10$ (551Hz) $\simeq Tetrafoil7$

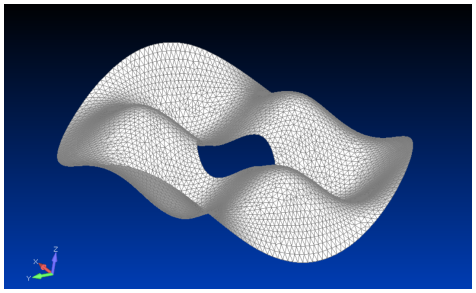

(g) $Modes\ 20, 21$ (1352Hz) $\simeq Trefoli7$

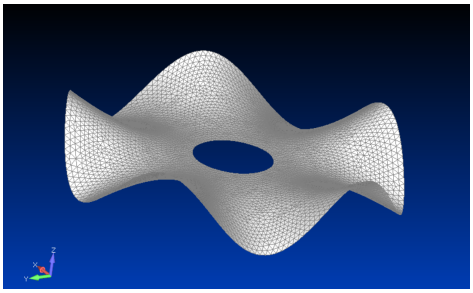

(h) $Modes\ 13, 15$ (845Hz) $\simeq Pentafoil9$

Figure 2.9: Zernike vs Structural Modes

Another setting available in the code is the incremental or "static" sequence of commands. Actually the step amplitude at a certain instant can be summed to the previous one or just taken as absolute value with respect to the reference null position. This choice offers the possibility to keep the commands bounded around the rest position. This latter condition is a realistic situation, since optical aberrations are absolute values and do not sum up. An incremental sequence of commands could exceed actuators saturation limits, which must be always checked.

Finally, also the step amplitude can be tuned to investigate its effects on the control effectiveness.

2.3 Command shaping filter

As discussed in the previous section, the output of the mirror shape generator is a series of step commands. Considering the low damping level of the mirror and the goal of this control system of limiting the structural oscillations, it would be surely detrimental using sharp and fast commands with a rich frequency content. As a matter of fact, a smoothing procedure of the input would help not exciting the reflective surface high frequency modes. A filter, used also in previous projects [2, 8], has thus been implemented to gently blend two consecutive steps. The transition occurs within the first half of the command timespan, whereas the remaining part of the interval is left to reach a steady state. This filter is realized with the following 5^{th} order polynomial, continuous up to the second derivative:

$$f_{sh}(t) = 6f^5t^5 - 15f^4t^4 + 10f^3t^3 \tag{2.29}$$

where f is twice the command frequency f_{cmd} to limit the climb to half the step length. The amplitude difference between two consecutive commands just multiply the shaping function, modulating its profile.

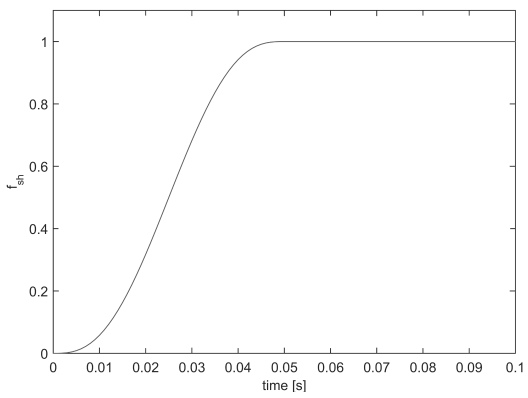

(a) Shaping filter, 10Hz unity signal

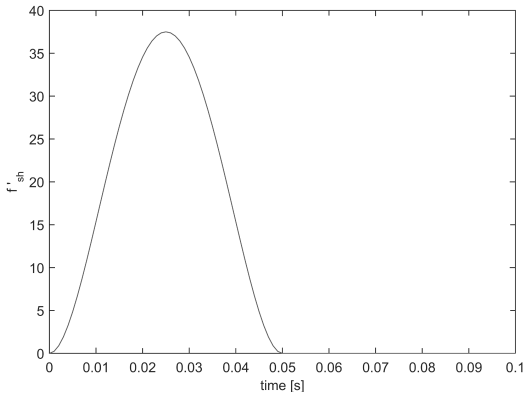

(b) Shaping filter first derivative

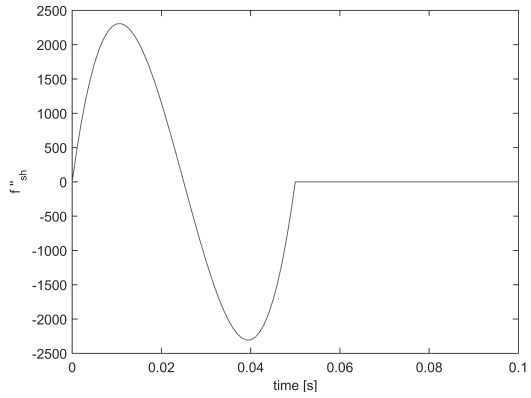

(c) Shaping filter second derivative

Figure 2.10: Shaping filter

Chapter 3

Oxymoronic Feedforward Control

Feedforward architectures have been widely used in control schemes to support feedback actions by improving the closed loop system promptness and producing dynamics compensation. Indeed, in pure feedback control laws, the error has to grow before the controller generates a considerable reaction, whereas, in a feedforward control solution, the reference amplitude influences directly the control intensity, avoiding the introduction of a time delay.

From an implementation point of view, the absence of measurements, along with the related wiring, leads to centralized control architectures which could have a practical realization even if a large number of actuators are used. Furthermore, as previously mentioned, the structure of a feedforward control scheme could also include some terms that, resembling the process dynamics, try to compensate its inertial and dissipation response and improve the tracking of static commanded positions.

However, in high precision control problems, the strong dependence of feedforward response accuracy on the accurate knowledge of the process dynamics, brought this schemes to be generally adopted as a complementary action to classical feedback approaches. This combined feedback-feedforward architecture has been applied to many engineering fields, ranging from robotics to Adaptive Optics applications, yielding satisfactory results.

In this chapter, along with the standard form, an advanced feedforward control law is presented. The strategy [15, 16, 17, 18] is an evolution of a classic feedforward control scheme with dynamics compensation. The result is a hybrid control scheme, that apparently has the aspect of a feedforward controller, but actually implicitly contains a feedback integral term. Indeed, measures are taken and integrated to statically correct and tune the direct action.

The preliminary use of a feedforward controller only (i.e., not combined with a complementary feedback action) allows to isolate and test the benefi-

cial damping effect of voltage-driven voice-coils, to the point that the design specs can be nearly satisfied without any feedback. This is shown and discussed in this chapter. The roadmap of this thesis is first to apply only this hybrid control system to drive the mirror and then to refine the performance by adding a true feedback control law. Actually, the electric dynamics should guarantee the required structural stability, while the feedback term hidden in the present feedforward scheme should at least limit the steady state positioning error on the final part of command steps.

3.1 Control scheme

In this section, two feedforward control schemes are presented. First, a classical feedforward controller is designed and implemented with the aim of being a reference solution to evaluate the suitability and effectiveness of a second approach based on a more advanced control scheme as mentioned above.

3.1.1 Classical feedforward controller

According to a classical feedforward scheme, the control force is assumed to be proportional to the reference position as follows

$$\mathbf{f}_{c_{ff}} = \mathbf{K}^* \, \mathbf{u}^r \tag{3.1}$$

where the matrix $\mathbf{K}^*$ is an estimate of the mirror stiffness matrix. The previous relation represents the force required to statically deform the shell to a desired shape. Since the system is voltage-driven, a similar relation holds for voltage and reference position as follows

$$\mathbf{V}_{c_{ff}} = \mathbf{K}_v^* \, \mathbf{u}^r \tag{3.2}$$

As already outlined in section 2.3, the command sequence is passed through a shaping filter that limits the dynamics excitation of the mirror. It is thus possible to write the reference position command at step $k+1$ as

$$\mathbf{u}^r(t) = \mathbf{u}_k^r + (\mathbf{u}_{k+1}^r - \mathbf{u}_k^r) f_{sh}(t) \qquad for \quad t \in [t_{k+1}, t_k] \tag{3.3}$$

where k is the command step index. Inserting this expression in Eq. (3.2) yields

$$\mathbf{V}_{c_{ff}}(t) = \mathbf{V}_{c_{ff},k} + \mathbf{K}_v^* \, (\mathbf{u}_{k+1}^r - \mathbf{u}_k^r) \, f_{sh}(t) \tag{3.4}$$

that is a recursive form of a classic feedforward control scheme, adapted to the problem at hand. It should be noted that the matrix $\mathbf{K}_v^*$ has to be identified on the field to have a good estimate. This would bypass all modelisation uncertainties and include also manufacturing, assembly or integration errors that could affect the correct static positioning of the surface.

3.1.2 Dynamic compensation

Even if the presence of a command shaping filter smooths the input, the incoming signal still represents a great source of dynamics excitation. A further improvement to the static expression of the feedforward control law described above is the addition of dynamic terms, proportional to mass-like and damping-like matrices $\mathbf{M}^*$ and $\mathbf{C}^*$. This somewhat standard refinement has been recovered and suggested for contactless, voice-coil actuated adaptive optics control systems in [8] and eventually applied to VLT (Very Large Telescope). The classical feedforward controller thus evolves into the following more advanced control scheme

$$\mathbf{f}_{c_{ff}} = \mathbf{K}^* \, \mathbf{u}^r + \mathbf{C}^* \, \dot{\mathbf{u}}^r + \mathbf{M}^* \, \ddot{\mathbf{u}}^r \tag{3.5}$$

The additional terms become more and more effective as long as $\mathbf{M}^*$ and $\mathbf{C}^*$ better resemble the real mass and damping matrices, respectively. Thus, like $\mathbf{K}^*$, they could be identified by properly testing the system on the field.

An alternative approach relies on finding good approximations as described below, that would avoid time and computer resources for the identification of the mass and damping matrices. The experimental determination is thus left only to the stiffness part, since it presents the most stringent precision requirements, as the correct positioning is very sensitive to errors in the $\mathbf{K}^*$ matrix elements.

The mass term could be simply expressed as a diagonal matrix as follows

$$\mathbf{M}^* = m^* \, \mathbf{I}$$

where m^* is nothing more than the total mass of the mirror divided by the number of the actuators and augmented by the mass of the single magnet

$$m^* = \frac{M_{mir}}{n_{act}} + m_{mgn}$$

The physical justification of this rough approximation can be found in a nearly uniform distribution of control points, that translates into a nearly equal inertial loading of each actuator. The mathematical validity check of the above assumption can be obtained by looking whether the product $\mathbf{X}^T\mathbf{X}$ is nearly diagonal.

The damping matrix is somewhat more complex, as its structure is indefinitely full. There exist some effective methods to reconstruct the structural $\mathbf{C}$ matrix from truncated modal shapes, natural frequencies and damping factors [29]. However, it should be highlighted that, for the problem at hand, the dominant damping effect is related to the eddy current term. Looking

at Eq. (2.16), it is clear that this dominant term is diagonal. Therefore, a diagonal approximation could be taken also in the case as follows

$$\mathbf{C}^* = c^* \, \mathbf{I}$$

where the coefficient c^* can be set equal to the square of the voice-coil efficiency η^2.

Finally, as with the stiffness matrix, also these terms have to be adapted to voltage control. Assuming the electric part considerably faster than the structural dynamics, the static approximation, already presented in section 2.1.2, can be exploited to properly scale the terms. Thus, knowing that $\mathbf{f} = K_t \, \mathbf{i}$ and neglecting the back emf term yields

$$\mathbf{V}_{c_{ff}} = \frac{R}{K_T} \, \mathbf{f}_{c_{ff}} \tag{3.6}$$

The dynamic part of the feedforward controller becomes

$$\mathbf{V}^{d}_{c_{ff}} = \mathbf{C}^*_v \, \dot{\mathbf{u}}^r + \mathbf{M}^*_v \, \ddot{\mathbf{u}}^r \tag{3.7}$$

Using Eq. (3.3), the feedforward command voltage along step $k+1$ becomes

$$\mathbf{V}_{c_{ff}}(t) = \mathbf{V}_{c_{ff},k} + [\, \mathbf{K}^*_v \, f_{sh}(t) + \mathbf{C}^*_v \, \dot{f}_{sh}(t) + \mathbf{M}^*_v \, \ddot{f}_{sh}(t) \,] \, (\mathbf{u}^r_{k+1} - \mathbf{u}^r_k) \tag{3.8}$$

where $\mathbf{V}_{c_{ff},k}$ is the static part of the command voltage applied at the end of the previous step. The incremental form of the control is explicit and the benefit of an up to second order continuous shaping function, in terms of signal smoothness, becomes clear looking at its derivatives presence.

3.1.3 Hybrid feedforward controller

The basic structure of the hybrid feedforward is still made up of a static and a dynamic term

$$\mathbf{V}_{c_{ff}} = \mathbf{V}^{s}_{c_{ff}} + \mathbf{V}^{d}_{c_{ff}} \tag{3.9}$$

The latter term proposes again a dynamic compensation in the form shown in Eq. (3.8)

$$\mathbf{V}^{d}_{c_{ff}}(t) = [\, \mathbf{C}^*_v \, \dot{f}_{sh}(t) + \mathbf{M}^*_v \, \ddot{f}_{sh}(t) \,] \, (\mathbf{u}^r_{k+1} - \mathbf{u}^r_k) \tag{3.10}$$

The main difference with respect to previous schemes lies instead in the static term, that modifies Eq. (3.4) as follows

$$\mathbf{V}^{s}_{c_{ff}}(t) = \overline{\mathbf{V}}_{c,k} + \mathbf{K}^*_v \, (\mathbf{u}^r_{k+1} - \overline{\mathbf{y}}^r_{u,k}) \, f_{sh}(t) \tag{3.11}$$

Here, $\overline{\mathbf{V}}_{c,k}$ and $\overline{\mathbf{y}}^r_{u,k}$ indicate, respectively, the time averages of the control voltage and the measured position, computed over the final half part of step k. The underlying assumption is that the response is essentially steady and that every actuator has achieved a stable average position $\overline{u}$, by applying an average control voltage $\overline{V}_c$. This leads to an "oxymoronic"[1] control, providing feedback through a feedforward design [8]. The hidden action is a sort of integral term. Actually, neglecting for a while the shaping function, after expanding the recursive term, it could be written

$$\mathbf{V}^s_{c\,ff}(t) = \mathbf{K}^*_v \sum_{i=1}^{k} (\mathbf{u}^r_{i+1} - \overline{\mathbf{y}}^r_{u,i}) \tag{3.12}$$

It should be also noted that the average position can be expressed as the summation of the reference position and an averaged error of the measured position as follows

$$\overline{\mathbf{y}}^r_{u,i} = \mathbf{u}^r_i + \overline{e}_i \tag{3.13}$$

Combining Eqs. (3.12) and (3.13) yields

$$\mathbf{V}^s_{c\,ff}(t) = \mathbf{K}^*_v \sum_{i=1}^{k} (\mathbf{u}^r_{i+1} - \mathbf{u}^r_i - \overline{e}_i) = \mathbf{K}^*_v\, \mathbf{u}^r_{k+1} - \mathbf{K}^*_v \sum_{i=1}^{k} (\overline{e}_i) \tag{3.14}$$

The first term is the classic static feedforward contribution, whereas the second one is a sort of feedback integral action, applied at the slow optical loop frequency, with a centralized gain structure represented by the matrix $\mathbf{K}^*_v$. The possibility of computing meaningful values for the two averaged quantities relies on a quiet and stable steady state condition for the final part of each command step [8]. In a feedforward scheme, this is guaranteed only by a proper level of damping. It thus becomes evident that the use of a feedback term would not only add a corrective action, but would also improve the feedforward precision by increasing the quality of the averaged quantities. Another advantage of this hybrid approach is that the integral recovers also the static errors arising from discrepancies between estimated and true stiffness matrix. Demonstration of this can be found in related papers [8]. As a result, it is possible to relax the precision requirements on the matrix identification, even if a good estimation would for sure guarantee immediate accurate positioning.

Oxymoronic control stabilization

Like every feedback integral action, the oxymoronic feedforward control previously described can produce instabilities. Since the actual gain of the

[1] since, basically, a feedforward term is used, unchanged, as feedback

integral is somehow embedded in the stiffness matrix, a method has been devised to limit the application of the destabilizing term without touching $\mathbf{K}_v^*$. A mixed form, containing both the classic feedforward term and its oxymoronic evolution, is implemented by weighting the two variants in the same expression. Calling α the stabilizing relative weight, the following modified version of Eq. (3.11) is introduced

$$\begin{aligned}\mathbf{V}_{c_{ff}}^{s} = [\urcorner\alpha\llcorner]\overline{\mathbf{V}}_{c,k} + (\mathbf{I} - [\urcorner\alpha\llcorner])\mathbf{V}_{c_{ff},k} + \\ + \mathbf{K}_v^* \{ \mathbf{u}_{k+1}^r - ([\urcorner\alpha\llcorner] \overline{\mathbf{y}}_{u,k} + (\mathbf{I} - [\urcorner\alpha\llcorner]) \mathbf{u}_k^r) \} f_{sh}(t)\end{aligned} \tag{3.15}$$

The limit values of α are 0 and 1, corresponding respectively to the pure classical feedforward and to the pure oxymoronic form. It is possible to vary this weight in the range [0,1] making the control pending towards one of the two formulations. The main idea is to decrease the value of α as long as instabilities appears. It is clear that a lower value would reduce the integral effect, requiring more time to fully eliminate static errors.

Jump-free implementation

The insertion of temporal averages alters the continuity properties of the control recursive formulation. Thus, small arrangements have been taken to adapt the shaping effect to the actual static voltage jump, without substantially varying the control properties. A jump-free formulation is thus reformulated as follows

$$\begin{aligned}\mathbf{V}_{c_{ff}}^{s} = \mathbf{V}_{c_{ff},k} + \{ [\urcorner\alpha\llcorner]\overline{\mathbf{V}}_{c,k} + (\mathbf{I} - [\urcorner\alpha\llcorner])\mathbf{V}_{c_{ff},k} - \mathbf{V}_{c_{ff},k} + \\ + \mathbf{K}_v^* \, \mathbf{u}_{k+1}^r - ([\urcorner\alpha\llcorner] \, \overline{\mathbf{y}}_{u,k} + (\mathbf{I} - [\urcorner\alpha\llcorner]) \, \mathbf{u}_k^r) \} \, f_{sh}(t)\end{aligned} \tag{3.16}$$

It is a slight modification of Eq. (3.15), where the shaping function modulation starts at the end voltage value of the previous command step.

3.1.4 Estimation of the stiffness matrix

The correct positioning of the mirror is for sure helped by the integral action introduced above, but it still strongly relies on the correctness of the estimation of the stiffness matrix. As previously mentioned, an identification procedure of this matrix is carried out on the field. The FE model could be sufficient for providing $\mathbf{K}^*$, but would suffer from poor knowledge of some system parameters and from manufacturing and integration errors.

The identification procedure is a pre-operational phase during which a series of known commands are sent to the mirror and its response is measured. Before measuring the position, the system is allowed to stabilize. After this

stabilization, the measures are taken for a sufficiently long time. In such a way, a considerable number of samples are taken and the averages quality increases, according to the square root of the number of measures [8].

The steady state response of the mirror can be described with the equation

$$\mathbf{K}\,\mathbf{u} = \mathbf{f}_c + \mathbf{f}_d \tag{3.17}$$

Voltage scaling yields

$$\mathbf{K}_v\,\mathbf{u} = \mathbf{V}_c + \frac{R}{K_t}\mathbf{f}_d \tag{3.18}$$

It is thus possible to write

$$\overline{\mathbf{V}}_c^T = \overline{\mathbf{y}}_u^T\,\mathbf{K}_v^{*T} - \frac{R}{K_t}\bar{\mathbf{f}}_d^{*T} = \begin{bmatrix}\overline{\mathbf{y}}_u^T & -\frac{R}{K_t}\end{bmatrix}\begin{bmatrix}\mathbf{K}_v^{*T} \\ \bar{\mathbf{f}}_d^{*T}\end{bmatrix} \tag{3.19}$$

Here, we have two unknowns: the stiffness matrix and the average disturbance force. The identification also of any possible static disturbance it is thus accounted for. Unfortunately, this equation is not sufficient to find $\mathbf{K}_v^*$, since the system is undetermined. To solve the problem at least $n_a + 1$ equations are necessary. Furthermore, it is advisable to write an overdetermined system to limit the noise effect. This procedure takes less time as the operational frequency increases. Generally speaking, even with thousands of samples and hundreds of tests, the time required by the identification would be in the order of minutes. Collecting all the equations of type 3.19, it is thus possible to write

$$\begin{bmatrix}\overline{\mathbf{y}}_{u,1}^T & -\frac{R}{K_t} \\ \overline{\mathbf{y}}_{u,2}^T & -\frac{R}{K_t} \\ \vdots \quad\quad \vdots & \\ \overline{\mathbf{y}}_{u,n}^T & -\frac{R}{K_t}\end{bmatrix}\begin{bmatrix}\mathbf{K}_v^{*T} \\ \bar{\mathbf{f}}_d^{*T}\end{bmatrix} = \begin{bmatrix}\overline{\mathbf{V}}_{c,1}^T \\ \overline{\mathbf{V}}_{c,2}^T \\ \vdots \\ \overline{\mathbf{V}}_{c,n}^T\end{bmatrix} \tag{3.20}$$

To solve this system various ideas have been proposed. It is possible for example to use an LDL factorization and to implement an iterative update of the matrix, which can be also kept active during the operations of the telescope [8].

Since the identification procedure is not a topic investigated in this thesis and the whole process simulation would be computationally onerous and time demanding, an equivalent representation of the process itself and its effect has been inserted in the code. At the beginning, a direct introduction of random errors into the exact stiffness matrix was considered. However, this solution leads to a loss of its positiveness, with resulting unrealistic errors.

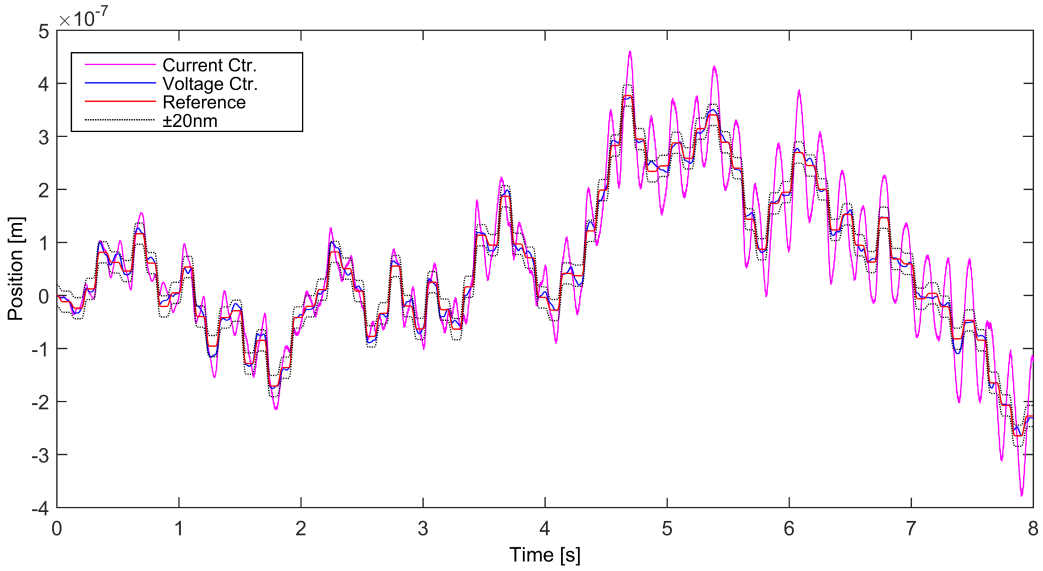

Figure 3.1: Voltage vs Current Drive - actuator response

Therefore, a simple reproduction of the identification procedure was taken from previous studies [8]. In particular, at each step, a random but known voltage is sent to the actuators and only the static response of the mirror is analytically computed by matrix product. Then, noise is artificially inserted into voltage and position vectors, before averaging operations

$$\overline{\mathbf{y}}_u^n = \frac{\sum_{j=1}^{n_{smp}} (\mathbf{y}_{u,j} + Gauss(\sigma_y))}{n_{smp}} \tag{3.21}$$

$$\overline{\mathbf{V}}_c^n = \frac{\sum_{j=1}^{n_{smp}} (\mathbf{V}_{c,j} + Gauss(\sigma_V))}{n_{smp}} \tag{3.22}$$

In such a way it is possible to simulate the errors in the process. Finally, the system in Eq. (3.20) is simply solved with the pseudoinverse computation. Since the number of equations are well in excess, the result is a least square estimation. The script offers the possibility of setting both the number of test steps and the samples taken at each step. Clearly, both parameters affect the quality of the results.

3.2 Voltage-driven versus current-driven actuation

As already mentioned in the introduction of this chapter, it is interesting to test the effective damping action introduced by voltage-driven voice-coils

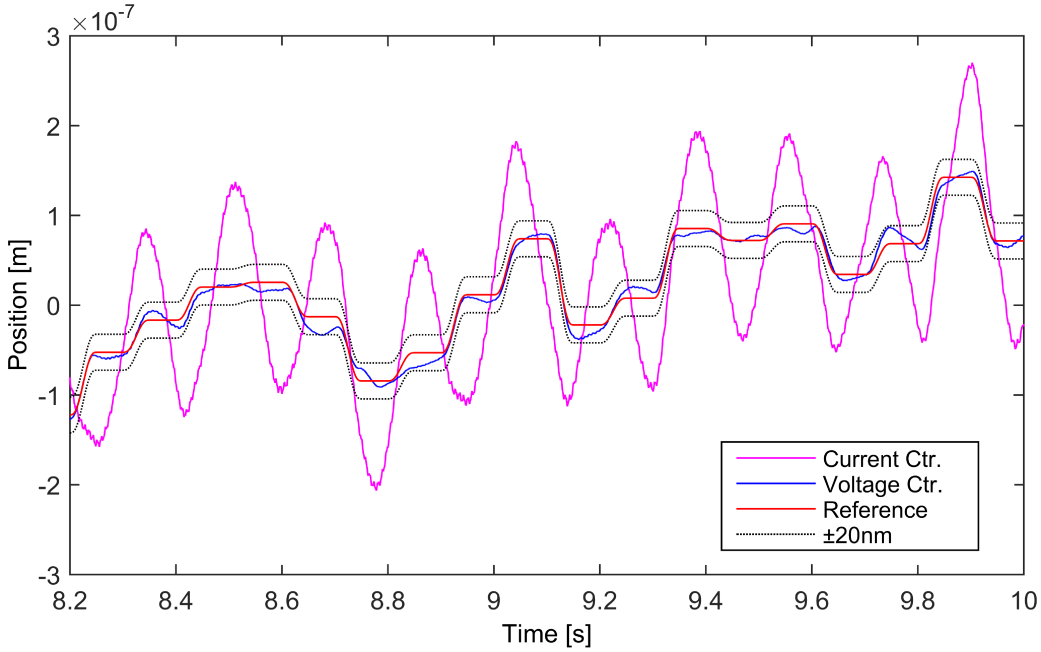

Figure 3.2: Voltage vs Current Drive - actuator response (zoom)

actuating the P45 mirror. To this end, a comparison model with current-driven actuators has been built. In this model, the electric part is omitted and a direct control on the current, and so on the force exerted, is assumed.

The analysis is carried out as follows. A series of random step positions at a frequency of 10Hz has been created using the mirror shape generator, and the system responses have been simulated and collected. During these tests, the exact stiffness matrix has been used in the control law, without any noise in the measurements and actuators. Accordingly, the only sources of dynamical excitation were the commands themselves.

Despite this fact, the result is a significant difference between the two configurations. As could be seen in figures 3.1 and 3.2, current-driven actuators exhibit highly oscillatory response. This comes to little surprise as the system can only rely on a practically nihil intrinsic structural damping (sec. 2.1.1) and on limiting the input frequency content with smooth signals. This is clearly the weak point of current-driven actuators in a space application, since the lack of damping results in strong limitations in enlarging the feedback control bandwidth and achieving high closed-loop performance. It should be highlighted that current-driven actuators are a better choice, but they require a suitable passive damping, i.e. the squeezed air film available on Earth. For example, an advanced design of the mirror central membrane could help in dissipating the vibrational energy accumulated by the shell.

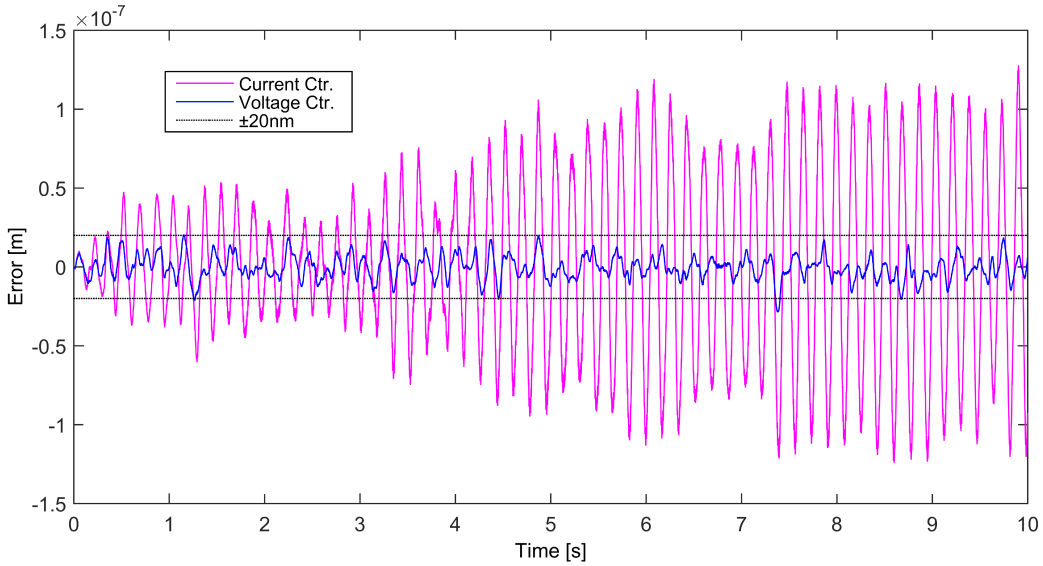

Figure 3.3: Voltage vs Current Drive - position error

There are also some viscoelastic materials that, applied as thin layers on the structure surface, could increase significantly the structural damping of the mirror. Yet, they result hardly applicable to a delicate and quality demanding optical surface.

On the contrary, the adoption of voltage-driven actuators offers a simpler solution to the lack of passive damping, by release of eddy currents. Looking at figures 3.1 and 3.2 again, it can be noticed how this second approach produces a more stable response. The absence of oscillations and sawtoothed response profiles, which instead are present in the current-driven case, demonstrates a significant increase in the damping level, both at low and high frequencies. The position error with respect to the reference appears to grow in time for current-driven actuators, whereas it remains bounded in the voltage-driven case. This clearly comes out in figure 3.3, where $\pm$20nm bounds are also highlighted. It is noted that this is not yet the desired performance level, but it can be already considered a rather satisfactory result, achieved just with a mere feedforward controller.

Another comparison between the two different voice-coil drives has been carried out by computing the minimum structural damping level which is required to obtain, in the current-driven case, the same performance as in the voltage-driven case. The rms error over the actuators points has been taken as comparison quantity. Simulations have been run at different ξ values. The results, reported in figure 3.4, show that, to obtain similar performances, the structure should present a damping level in the order of tenths. Even with

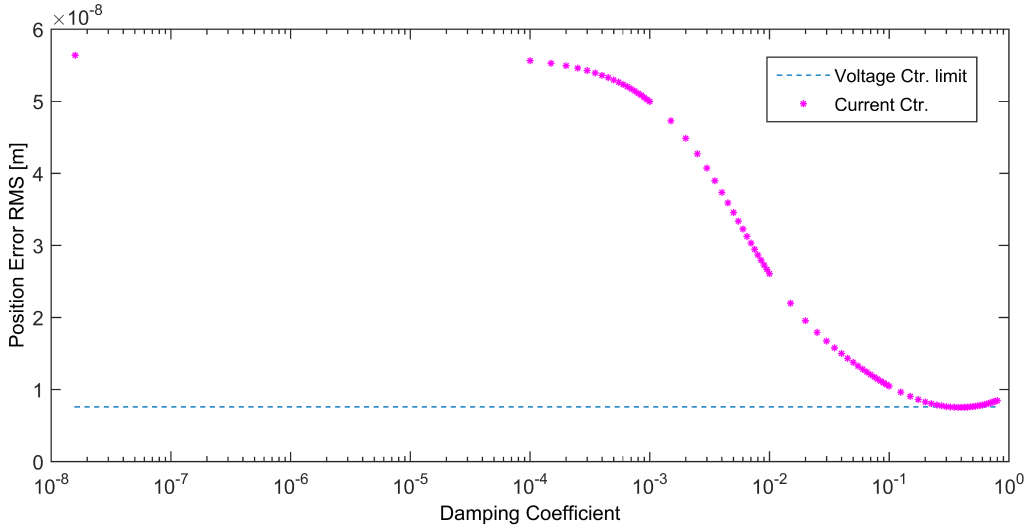

Figure 3.4: Voltage vs Current Drive - spatial error rms as function of damping

an advanced passive design, it seems unrealistic to achieve such conditions, though it is possible to obtain good results with passive elements supported by a feedback control. It is thus reasonable to give up the direct force control, moving to voltage driving the actuators circuits. Since the electrical dynamics is typically faster than the command rate, the presence of the electric filter constituted by the circuit should not be source of problems. It could produce troubles in digital implementation, where high control frequencies are presumably required. In this case, its effect would be to filter the commands, so degrading the performance.

In conclusion, the previous analysis has shown that voltage-driven voice-coils turn out to be a robust, attractive and promising approach for an active control of a secondary mirror shape controller, based on a contactless technology already successful on Earth.

3.3 Validation of the feedforward controller

In this final section, the hybrid feedforward control scheme presented before is tested under critical conditions to verify its actual capabilities and to remove any doubt, related to fortuitous operational conditions, on the voltage control effectiveness. System parameters has been varied and brought to their operational critical values, looking for possible weak points in the proposed architecture and providing a first overview of the system sensitivity

to modeling uncertainties.

The first simulation has been run to evidence the oxymoronic capability to limit steady state errors. A relatively well identified $\mathbf{K}^*$ matrix has been generated, assuming the exploitation of about 4500 command steps of 10000 samples each. Nominal motor efficiency $\eta = 0.4\ \mathrm{N}/\sqrt{\mathrm{W}}$ has been assumed for the actuators. Small random errors has been added to the nominal damping and mass matrices in order to simulate a model with uncertainties. Finally, both measurements and actuation noise has been introduced to simulate operative conditions. As could be seen in figures 3.5 and 3.6, the classical feedforward scheme presents a response which is gradually drifting from the reference. This is mainly due to imprecision in the estimated stiffness matrix, that, combined with commanded positions of increasing amplitude, brings the system to accumulate static discrepancies. On the contrary, under the same conditions, the oxymoronic control scheme limits this drifting effect as shown in figure 3.7 and 3.8.

A second analysis was carried out by reducing the actuators' efficiency. Indeed, it is known that its value varies with the amplitude of the gap between the mirror and the reference plate, and so with the commanded position. Since the level of the electrically induced damping is directly linked to η, it is worth checking the system stability at its lower value. According to the actuators characteristics, it could be stated that a conservative lower bound for η is $0.3\,\mathrm{N}/\sqrt{\mathrm{W}}$. As the damping decreases, the feedback integral term approaches the limit of instability. As already mentioned in section 3.1.3, in such cases it is required to reduce the value of α in order to have a partial oxymoronic action. In the selected conditions, α should be reduced down to 0.6 to guarantee that the responses could be univocally considered stable. This value corresponds to a very low oxymoronic contribution, since the control action is almost half determined by the classical feedforward scheme. However, it is expected that α could be increased, once a feedback controller would flank the feedforward control. The stiffness matrix has been considered to be nicely estimated, but contains suitable estimation errors, while $\mathbf{M}^*$ and $\mathbf{C}^*$ matrices have been spoiled with up to 10% errors. The system response is reported in figures 3.9 and 3.10. It exhibits an evident worsening of the average error level, that is more ore less 1.5 times the nominal case, but a stable behavior is preserved. The oxymoronic term still shows its beneficial effect, despite it requires more steps to fully compensate the greatest steady state errors due to its limited contribution. Actually, with respect to figure 3.8, the error trends in figure 3.10 present bumps, that are slowly eroded by the integral action.

The final test related to the feedforward control action was a series of step responses at a frequency of 20 Hz. A higher command frequency would indeed

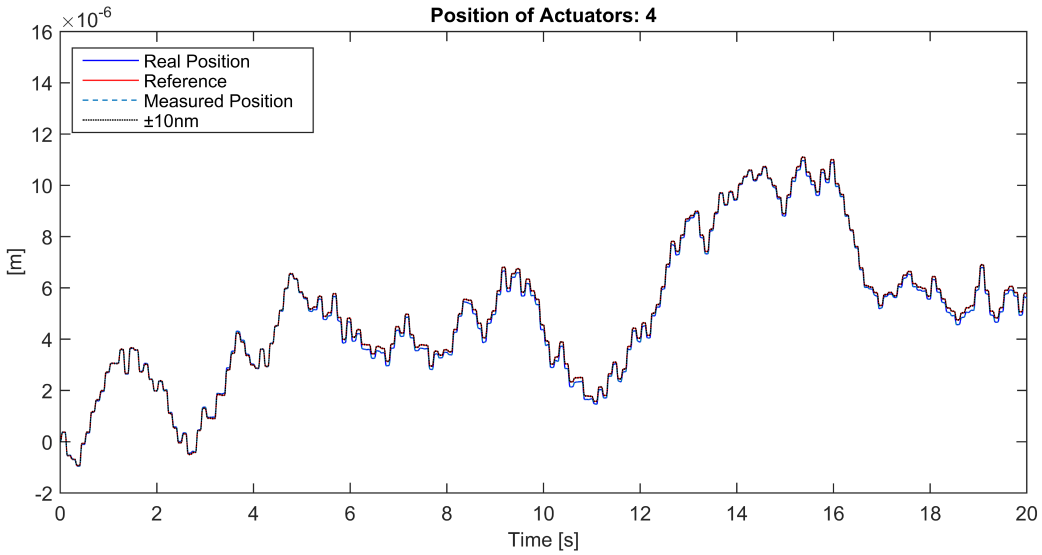

(a)

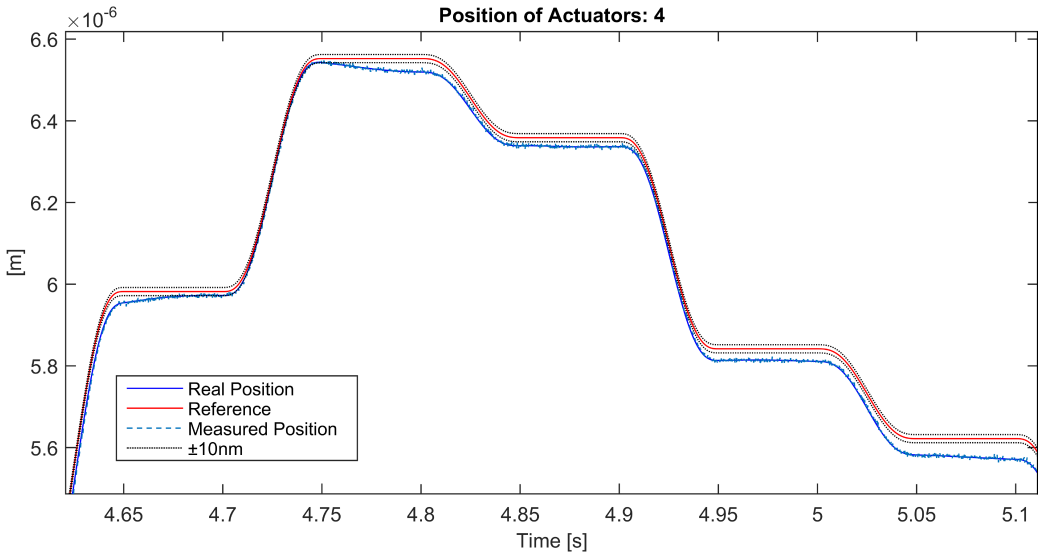

(b)

Figure 3.5: Classic Feedforward - actuator response

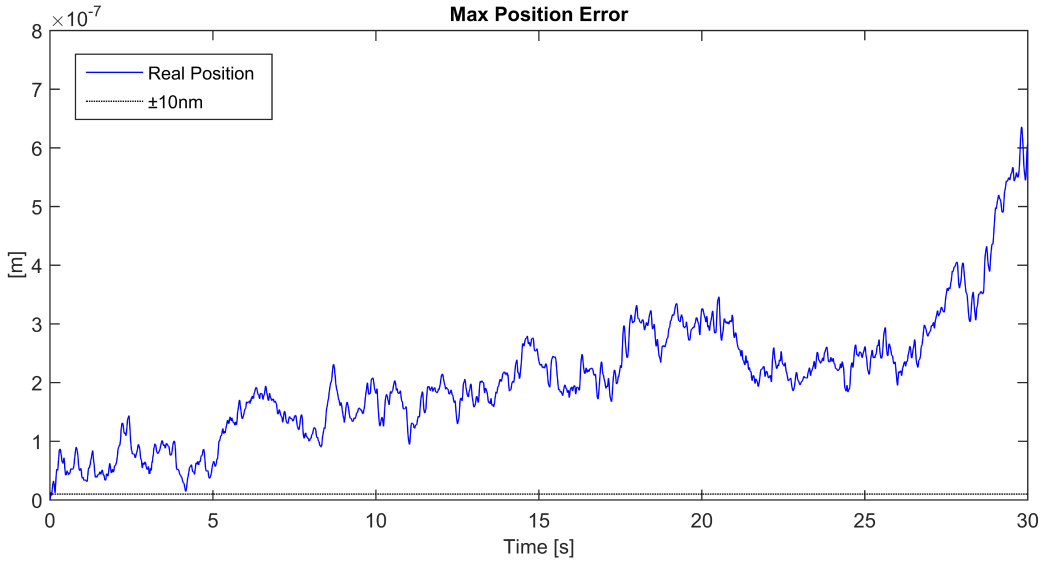

(a) maximum between actuators

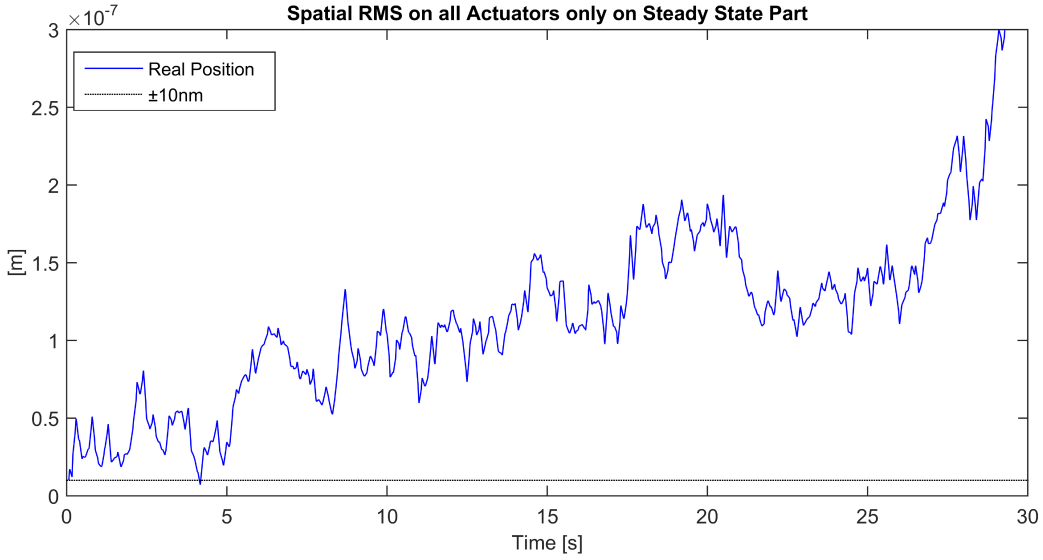

(b) spatial rms, only steady state part

Figure 3.6: Classic Feedforward - error

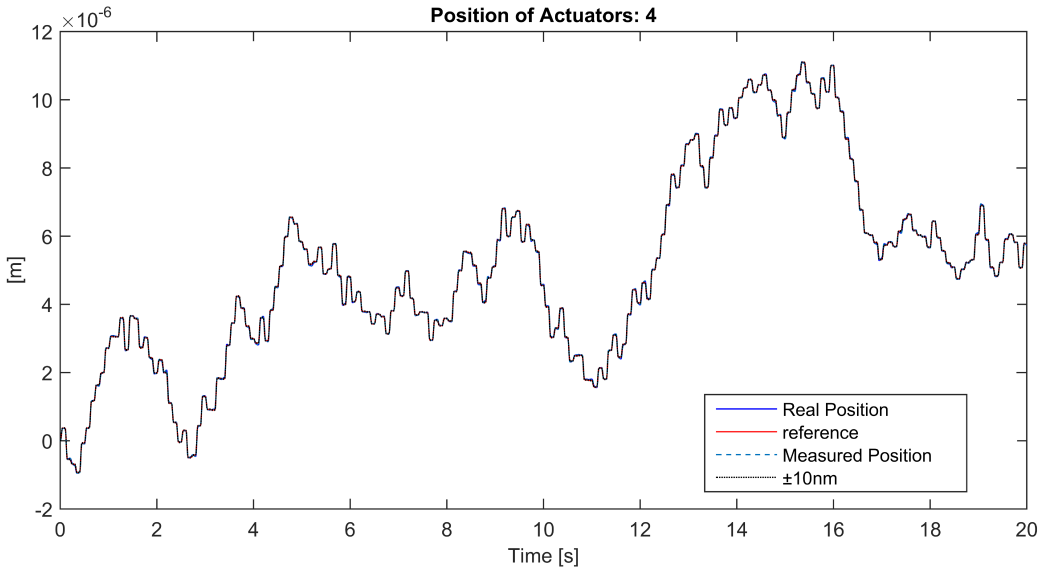

(a)

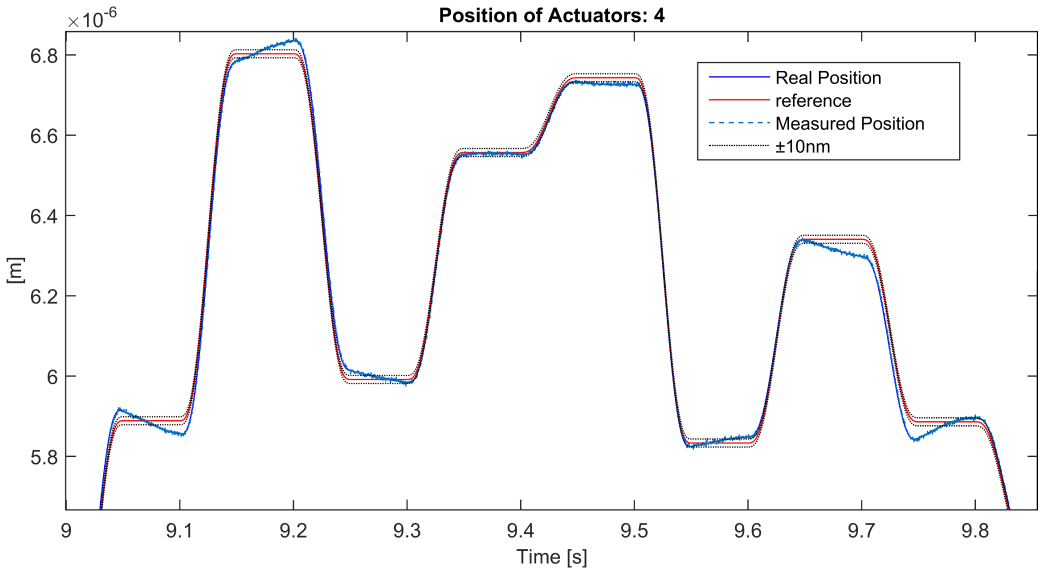

(b)

Figure 3.7: Oxymoronic Feedforward - actuator response

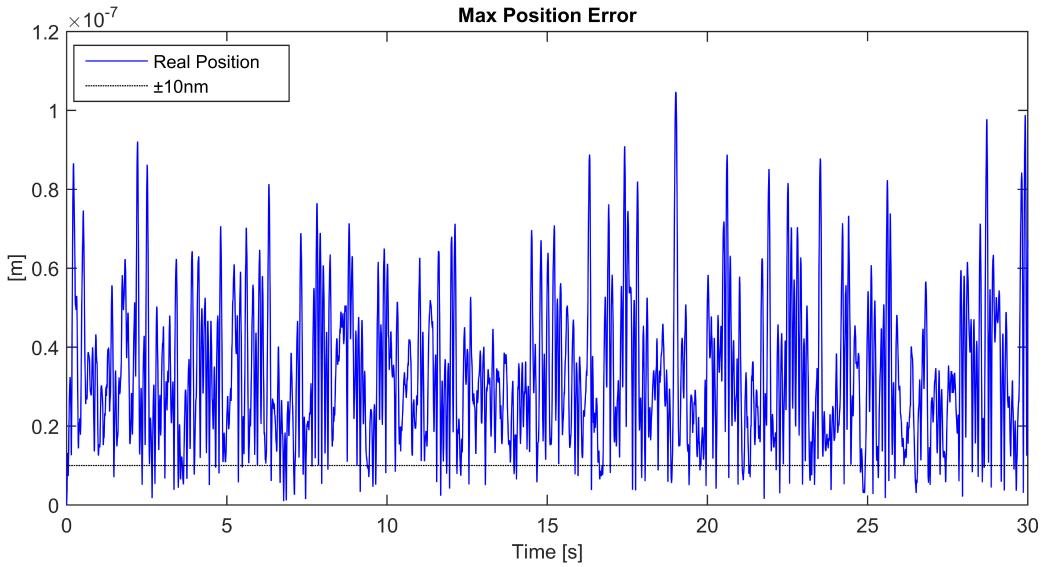

(a) maximum between actuators

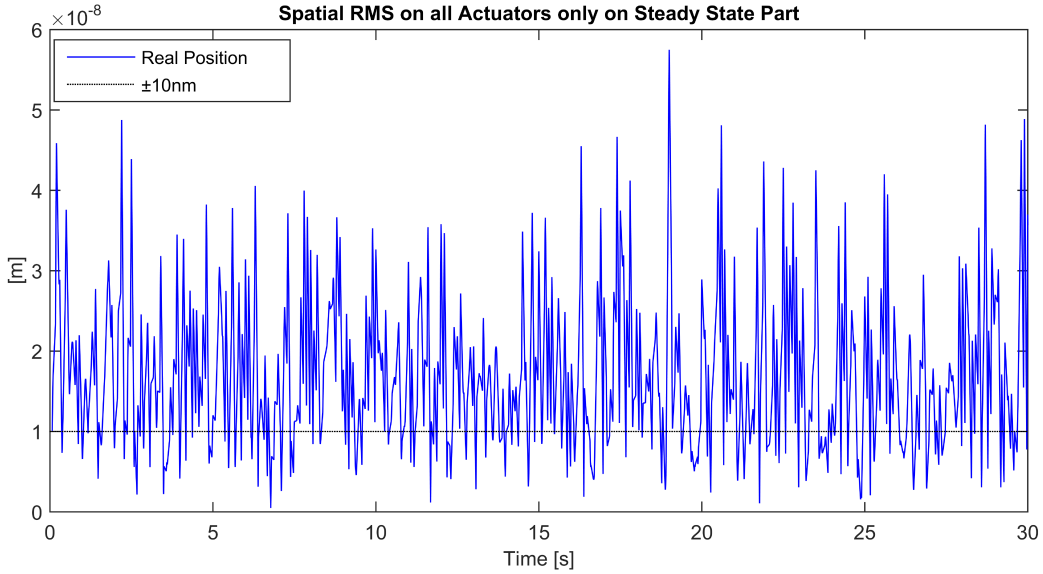

(b) spatial rms, only steady state part

Figure 3.8: Oxymoronic Feedforward - error

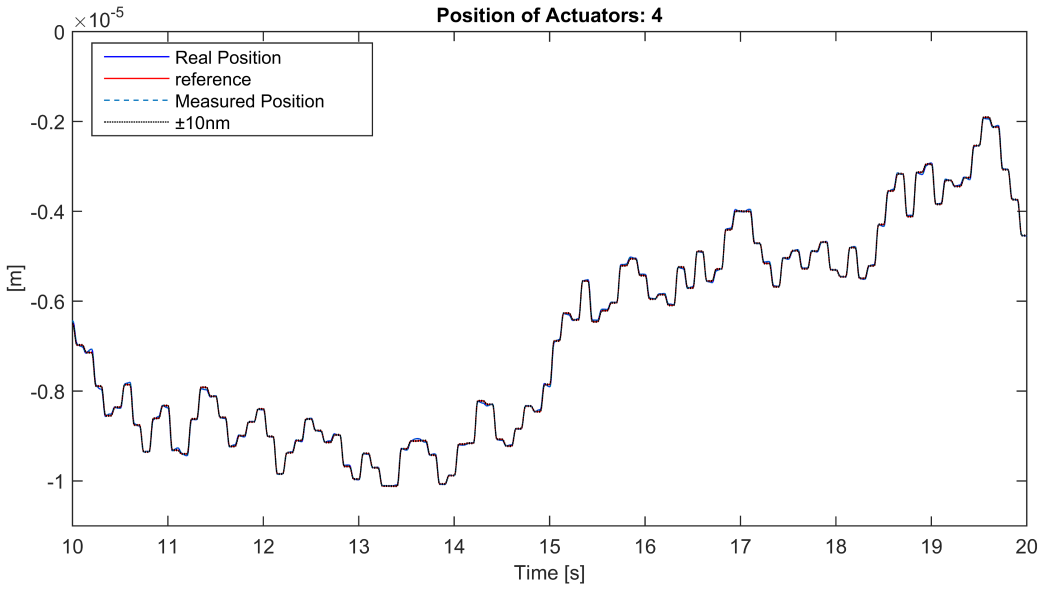

(a)

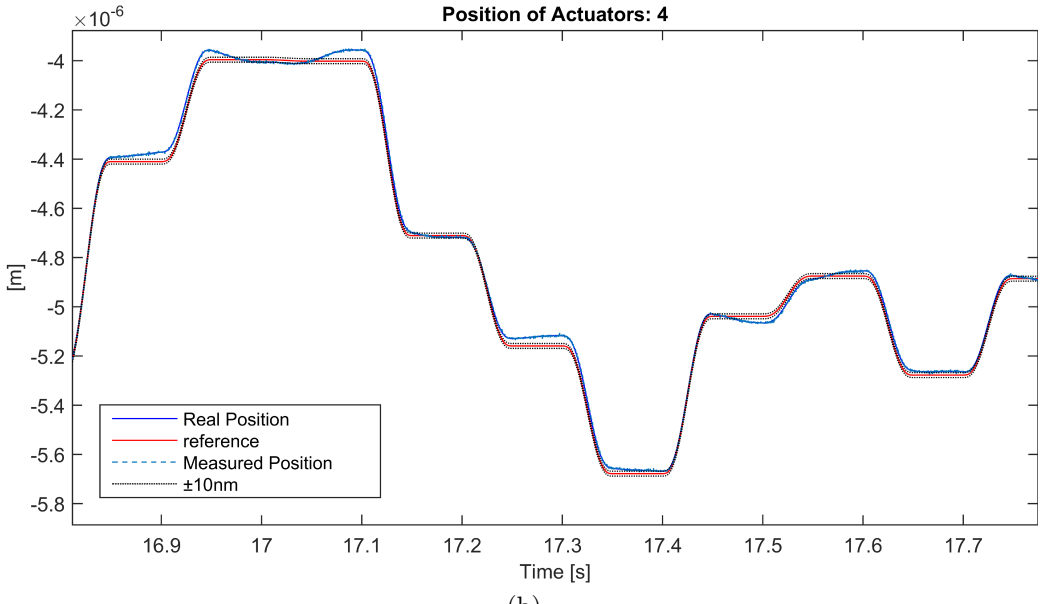

(b)

Figure 3.9: Test for $\eta = 0.3\,\mathrm{N}/\sqrt{\mathrm{W}}$ - actuator response

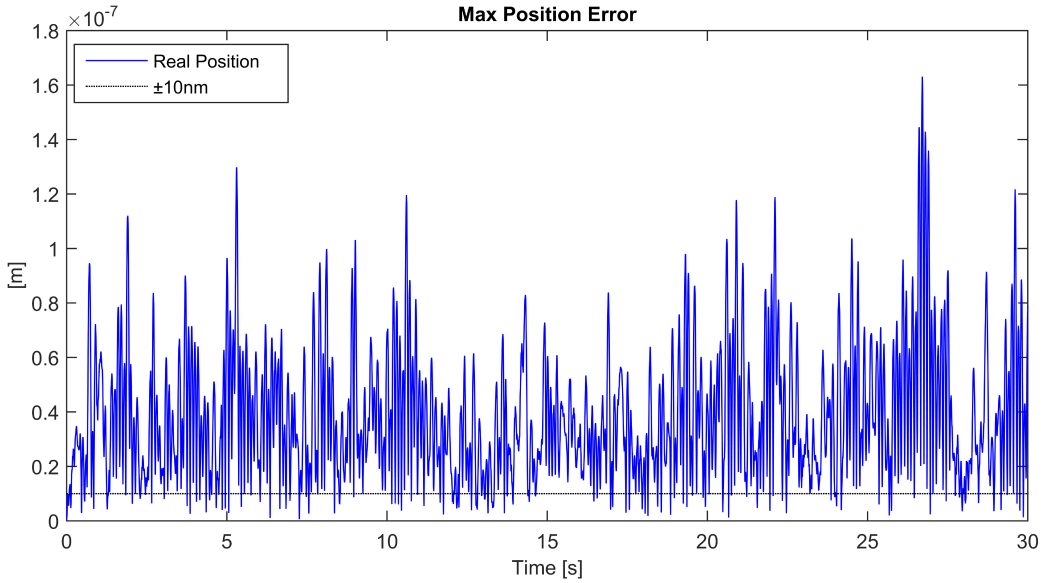

(a) maximum between actuators

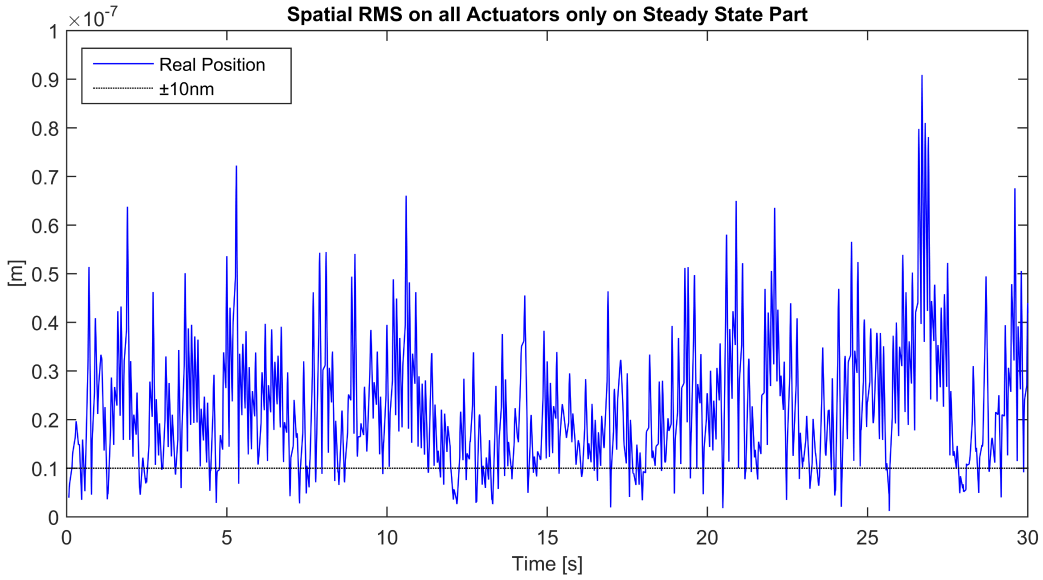

(b) spatial rms, only steady state part

Figure 3.10: Test for $\eta = 0.3\mathrm{N}/\sqrt{\mathrm{W}}$ - error

increase the structural excitation level. The system parameters have been kept equal to the previous test. The only difference has been the amplitude of the steps. Indeed, a certain command could be split into two substeps of half the amplitude, executed at twice the frequency. This simulation test can be considered not only a conjecture on limit performances of the mirror, but also a feasible alternative to perform the same tasks. The weak point of this approach is that, despite a lower amplitude that could induce reduced error, the computational resources needed to calculate the low frequency control law would be doubled. Looking at figures 3.11 and 3.12, the response shows no major differences with respect to $\eta = 0.3\,\mathrm{N}/\sqrt{\mathrm{W}}$ simulation. The average error is lower thanks to the reduced amplitude of the commands and, dynamically, the system appears to behave well also at 20 Hz frequency.

All simulations and results proposed in this section strengthen and support the conclusions that have been drawn at the end of section 3.2.

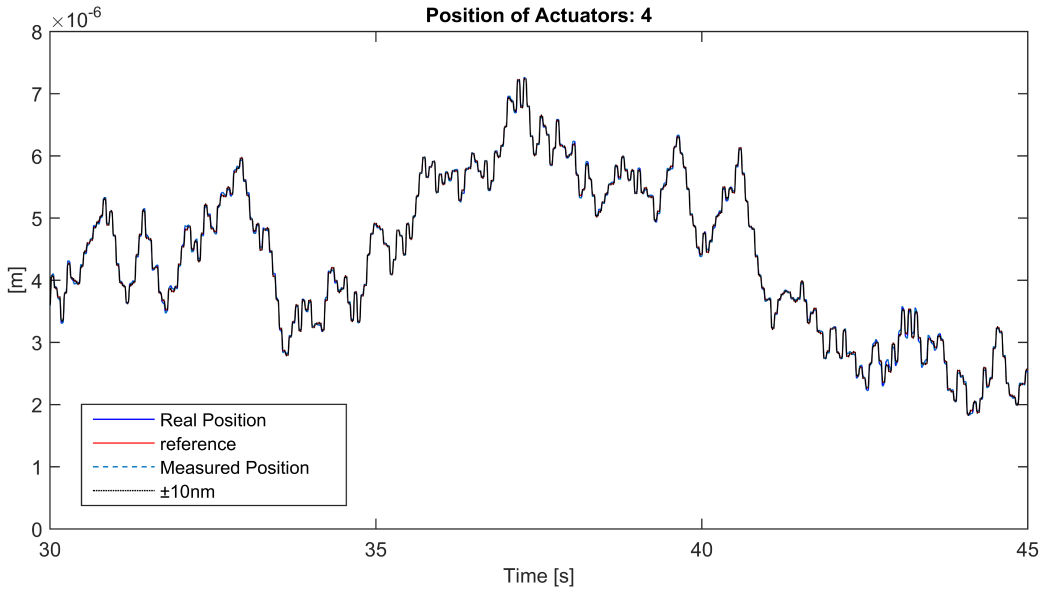

(a)

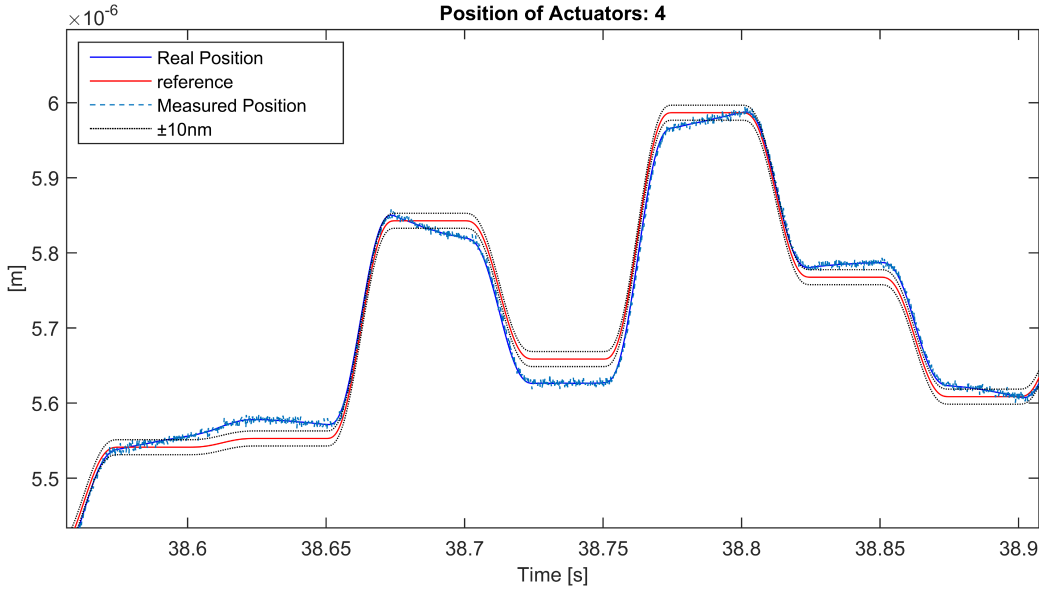

(b)

Figure 3.11: Test for 20 Hz commands - actuator response

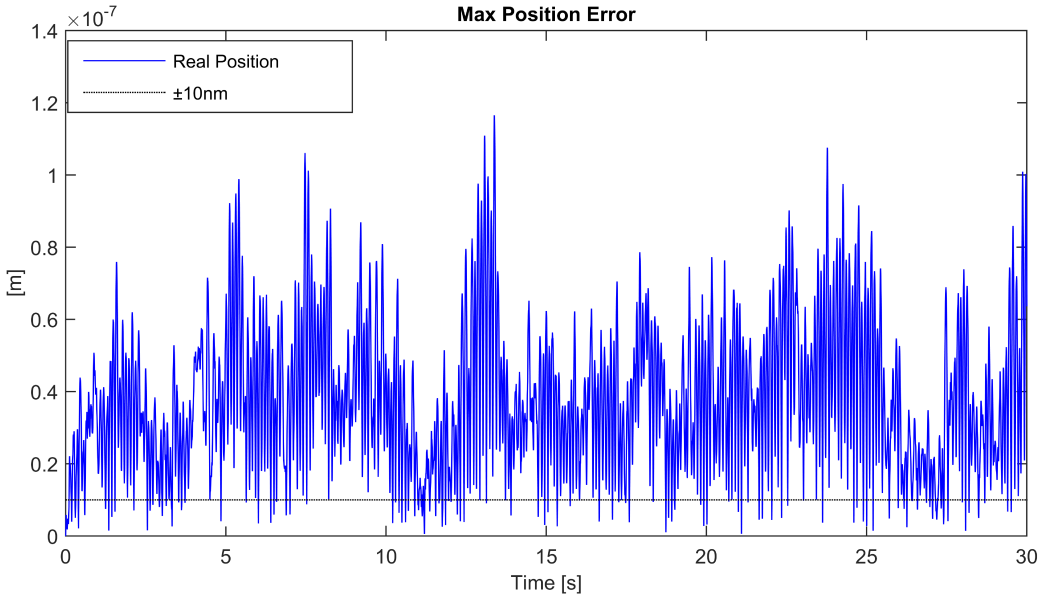

(a) maximum between actuators

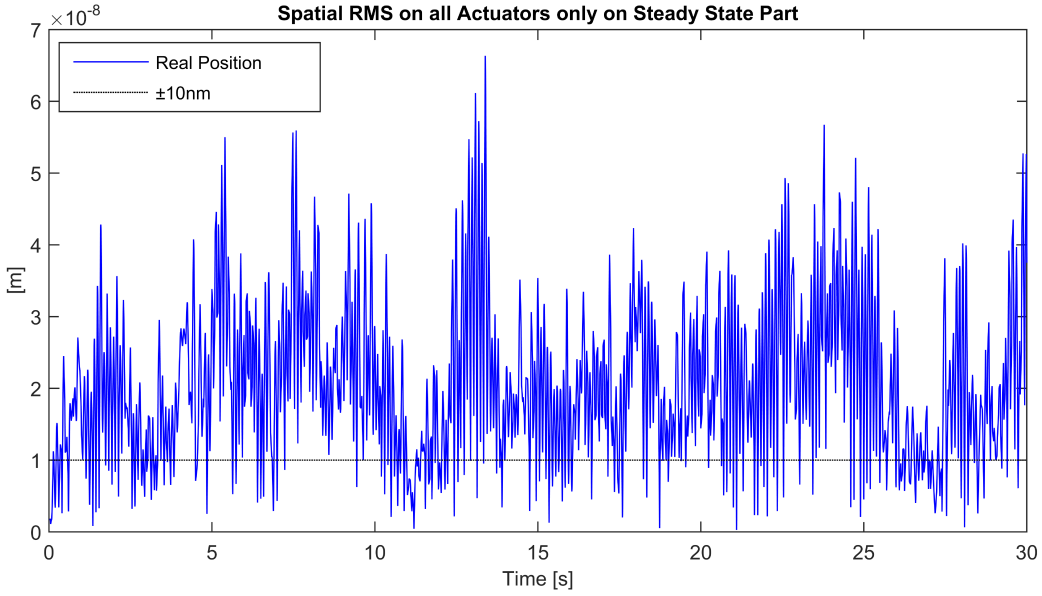

(b) spatial rms, only steady state part

Figure 3.12: Test for 20 Hz commands - error

Chapter 4

Static Output Optimal Feedback Control

As mentioned many times in the previous chapter, the final control scheme developed in this thesis involves a combined feedforward-feedback architecture. The feedforward part is represented by the oxymoronic scheme just presented. The closed loop controller is an optimized static output feedback, also known as suboptimal control. The reason is twofold. First, contrary to a full state optimal control, which requires the knowledge of the whole system state, the suboptimal scheme is based on feeding back an output quantity that can be easily measured with proper sensors. As such, no reconstruction of the state is required. Furthermore, the suboptimal controller offers a greater flexibility than the optimal solution since it allows to impose the controller structure, i.e., the control scheme can range from a fully decentralized controller with a diagonal gain matrix up to a fully centralized architecture where each control voltage is related to all elements of the measurement vector.

Broadly speaking, it could be stated that the static output optimal feedback control relies on a very simple scheme where the vector of control voltages is assumed to be proportional to the output vector through a control gain matrix $\mathbf{G}$. Therefore, the design of the feedback control law reduces to a procedure aimed at determining the matrix $\mathbf{G}$ such that some desired closed-loop performances are achieved. However, it is noted that the above representation is only a conceptual description of the feedback logic. The real implementation of the control system is more complicated and should be carefully considered in the design process.

The optimal static output feedback control is part of the so called Optimal Control Theory. This theory, based on the state space representation, deals with finding a control law which satisfies a prescribed optimality criterion.

Accordingly, the problem is formulated through a quadratic cost function, which is minimized in the presence of certain constraints.

A particular case of the optimal control problem is the so-called linear quadratic (LQ) optimal control problem, where the cost function takes the form of a quadratic expression of both state and control variables. It can be shown that the LQ optimal solution for linear time-invariant systems leads to the well-known feedback form $\mathbf{u}(t) = -\mathbf{G}(t)\mathbf{x}(t)$, where $\mathbf{u}$ and $\mathbf{x}$ are the control and state vector, respectively, and $\mathbf{G}$ is the gain matrix. In the infinite-horizon case, the $\mathbf{G}$ matrix is constant and can be expressed in terms of a matrix which is computed by solving an algebraic Riccati equation. Therefore, as already outlined, the LQ optimal control requires the knowledge of the state vector, which can be obtained through a, possibly optimal, observer. An observer is a dynamical system, resembling the actual physical system, whose aim is to give an accurate estimation of the full state vector. It involves a set of differential equations that should be integrated at each time step. In a digital implementation, the presence of an observer significantly increases the computational time and resources associated with the application of the control action. Furthermore, the observer must be carefully designed to be stable and to have desired dynamic properties in terms of bandwidth and noise rejection. The resulting design process may be not trivial. The adoption of a direct output feedback control of the form $\mathbf{u}(t) = -\mathbf{G}\mathbf{y}(t)$, where $\mathbf{y}$ is the output vector, completely eliminates the need of a state reconstruction system and so is exempt from the issues associated with it. However, since the output vector can be viewed as a subset of the full state vector, the corresponding feedback law yields a sub-optimal solution of the control problem, since the global LQ minimum of the cost function is not actually achieved and so the closed-loop performance are not optimal in such a sense.

In this chapter the theory underlying the design of the suboptimal control is resumed. Both continuous-time and discrete-time solutions are reported, with and without time delay consideration. A brief outline on optimization algorithms is also provided with the aim of introducing the reader to the numerical methods used in this thesis. Finally, a simple dynamical system is used to validate the software.

4.1 Continuous-time suboptimal control

The continuous-time design of control systems is the most straightforward approach and it is not necessarily limited to an analog implementation. Indeed, the resulting design can be also realized through a digital (discrete-

time) implementation by selecting a sampling frequency high enough to have a discrete-time controller emulating its continuous counterpart.

4.1.1 Problem formulation

The procedure followed in this chapter is related to the mirror assembly model presented in Chapter 2. However, since the mirror model is expressed as a generic linear time-invariant state space system, it can be easily extended to other physical processes.

Rearranging Eq. (2.28), the open loop system dynamics can be written as

$$\begin{cases} \dot{\mathbf{x}} = \mathbf{A}\mathbf{x} + \mathbf{B}\mathbf{v} + \begin{bmatrix} \mathbf{B}_d & \mathbf{B}_n \end{bmatrix} \begin{Bmatrix} \mathbf{f}_d \\ \mathbf{n} \end{Bmatrix} \\ \mathbf{y} = \mathbf{C}\mathbf{x} + \mathbf{D}_n\mathbf{n} \\ \mathbf{z} = \mathbf{C}_z\mathbf{x} \end{cases} \tag{4.1}$$

where $\mathbf{z}$ is the $(n_z \times 1)$ performance vector, containing a combination of state space variables that will fall in the cost function formulation. A separation between force disturbances $\mathbf{f}_d$ and measure noise disturbances $\mathbf{n}$ is retained, in order to underline their different nature and to put in evidence their different influence in the system dynamics.

The direct output optimal feedback control law takes the following form

$$\mathbf{v} = -\mathbf{G}\,\mathbf{y} \tag{4.2}$$

which, using the output equation, can be also written as

$$\mathbf{v} = -\mathbf{G}\mathbf{C}\,\mathbf{x} - \mathbf{G}\mathbf{D}_n\,\mathbf{n} \tag{4.3}$$

At this stage, no specific constraint on the structure of the gain matrix $\mathbf{G}$ is imposed. The related discussion is postponed to section 4.1.4. According to the assumed control law, the closed-loop system dynamics is governed by the following set of equations

$$\begin{cases} \dot{\mathbf{x}} = (\mathbf{A} - \mathbf{B}\mathbf{G}\mathbf{C})\,\mathbf{x} + \begin{bmatrix} \mathbf{B}_d & (\mathbf{B}_n - \mathbf{B}\mathbf{G}\mathbf{D}_n) \end{bmatrix} \begin{Bmatrix} \mathbf{f}_d \\ \mathbf{n} \end{Bmatrix} \\ \mathbf{z} = \mathbf{C}_z\mathbf{x} \\ \mathbf{v} = -(\mathbf{G}\mathbf{C})\,\mathbf{x} - (\mathbf{G}\mathbf{D}_n)\,\mathbf{n} \end{cases} \tag{4.4}$$

In a more compact notation, it can be written as

$$\begin{cases} \dot{\mathbf{x}} = \mathbf{A}_c\,\mathbf{x} + \begin{bmatrix} \mathbf{B}_d & \mathbf{B}_{n,c} \end{bmatrix} \begin{Bmatrix} \mathbf{f}_d \\ \mathbf{n} \end{Bmatrix} \\ \mathbf{z} = \mathbf{C}_z\mathbf{x} \\ \mathbf{v} = -(\mathbf{G}\mathbf{C})\,\mathbf{x} - (\mathbf{G}\mathbf{D}_n)\,\mathbf{n} \end{cases} \tag{4.5}$$

where

$$\mathbf{A}_c = (\mathbf{A} - \mathbf{BGC})$$
$$\mathbf{B}_{n,c} = (\mathbf{B}_n - \mathbf{BGD}_n)$$

4.1.2 Deterministic design

The cost function to be minimized by the controller is expressed as a quadratic form

$$J = \frac{1}{2}\int_0^\infty \left[\mathbf{z}^T\,\mathbf{W}_{zz}\,\mathbf{z} + \mathbf{v}^T\,\mathbf{W}_{vv}\,\mathbf{v}\right]\,dt \tag{4.6}$$

where both $\mathbf{W}_{zz}$ and $\mathbf{W}_{vv}$ are symmetric weighting matrices. $\mathbf{W}_{vv}$ must be a positive definite matrix, whereas $\mathbf{W}_{zz}$ can be positive semi-definite. Their values represent the relative weight between performance and control effort. Usually, the weighting matrices are selected as diagonal matrices, in order to express the cost function as a weighted linear combination of the squares values of the performance and control variables. The presence of the control term in the cost function is used to limit the control action. Indeed, the control problem can be stated as follows: find a stabilizing constant gain matrix $\mathbf{G}$ corresponding to a controller which minimizes the desired performance with the constraint of using a limited amount of control energy. This penalty method is justified by the presence of saturation limits on actuators or, simply, by the need for limiting the energy consumption.

One of the options that can be adopted in the present optimal control design is to consider the closed-loop free system response subjected only to non null initial conditions [30]. In this way, the design is focused on optimizing the transient response, and thus the promptness of the system. Looking at the free response means considering just a state initial condition $\mathbf{x}(0) = \mathbf{x}_0$ as source of system excitation, without any other disturbance or noise. Thus the related simplified closed loop system dynamics becomes

$$\begin{cases} \dot{\mathbf{x}} = \mathbf{A}_c\,\mathbf{x} \\ \mathbf{z} = \mathbf{C}_z\mathbf{x} \\ \mathbf{v} = -(\mathbf{GC})\,\mathbf{x} \end{cases} \tag{4.7}$$

Free response to initial conditions is given by

$$\mathbf{x}(t) = e^{\mathbf{A}_c t}\,\mathbf{x}_0 \tag{4.8}$$

The cost function can be expressed in terms of the state vector only by using the performance equation and the feedback law. Accordingly, J takes the following form

$$J = \frac{1}{2}\int_0^\infty \left[\mathbf{x}^T\,\mathbf{C}_z^T\,\mathbf{W}_{zz}\,\mathbf{C}_z\,\mathbf{x} + \mathbf{x}^T\,\mathbf{C}^T\,\mathbf{G}^T\,\mathbf{W}_{vv}\,\mathbf{G}\,\mathbf{C}\,\mathbf{x}\right]\,dt \tag{4.9}$$

If Eq. (4.8) is substituted into the previous expression of J, the cost function becomes a quadratic form of the initial conditions only as follows

$$J = \frac{1}{2}\mathbf{x}_0^T \left[\int_0^\infty e^{\mathbf{A}_c^T t}\, \mathbf{W}(\mathbf{G})\, e^{\mathbf{A}_c t}\, dt \right] \mathbf{x}_0 \tag{4.10}$$

where

$$\mathbf{W}(\mathbf{G}) = \mathbf{C}_z^T\, \mathbf{W}_{zz}\, \mathbf{C}_z \,+\, \mathbf{C}^T\, \mathbf{G}^T\, \mathbf{W}_{vv}\, \mathbf{G}\, \mathbf{C} \tag{4.11}$$

Let us denote the integral in Eq. (4.10) as the symmetric matrix $\mathbf{P}$. After introducing the trace operator and using the properties of the trace, the cost function thus rearranges as

$$\begin{aligned} J &= \frac{1}{2}\, \mathbf{x}_0^T\, \mathbf{P}\, \mathbf{x}_0 \\ &= \frac{1}{2}\, \mathrm{Tr}\left[\mathbf{x}_0^T\, \mathbf{P}\, \mathbf{x}_0\right] \\ &= \frac{1}{2}\, \mathrm{Tr}\left[\mathbf{P}\, \mathbf{x}_0 \mathbf{x}_0^T\right] \\ &= \frac{1}{2}\, \mathrm{Tr}\left[\mathbf{P}\mathbf{X}_0\right] \end{aligned} \tag{4.12}$$

where $\mathbf{X}_0 = \mathbf{x}_0\mathbf{x}_0^T$. The symmetric matrix $\mathbf{P}$ is constrained to satisfy the following Lyapunov equation

$$\mathbf{A}_c^T\mathbf{P} \,+\, \mathbf{P}\mathbf{A}_c \,+\, \mathbf{W}(\mathbf{G}) = \mathbf{0} \tag{4.13}$$

Therefore, the minimization of J has to be done under the constraint expressed by Eq. (4.13). The cost function is then reformulated as follows

$$J = \frac{1}{2}\, \mathrm{Tr}\left[\mathbf{P}\mathbf{X}_0 + \mathbf{\Lambda}\left(\mathbf{A}_c^T\mathbf{P} \,+\, \mathbf{P}\mathbf{A}_c \,+\, \mathbf{W}(\mathbf{G})\right)\right] \tag{4.14}$$

where $\mathbf{\Lambda}$ is the symmetric matrix of Lagrange multipliers.

Since the cost function now contains three unknown matrices, the solution of the minimization problem requires the matrix equations

$$\begin{cases} \frac{\partial J}{\partial \mathbf{\Lambda}} &= \mathbf{0} \\ \frac{\partial J}{\partial \mathbf{G}} &= \mathbf{0} \\ \frac{\partial J}{\partial \mathbf{P}} &= \mathbf{0} \end{cases} \tag{4.15}$$

These three conditions yields the following set of matrix equations

$$\begin{cases} \mathbf{A}_c^T\mathbf{P} \,+\, \mathbf{P}\mathbf{A}_c \,+\, \mathbf{W}(\mathbf{G}) = \mathbf{0} \\ \mathbf{A}_c\mathbf{\Lambda} \,+\, \mathbf{\Lambda}\mathbf{A}_c^T \,+\, \mathbf{X}_0 = \mathbf{0} \\ -2\mathbf{B}^T\mathbf{P}\mathbf{\Lambda}\mathbf{C}^T + 2\mathbf{W}_{vv}\mathbf{G}\mathbf{C}\mathbf{\Lambda}\mathbf{C}^T = \mathbf{0} \end{cases} \tag{4.16}$$

which has to be solved to determine the gain matrix $\mathbf{G}$. It is noted that the system to be solved is a nonlinear fully coupled system. Many numerical methods are available in the literature to find the solution.

An alternative approach is a gradient-based direct numerical optimization of the cost function. In this case, J is expressed as

$$J = \frac{1}{2}\,\mathrm{Tr}\left[\mathbf{P}\mathbf{X}_0\right] \tag{4.17}$$

where the $\mathbf{P}$ matrix comes from the solution of Eq. (4.13). The gradient instead takes a little bit more of calculations. Knowing that

$$\mathrm{grad}\, J = \frac{\partial J}{\partial \mathbf{G}} = \begin{bmatrix} \\ \frac{\partial J}{\partial g_{ij}} \\ \\ \end{bmatrix} \tag{4.18}$$

the core of the problem lies in finding $\frac{\partial J}{\partial g_{ij}}$, which can be expressed as

$$\frac{\partial J}{\partial g_{ij}} = \frac{1}{2}\,Tr\left[\frac{\partial \mathbf{P}}{\partial g_{ij}}\,\mathbf{X}_0\right] \tag{4.19}$$

The derivatives of $\mathbf{P}$ can be obtained by differentiating Eq. (4.13). It follows that

$$\mathbf{A}_c^T\frac{\partial \mathbf{P}}{\partial g_{ij}} + \frac{\partial \mathbf{P}}{\partial g_{ij}}\mathbf{A}_c + \frac{\partial \mathbf{A}_c^T}{\partial g_{ij}}\mathbf{P} + \mathbf{P}\frac{\partial \mathbf{A}_c}{\partial g_{ij}} + \frac{\partial \mathbf{W}(\mathbf{G})}{\partial g_{ij}} = \mathbf{0} \tag{4.20}$$

This is again a Lyapunov equation which has to be solved for each element of the gain matrix. In order to avoid solving as many Lyapunov equations as the number of control gains, a different formulation of the gradient can be used. Considering the second equation of system 4.16 and exploiting the properties of the trace operator, each element of the gradient can be written as

$$\begin{aligned}
\frac{\partial J}{\partial g_{ij}} &= \frac{1}{2}\,\mathrm{Tr}\left[\frac{\partial \mathbf{P}}{\partial g_{ij}}\,\mathbf{X}_0\right] \\
&= -\frac{1}{2}\,\mathrm{Tr}\left[\frac{\partial \mathbf{P}}{\partial g_{ij}}\,\left(\mathbf{A}_c\mathbf{\Lambda} + \mathbf{\Lambda}\mathbf{A}_c^T\right)\right] \\
&= -\frac{1}{2}\,\mathrm{Tr}\left[\mathbf{\Lambda}\frac{\partial \mathbf{P}}{\partial g_{ij}}\mathbf{A}_c + \mathbf{\Lambda}\mathbf{A}_c^T\frac{\partial \mathbf{P}}{\partial g_{ij}}\right] \\
&= -\frac{1}{2}\,\mathrm{Tr}\left[\mathbf{\Lambda}\left(\frac{\partial \mathbf{P}}{\partial g_{ij}}\mathbf{A}_c + \mathbf{A}_c^T\frac{\partial \mathbf{P}}{\partial g_{ij}}\right)\right] \\
&= \frac{1}{2}\,\mathrm{Tr}\left[\mathbf{\Lambda}\left(\frac{\partial \mathbf{A}_c^T}{\partial g_{ij}}\mathbf{P} + \mathbf{P}\frac{\partial \mathbf{A}_c}{\partial g_{ij}} + \frac{\partial \mathbf{W}(\mathbf{G})}{\partial g_{ij}}\right)\right]
\end{aligned} \tag{4.21}$$

Since the only matrix that actually changes for each (i, j) element is $\frac{\partial \mathbf{G}}{\partial g_{ij}}$, the gradient expression could be further elaborated till reaching

$$\frac{\partial J}{\partial g_{ij}} = \frac{1}{2} \operatorname{Tr} \left[\mathbf{M}_1 \frac{\partial \mathbf{G}}{\partial g_{ij}} \right] \tag{4.22}$$

where

$$\mathbf{M}_1 = 2 \left(\mathbf{C} \mathbf{\Lambda} \mathbf{C}^T \mathbf{G}^T \mathbf{W}_{vv} \, - \, \mathbf{C} \mathbf{\Lambda} \mathbf{P} \mathbf{B} \right) \tag{4.23}$$

The matrix $\mathbf{M}_1$ can be computed only once. Therefore, a numerically efficient code is obtained since only one matrix product is needed in each gradient element.

4.1.3 Stochastic design

The previous design is based on the deterministic response of the system to initial conditions. A different approach can be used which leads to a so-called stochastic design of the suboptimal control.

Instead of exciting the system with non-null initial conditions, corresponding to impulse-like perturbations at $t = 0$, and then optimizing the transient response, one can assume the system subjected to random inputs having prescribed statistical properties and then optimize the steady state stochastic response. In particular, the random disturbances are assumed as ergodic white noises with zero mean values. The corresponding cost function can be expressed as

$$J = \frac{1}{2} E \left[\mathbf{z}^T \, \mathbf{W}_{zz} \, \mathbf{z} \, + \, \mathbf{v}^T \, \mathbf{W}_{vv} \, \mathbf{v} \right] \tag{4.24}$$

where E is the expected value operator. Starting from this cost function, a procedure similar to the deterministic case can be followed. The design model is now the model described in Eqs. (4.5), where $\mathbf{f}_d$ and $\mathbf{n}$ are white noise ergodic processes.

Substituting the closed loop dynamics and the control law expression, it is possible to rewrite Eq. (4.24) as

$$J = \frac{1}{2} E \left[\mathbf{x}^T \, \mathbf{W}(\mathbf{G}) \, \mathbf{x} \right] \tag{4.25}$$

where again

$$\mathbf{W}(\mathbf{G}) = \mathbf{C}_z^T \, \mathbf{W}_{zz} \, \mathbf{C}_z \, + \, \mathbf{C}^T \, \mathbf{G}^T \, \mathbf{W}_{vv} \, \mathbf{G} \, \mathbf{C}$$

Introducing the trace operator and exploiting its properties yields

$$\begin{aligned} J &= \frac{1}{2}\mathrm{Tr}\left\{E\left[\mathbf{x}^T\,\mathbf{W}(\mathbf{G})\,\mathbf{x}\right]\right\} \\ &= \frac{1}{2}E\left\{\mathrm{Tr}\left[\mathbf{x}^T\,\mathbf{W}(\mathbf{G})\,\mathbf{x}\right]\right\} \\ &= \frac{1}{2}E\left\{\mathrm{Tr}\left[\mathbf{W}(\mathbf{G})\,\mathbf{x}\,\mathbf{x}^T\right]\right\} \\ &= \frac{1}{2}\mathrm{Tr}\left\{E\left[\mathbf{W}(\mathbf{G})\,\mathbf{x}\,\mathbf{x}^T\right]\right\} \\ &= \frac{1}{2}\mathrm{Tr}\left\{\,\mathbf{W}(\mathbf{G})E\left[\mathbf{x}\,\mathbf{x}^T\right]\right\} \\ &= \frac{1}{2}\mathrm{Tr}\left\{\,\mathbf{W}(\mathbf{G})\boldsymbol{\sigma}_{xx}^2\right\} \end{aligned} \tag{4.26}$$

Here, $\boldsymbol{\sigma}_{xx}^2$ denotes the state variance matrix. For an ergodic random process, the state variance satisfies the following Lyapunov equation

$$\mathbf{A}_c\boldsymbol{\sigma}_{xx}^2 \,+\, \boldsymbol{\sigma}_{xx}^2\mathbf{A}_c^T \,+\, \mathbf{W}_2(\mathbf{G}) = \mathbf{0} \tag{4.27}$$

where

$$\mathbf{W}_2(\mathbf{G}) = \mathbf{B}_d\,\mathbf{W}_{dd}\,\mathbf{B}_d^T \,+\, \left(\mathbf{B}_n - \mathbf{B}\mathbf{G}\mathbf{D}_n\right)\,\mathbf{W}_{nn}\,\left(\mathbf{B}_n - \mathbf{B}\mathbf{G}\mathbf{D}_n\right)^T \tag{4.28}$$

and $\mathbf{W}_{dd}$ and $\mathbf{W}_{nn}$ are, respectively, the intensity of the disturbance force and measure noise. It is noted that the intensity of the noise can be considered as a tunable weighting quantity to be used as a design variable for the optimization of the controller.

Since J is expressed through the state variance matrix, which satisfies a Lyapunov equation, the minimization procedure applies to the following cost function

$$J = \frac{1}{2}Tr\left[\,\mathbf{W}(\mathbf{G})\boldsymbol{\sigma}_{xx}^2 \,+\, \boldsymbol{\Lambda}\left(\mathbf{A}_c\boldsymbol{\sigma}_{xx}^2 \,+\, \boldsymbol{\sigma}_{xx}^2\mathbf{A}_c^T \,+\, \mathbf{W}_2(\mathbf{G})\right)\right] \tag{4.29}$$

where $\boldsymbol{\Lambda}$ is the symmetric matrix of Lagrange multipliers. The minimum of J is obtained when

$$\begin{cases} \frac{\partial J}{\partial \boldsymbol{\Lambda}} = \mathbf{0} \\ \frac{\partial J}{\partial \mathbf{G}} = \mathbf{0} \\ \frac{\partial J}{\partial \boldsymbol{\sigma}_{xx}^2} = \mathbf{0} \end{cases} \tag{4.30}$$

As in the previous deterministic design, a direct numerical optimization is again proposed. The cost function to be minimized is

$$J = \frac{1}{2}\,\mathrm{Tr}\left[\mathbf{W}(\mathbf{G})\boldsymbol{\sigma}_{xx}^2\right] \tag{4.31}$$

The steps to compute the gradient of J are very similar to the deterministic design previously discussed. It follows that

$$\frac{\partial J}{\partial g_{ij}} = \frac{1}{2}\,\mathrm{Tr}\left[\frac{\partial \mathbf{W}(\mathbf{G})}{\partial g_{ij}}\boldsymbol{\sigma}^2_{xx} + \frac{\partial \boldsymbol{\sigma}^2_{xx}}{\partial g_{ij}}\mathbf{W}(\mathbf{G})\right] \tag{4.32}$$

The derivative of the variance matrix can be expressed by considering the third equation of the system 4.30

$$\mathbf{A}_c^T\boldsymbol{\Lambda} + \boldsymbol{\Lambda}\mathbf{A}_c + \mathbf{W}(\mathbf{G}) = \mathbf{0} \tag{4.33}$$

Differentiation of the previous equation yields

$$\mathbf{A}_c\frac{\partial \boldsymbol{\sigma}^2_{xx}}{\partial g_{ij}} + \frac{\partial \boldsymbol{\sigma}^2_{xx}}{\partial g_{ij}}\mathbf{A}_c^T + \frac{\partial \mathbf{A}_c}{\partial g_{ij}}\boldsymbol{\sigma}^2_{xx} + \boldsymbol{\sigma}^2_{xx}\frac{\partial \mathbf{A}_c^T}{\partial g_{ij}} + \frac{\partial \mathbf{W}_2(\mathbf{G})}{\partial g_{ij}} = \mathbf{0} \tag{4.34}$$

Accordingly, the gradient is given by

$$\begin{aligned}\frac{\partial J}{\partial g_{ij}} &= \frac{1}{2}\,\mathrm{Tr}\left[\frac{\partial \mathbf{W}(\mathbf{G})}{\partial g_{ij}}\boldsymbol{\sigma}^2_{xx} - \frac{\partial \boldsymbol{\sigma}^2_{xx}}{\partial g_{ij}}\left(\mathbf{A}_c^T\boldsymbol{\Lambda} + \boldsymbol{\Lambda}\mathbf{A}_c\right)\right] \\ &= \frac{1}{2}\,\mathrm{Tr}\left[\frac{\partial \mathbf{W}(\mathbf{G})}{\partial g_{ij}}\boldsymbol{\sigma}^2_{xx} - \boldsymbol{\Lambda}\left(\frac{\partial \boldsymbol{\sigma}^2_{xx}}{\partial g_{ij}}\mathbf{A}_c^T + \mathbf{A}_c\frac{\partial \boldsymbol{\sigma}^2_{xx}}{\partial g_{ij}}\right)\right] \\ &= \frac{1}{2}\,\mathrm{Tr}\left[\frac{\partial \mathbf{W}(\mathbf{G})}{\partial g_{ij}}\boldsymbol{\sigma}^2_{xx} + \boldsymbol{\Lambda}\left(\frac{\partial \mathbf{A}_c}{\partial g_{ij}}\boldsymbol{\sigma}^2_{xx} + \boldsymbol{\sigma}^2_{xx}\frac{\partial \mathbf{A}_c^T}{\partial g_{ij}} + \frac{\partial \mathbf{W}_2(\mathbf{G})}{\partial g_{ij}}\right)\right]\end{aligned} \tag{4.35}$$

It can be again rearranged as

$$\frac{\partial J}{\partial g_{ij}} = \frac{1}{2}\,Tr\left[\mathbf{M}_1\frac{\partial \mathbf{G}}{\partial g_{ij}}\right] \tag{4.36}$$

where

$$\mathbf{M}_1 = 2\left[\left(\mathbf{W}_{vv}\mathbf{G}\mathbf{C}\boldsymbol{\sigma}^2_{xx}\mathbf{C}^T\right)^T - \mathbf{C}\boldsymbol{\sigma}^2_{xx}\boldsymbol{\Lambda}\mathbf{B} - \mathbf{D}_n\mathbf{W}_{nn}\left(\mathbf{B}_n - \mathbf{B}\mathbf{G}\mathbf{D}_n\right)^T\boldsymbol{\Lambda}\mathbf{B}\right] \tag{4.37}$$

4.1.4 Numerical solution of the optimal control problem

As already outlined in the previous section, the control problem expressed by searching for the minimum value of the cost functions in Eq. (4.17) and Eq. (4.31) has been solved through a numerical optimization procedure. In particular, the numerical solution has been implemented using MATLAB embedded optimization algorithms.

The solution of the deterministic design is carried out by performing the following five steps:

1. solve the Lyapunov equation Eq. (4.13) to find $\mathbf{P}$
2. compute the cost function J using Eq. (4.17)
3. solve the Lyapunov equation in the matrix $\mathbf{\Lambda}$ (second equation of the set (4.16))
4. compute the matrix $\mathbf{M}_1$ as given by Eq. (4.23)
5. compute the gradient of J according to Eq. (4.22)

It should be noted that, since the above procedure involves quantities that are functions of the elements of the gain matrix, it is possible to impose a prescribed structure to the gain matrix and obtain the corresponding suboptimal solution. In particular, one can assume that some elements of the gain matrix are null. In this way, the designer can force that a control input is coupled to some measurements and is not coupled with others. This partial centralization of the control architecture can also become a fully decentralized co-located scheme if a control channel is coupled only with the mated co-located sensor, i.e., the only non-null gains are the diagonal elements of $\mathbf{G}$. The possibilities offered by this approach are nearly infinite. For example, one can also impose that a fully decentralized architecture is realized with a single gain being used for all the co-located sensor-actuator pairs or with gains organized by clusters defined according to their geometrical distribution over the mirror.

This freedom was exploited by writing a MATLAB function which receives as input only the non-null gains of the $\mathbf{G}$ matrix and the information on their positions inside $\mathbf{G}$. This function then calls an additional external script that, from the above informations, builds the actual gain matrix to be used in the computation of J and grad J.

It should be highlighted that such a manipulation of the $\mathbf{G}$ matrix is allowed only when the control problem is solved by a direct numerical optimization procedure.

The computational steps to be performed in the stochastic design are similar to the deterministic case and are reported here for the sake of completeness:

1. solve the Lyapunov equation (4.27) to compute the variance matrix $\boldsymbol{\sigma}_{xx}^2$
2. compute J using Eq. (4.31)
3. solve the Lyapunov equation in $\mathbf{\Lambda}$ from the set (4.33)

4. compute $\mathbf{M}_1$ from Eq. (4.37)

5. compute the gradient of J according to Eq. (4.36)

The same considerations on imposing particular rules to matrix $\mathbf{G}$ can be also done for the stochastic problem.

4.2 Optimization Algorithms

Two main optimization algorithms available in the MATLAB Optimization Toolbox have been specifically adopted in this thesis. This section summarizes the theory behind the two tools and some guidelines on their usage and performance are provided.

Both methods are embedded in the MATLAB function `fminunc`. The first method is a Quasi-Newton Method exploiting the BFGS formula for the Hessian approximation update. The second method is the so-called Trust Region Method based on the preconditioned conjugate gradient. As the name of the MATLAB function implies, an unconstrained optimization is carried out. A good choice for the initial guess $\mathbf{g}_0$ is required to obtain reliable results. Starting from this guess, the algorithms perform a series of iterations until the difference of values of J between two iterations is within a prescribed tolerance. The main differences between the two methods are the rules followed to move from one iterate to the next one.

In parallel with these algorithms a second order method, already applied to a suboptimal control design [31], has been tested on the problem at hand. Results showed the extreme efficiency of the implemented code, that anyway has not been fully integrated in the developed software.

4.2.1 The BFGS method

The BFGS method [32, 33] is one of the most popular Quasi-Newton methods for optimization. Named after its inventors, Broyden, Fletcher, Goldfarb, and Shanno, it is part of a wider category of methods called line search methods. The logic behind the method is based on the choice of the iterate search direction $\mathbf{p}_k$, along which a minimum of the objective function f is identified

$$min\, f(\mathbf{x}_k + \alpha \mathbf{p}_k) \tag{4.38}$$

The peculiarity of Quasi-Newton methods is the choice of the search direction. It is done, like every Newton method, using a second-order Taylor

series representation of $f(\mathbf{x}_k + \mathbf{p}_k)$, but with a second order term containing an approximation $\mathbf{B}_k$ of the Hessian $\boldsymbol{\nabla}^2 f_k$, rather than true Hessian itself

$$f(\mathbf{x}_k + \mathbf{p}_k) \approx f(\mathbf{x}_k) + \boldsymbol{\nabla} f(\mathbf{x}_k)^T \mathbf{p}_k + \frac{1}{2}\mathbf{p}_k^T \mathbf{B}_k \mathbf{p}_k \triangleq m(\mathbf{p}_k) \tag{4.39}$$

The optimal solution of the model $m(\mathbf{p}_k)$ can be found simply by setting to zero its first derivative. Thus

$$\mathbf{p}_k = -\mathbf{B}_k^{-1}\, \boldsymbol{\nabla} f(\mathbf{x}_k) \tag{4.40}$$

and then, according to Eq. (4.38), the following iterate is computed with

$$\mathbf{x}_{k+1} = \mathbf{x}_k + \alpha \mathbf{p}_k \tag{4.41}$$

In the BFGS method, the Hessian approximation is updated at each iteration according to the following recursive formula

$$\mathbf{B}_{k+1} = \mathbf{B}_k - \frac{\mathbf{B}_k \mathbf{s}_k \mathbf{s}_k^T \mathbf{B}_k}{\mathbf{s}_k^T \mathbf{B}_k \mathbf{s}_k} + \frac{\mathbf{y}_k \mathbf{y}_k^T}{\mathbf{y}_k^T \mathbf{s}_k} \tag{4.42}$$

with

$$\mathbf{s}_k = \mathbf{x}_{k+1} - \mathbf{x}_k \qquad\qquad \mathbf{y}_k = \boldsymbol{\nabla} f_{k+1} - \boldsymbol{\nabla} f_k$$

that is an efficient procedure for updating curvature information of the model. This method requires only the gradient to be supplied. Furthermore, the absence of the Hessian request makes this method producing low computational cost algorithms.

4.2.2 The Trust Region Method

In Trust Region methods [32], the main idea is creating an approximate model of the objective function around the current point. Then, the optimal solution of this simplified expression is found. Iterating these steps, the algorithm arrives sufficiently near to the optimum values of the objective function. In addition, the peculiarity of this method is the presence of a trust region, that is a bounded space around the current iterate, where the solution is sought. The size of this region is not static, in order not to excessively limit the convergence rate and, on the opposite side, to avoid proceeding with too hasty steps, that could lead far from the optimum. The radius of the region is tuned at each step according to a simple logic: if the decrease in the objective function is large enough, the size can be increased, whereas, if the iterate is not satisfactory, it should be concluded that the trust region is too large and, consequently, the boundary is restricted. The shape of this

region can not only assume spherical boundaries, but also elliptical ones, in order to better follow the different trends given to the function by all the variables.

According to all what just mentioned, the model resembling the objective function around the iterate $\mathbf{x}_k$ can be written as

$$m(\mathbf{p}_k) = f_k + \mathbf{p}_k^T \mathbf{g}_k + \frac{1}{2}\mathbf{p}_k^T \mathbf{B}_k \mathbf{p}_k \tag{4.43}$$

where $\mathbf{g}_k$ is the gradient of the function and $\mathbf{B}_k$ the Hessian or its finite-difference approximation. Consequently, the minimization problem within the trust region is

$$min \left\{ \psi(\mathbf{p}_k) = \mathbf{p}_k^T \mathbf{g}_k + \tfrac{1}{2}\mathbf{p}_k^T \mathbf{B}_k \mathbf{p}_k \quad : \parallel D_k \mathbf{p}_k \parallel \leq \mathbf{\Delta}_k \right\} \tag{4.44}$$

Differences among methods falling within this category lie in how this minimization problem is solved and in the choice of the approximation model. The MATLAB `fminunc` provides a trust region algorithm [33] based on a two-dimensional subspace solution of problem (4.44). Once the subspace S is computed, the eigensystem problem required to solve the sub-problem becomes trivial, presenting only two dimensions. The most complex aspect of this procedure is identifying the subspace S. The solver at hand defines S as the linear space spanned by $\mathbf{s}_1$ and $\mathbf{s}_2$, where $\mathbf{s}_1$ is in the direction of the gradient $\mathbf{g}$, and $\mathbf{s}_2$ is an approximate Newton direction, i.e., a solution to

$$\mathbf{H}\,\mathbf{s}_2 = -\mathbf{g} \tag{4.45}$$

or, alternatively, the direction of negative curvature

$$\mathbf{s}_2^T\,\mathbf{H}\,\mathbf{s}_2 < 0 \tag{4.46}$$

The philosophy behind this choice of S is to force global convergence via steepest descent direction or negative curvature direction and, at the same time, achieve fast local convergence via Newton step, when it exists. Note also that the problem (4.45) is solved using the method of Preconditioned Conjugate Gradients (PCG).

Finally, after the solution of the sub-problem (4.44), the effective decrease in the cost function is computed and, accordingly, the trust region is updated. Defining

$$\rho_k^f = \frac{f(\mathbf{x}_{k+1}) - f(\mathbf{x}_k)}{\psi(\mathbf{s}_k)} \tag{4.47}$$

the rules for modifying the size $\mathbf{\Delta}_{k+1}$ of the region are:
let $0 < \gamma_1 < 1 < \gamma_2$

1. if $\rho_k^f \leq \mu$ then set $\boldsymbol{\Delta}_{k+1} \in (0, \gamma_1 \boldsymbol{\Delta}_k]$
2. if $\rho_k^f \in (\mu, \eta)$ then set $\boldsymbol{\Delta}_{k+1} \in [\gamma_1 \boldsymbol{\Delta}_k, \boldsymbol{\Delta}_k]$
3. if $\rho_k^f \geq \eta$ then set $\boldsymbol{\Delta}_{k+1} \in [\boldsymbol{\Delta}_k, \gamma_2 \boldsymbol{\Delta}_k]$

Computationally this method results more onerous, because of the use of the Hessian that, if not directly furnished by the user, is numerically approximated by means of finite differences. With respect to the BFGS method, it is mandatory to provide the gradient expression.

4.3 Discrete-time suboptimal control

The suboptimal control can be also designed using a discrete-time formulation. The related equations are presented in this section.

The discrete-time formulation considers piecewise step inputs and outputs, as it happens in practical digital implementations. When high sampling frequencies are adopted, a feedback controller designed according to a continuous-time formulation behaves very similarly to a discrete-time control system. In this case, the digitalization of the input and output variables can be viewed as a noise source. However, as the frequency at which the control is paced decreases, the difference between continuous-time and discrete-time control designs becomes large. Thus the continuous-time optimal gains are not only far from the optimal gains of the discrete case, but a closed-loop instability can even occur.

For a time-discrete design, the dynamic system described in section 4.1.1 must be reformulated. This has to be done both for the deterministic and the stochastic design approach. The first step is to rewrite the dynamics of the system in terms of finite-difference equations [30, 34]. Therefore, the exact discrete-time representation of the model is the following

$$\begin{cases} \mathbf{x}_{k+1} = \mathbf{A}^d \, \mathbf{x}_k \, + \, \mathbf{B}^d \, \mathbf{u}_k \, + \, \mathbf{B}_{dn}^d \, \mathbf{d}_k \\ \mathbf{y}_k = \mathbf{C} \, \mathbf{x}_k \end{cases} \tag{4.48}$$

in which, for a zero-order hold, the discrete matrices are given by

$$\mathbf{A}^d = e^{\mathbf{A}\Delta t}, \quad \mathbf{B}^d = \int_0^{\Delta t} e^{\mathbf{A}\eta} \, \mathbf{B} \, d\eta, \quad \mathbf{B}_{dn}^d = \int_0^{\Delta t} e^{\mathbf{A}\eta} \, \mathbf{B}_{dn} \, d\eta$$

with the synthetic representation of

$$\mathbf{B}_{dn} = \begin{bmatrix} \mathbf{B}_d & \mathbf{B}_n \end{bmatrix} \qquad \mathbf{d} = \begin{Bmatrix} \mathbf{f}_d \\ \mathbf{n} \end{Bmatrix} \tag{4.49}$$

Here Δt is the constant sampling period and $\eta = (k+1)\Delta t - \tau$. Whereas, k and $k+1$ identify the related variable at two successive time instants $k\,\Delta t$ and $(k+1)\,\Delta t$.

It should be stressed that the above representation correctly describes the piecewise constant control action, but nevertheless it approximates the also disturbances $\mathbf{d}$ in the same way. Even if this approximation is not realistic, it is commonly accepted.

In the discrete-time formulation, the control law takes the form

$$\mathbf{v}_k = -\mathbf{G}\,\mathbf{y}_k = -\mathbf{G}\,\mathbf{C}\,\mathbf{x}_k \tag{4.50}$$

and, as a result, the closed loop dynamics become

$$\begin{cases} \mathbf{x}_{k+1} = \mathbf{A}_c^d\,\mathbf{x}_k + \mathbf{B}_{dn}^d\mathbf{d}_k \\ \mathbf{z}_k = \mathbf{C}_z\mathbf{x}_k \\ \mathbf{v} = -(\mathbf{GC})\,\mathbf{x}_k \end{cases} \tag{4.51}$$

with

$$\mathbf{A}_c^d = (\mathbf{A}^d - \mathbf{B}^d\mathbf{GC})$$

4.3.1 Deterministic design

In addition to the system dynamics, also the cost function has to be reformulated [30, 34, 35]. The result is that the time integral transforms into a summation

$$J = \frac{1}{2}\sum_{k=0}^{\infty}\left[\mathbf{z}_k^T\,\mathbf{W}_{zz}\,\mathbf{z}_k \;+\; \mathbf{v}_k^T\,\mathbf{W}_{vv}\,\mathbf{v}_k\right] \tag{4.52}$$

After using the control law and the performance equation, the cost function can be written in terms of the state vector only as follows

$$J = \frac{1}{2}\sum_{k=0}^{\infty}\left[\mathbf{x}_k^T(\mathbf{C}_z^T\mathbf{W}_{zz}\mathbf{C}_z + \mathbf{C}^T\mathbf{G}^T\mathbf{W}_{vv}\mathbf{GC})\mathbf{x}_k\right] \tag{4.53}$$

The discrete-time response of the closed-loop system in Eq. (4.51) to generic initial conditions $\mathbf{x}_0$ is given by

$$\mathbf{x}_k = (\mathbf{A}_c^d)^k\mathbf{x}_0 \tag{4.54}$$

Substituting the above into the cost function yields

$$J = \frac{1}{2}\,\mathbf{x}_0\sum_{k=0}^{\infty}\left\{\left[(\mathbf{A}_c^d)^k\right]^T\mathbf{W}(\mathbf{G})(\mathbf{A}_c^d)^k\right\}\mathbf{x}_0 \tag{4.55}$$

It is now possible to apply the trace operator to the J expression and write

$$J = \frac{1}{2}\,\mathrm{Tr}\left[\mathbf{x}_0^T\mathbf{H}\mathbf{x}_0\right] = \frac{1}{2}\,\mathrm{Tr}\left[\mathbf{H}\mathbf{X}_0\right] \tag{4.56}$$

where

$$\mathbf{H} = \sum_{k=0}^{\infty}\left[((\mathbf{A}_c^d)^k)^T\mathbf{W}(\mathbf{G})(\mathbf{A}_c^d)^k\right]\,, \qquad \mathbf{X}_0 = \mathbf{x}_0\mathbf{x}_0^T$$

The matrix $\mathbf{H}$ included in the cost function J satisfies the following relation [34]

$$(\mathbf{A}_c^d)^T\mathbf{H}\mathbf{A}_c^d - \mathbf{H} = \lim_{k\to\infty}\left\{\left[(\mathbf{A}_c^d)^k\right]^T\mathbf{H}(\mathbf{A}_c^d)^k\right\} - \mathbf{W}(\mathbf{G}) \tag{4.57}$$

Now, if the closed-loop system is asymptotically stable, the matrix $\mathbf{A}_c$ has spectral radius lower than one. Therefore, the limit in the above relation goes to zero. It follows that the matrix $\mathbf{H}$ is a solution of

$$(\mathbf{A}_c^d)^T\mathbf{H}\mathbf{A}_c^d - \mathbf{H} + \mathbf{W}(\mathbf{G}) = \mathbf{0} \tag{4.58}$$

This is a discrete Lyapunov equation and can be considered the discrete-time version of the continuos-time Lyapunov equation (4.13).

It is clear that the cost function to be minimized takes the form

$$J = \frac{1}{2}\,\mathrm{Tr}\left[\mathbf{H}\mathbf{X}_0 \,+\, \mathbf{\Lambda}\left((\mathbf{A}_c^d)^T\mathbf{H}\mathbf{A}_c^d - \mathbf{H} + \mathbf{W}(\mathbf{G})\right)\right] \tag{4.59}$$

where the equation governing the $\mathbf{H}$ matrix has been included in the free minimization problem as a constraint through the symmetric matrix of Lagrange multipliers $\mathbf{\Lambda}$. The solution of the above problem follows the same steps as the continuous-time case, and thus presents the same limitations. Here, only the approach based on the direct numerical optimization of J as expressed in Eq. (4.56) is described.

The matrix $\mathbf{H}$ is determined by solving the discrete Lyapunov equation (4.58). From Eq. (4.59), the derivative $\frac{\partial J}{\partial \mathbf{H}}$ gives

$$\mathbf{A}_c^d\mathbf{\Lambda}(\mathbf{A}_c^d)^T - \mathbf{\Lambda} + \mathbf{X}_0 = \mathbf{0} \tag{4.60}$$

Then, with a little bit of algebra, the gradient of J is computed as

$$\begin{aligned}\frac{\partial J}{\partial g_{ij}} &= \frac{1}{2}\,\mathrm{Tr}\left[\frac{\partial \mathbf{H}}{\partial g_{ij}}\mathbf{X}_0\right] \\ &= \frac{1}{2}\,\mathrm{Tr}\left[\frac{\partial \mathbf{H}}{\partial g_{ij}}\left(\mathbf{\Lambda} - \mathbf{A}_c^d\mathbf{\Lambda}(\mathbf{A}_c^d)^T\right)\right] \\ &= \frac{1}{2}\,\mathrm{Tr}\left[\mathbf{\Lambda}\left(\frac{\partial \mathbf{H}}{\partial g_{ij}} - (\mathbf{A}_c^d)^T\frac{\partial \mathbf{H}}{\partial g_{ij}}\mathbf{A}_c^d\right)\right]\end{aligned} \tag{4.61}$$

By differentiation of Eq. (4.58), we have

$$(\mathbf{A}_c^d)^T \frac{\partial \mathbf{H}}{\partial g_{ij}} \mathbf{A}_c^d - \frac{\partial \mathbf{H}}{\partial g_{ij}} + (\frac{\partial \mathbf{A}_c^d}{\partial g_{ij}})^T \mathbf{H} \mathbf{A}_c^d + (\mathbf{A}_c^d)^T \mathbf{H} \frac{\partial \mathbf{A}_c^d}{\partial g_{ij}} + \mathbf{W}(\mathbf{G}) = \mathbf{0} \quad (4.62)$$

The partial derivative of the cost function can thus be rewritten as

$$\frac{\partial J}{\partial g_{ij}} = \frac{1}{2} \operatorname{Tr} \left[\mathbf{\Lambda} \left((\frac{\partial \mathbf{A}_c^d}{\partial g_{ij}})^T \mathbf{H} \mathbf{A}_c^d + (\mathbf{A}_c^d)^T \mathbf{H} \frac{\partial \mathbf{A}_c^d}{\partial g_{ij}} + \mathbf{W}(\mathbf{G}) \right) \right] \quad (4.63)$$

Rearranging

$$\frac{\partial J}{\partial g_{ij}} = \frac{1}{2} \operatorname{Tr} \left[\mathbf{M}_1 \frac{\partial \mathbf{G}}{\partial g_{ij}} \right] \quad (4.64)$$

with

$$\mathbf{M}_1 = 2 \left[\mathbf{C} \mathbf{\Lambda} \left(\mathbf{C}^T \mathbf{G}^T \mathbf{W}_{vv} - (\mathbf{A}_c^d)^T \mathbf{H} \mathbf{B}^d \right) \right] \quad (4.65)$$

It should be noted that the discrete-time design resembles the same procedure and solution of the continuous-time version. The great difference lies in the discrete form of Lyapunov equations involved in the computation of the cost function and its derivatives, replacing their continuous counterparts.

4.3.2 Stochastic design

The discrete version of the stochastic design discussed in section 4.1.3 is here presented. As for the deterministic design outlined before, a procedure completely similar to the continuous-time formulation is expected, with now discrete Lyapunov equations instead of the continuous counterparts.

The first step to properly formulate the problem is to define a cost function expressed through stochastic discrete variables [30, 36]. A suitable form is

$$J = \frac{1}{2} \lim_{N \to \infty} \left\{ \frac{1}{N} E \left[\sum_{k=0}^{N} \left(\mathbf{z}_k^T \, \mathbf{W}_{zz} \, \mathbf{z}_k \, + \, \mathbf{v}_k^T \, \mathbf{W}_{vv} \, \mathbf{v}_k \right) \right] \right\} \quad (4.66)$$

Using as before the control law and performance equation, it is possible to write the quadratic form in terms only of the state vector at instant k. Taking the trace operator and exploiting its properties, J can be written as

$$J = \frac{1}{2} \lim_{N \to \infty} \left\{ \operatorname{Tr} \left[\mathbf{W}(\mathbf{G}) \boldsymbol{\sigma}_{xx,k}^2 \right] \right\} \quad (4.67)$$

Since we are dealing with ergodic white noise processes, the limit value of the variance matrix assumes a constant value. So, the cost function is given by

$$J = \frac{1}{2} \operatorname{Tr} \left[\mathbf{W}(\mathbf{G}) \, \overline{\boldsymbol{\sigma}}_{xx}^2 \right] \quad (4.68)$$

The value of $\overline{\boldsymbol{\sigma}}^2_{xx}$ is determined from the closed-loop dynamics. It can be shown [30, 37] that the steady state variance matrix satisfies the following equation

$$\mathbf{A}_c^d \overline{\boldsymbol{\sigma}}^2_{xx} (\mathbf{A}_c^d)^T - \overline{\boldsymbol{\sigma}}^2_{xx} + \mathbf{W}_3(\mathbf{G}) = \mathbf{0} \tag{4.69}$$

where

$$\mathbf{W}_3(\mathbf{G}) = \mathbf{B}_d^d \, \mathbf{W}_{dd} \, (\mathbf{B}_d^d)^T \; + \; \left(\mathbf{B}_n^d - \mathbf{B}^d \mathbf{G} \mathbf{D}_n^d\right) \, \mathbf{W}_{nn} \, \left(\mathbf{B}_n^d - \mathbf{B}^d \mathbf{G} \mathbf{D}_n^d\right)^T \tag{4.70}$$

Accordingly, after introducing the matrix of Lagrange multipliers $\boldsymbol{\Lambda}$, the free minimization problem is rewritten as

$$J = \frac{1}{2} \operatorname{Tr} \left[\mathbf{W}(\mathbf{G}) \, \overline{\boldsymbol{\sigma}}^2_{xx} + \boldsymbol{\Lambda} \left((\mathbf{A}_c^d)^T \overline{\boldsymbol{\sigma}}^2_{xx} \mathbf{A}_c^d - \overline{\boldsymbol{\sigma}}^2_{xx} + \mathbf{W}_3(\mathbf{G}) \right) \right] \tag{4.71}$$

Setting to zero the derivative of J with respect to the state variance matrix yields the discrete Lyapunov equation to compute $\boldsymbol{\Lambda}$

$$(\mathbf{A}_c^d)^T \boldsymbol{\Lambda} \mathbf{A}_c^d - \boldsymbol{\Lambda} + \mathbf{W}(\mathbf{G}) = \mathbf{0} \tag{4.72}$$

The gradient of J as expressed by Eq. (4.68) is given by

$$\begin{aligned} \frac{\partial J}{\partial g_{ij}} &= \frac{1}{2} \operatorname{Tr} \left[\frac{\partial \mathbf{W}(\mathbf{G})}{\partial g_{ij}} \, \overline{\boldsymbol{\sigma}}^2_{xx} \; + \; \mathbf{W}(\mathbf{G}) \, \frac{\partial \overline{\boldsymbol{\sigma}}^2_{xx}}{\partial g_{ij}} \right] \\ &= \frac{1}{2} \operatorname{Tr} \left[\frac{\partial \mathbf{W}(\mathbf{G})}{\partial g_{ij}} \, \overline{\boldsymbol{\sigma}}^2_{xx} \; + \; \frac{\partial \overline{\boldsymbol{\sigma}}^2_{xx}}{\partial g_{ij}} \, (\boldsymbol{\Lambda} - (\mathbf{A}_c^d)^T \boldsymbol{\Lambda} \mathbf{A}_c^d) \right] \\ &= \frac{1}{2} \operatorname{Tr} \left[\frac{\partial \mathbf{W}(\mathbf{G})}{\partial g_{ij}} \, \overline{\boldsymbol{\sigma}}^2_{xx} \; + \; \boldsymbol{\Lambda} \, (\frac{\partial \overline{\boldsymbol{\sigma}}^2_{xx}}{\partial g_{ij}} - \mathbf{A}_c^d \frac{\partial \overline{\boldsymbol{\sigma}}^2_{xx}}{\partial g_{ij}} (\mathbf{A}_c^d)^T) \right] \end{aligned} \tag{4.73}$$

After differentiating the Lyapunov equation in $\overline{\boldsymbol{\sigma}}^2_{xx}$

$$\mathbf{A}_c^d \frac{\partial \overline{\boldsymbol{\sigma}}^2_{xx}}{\partial g_{ij}} (\mathbf{A}_c^d)^T - \frac{\partial \overline{\boldsymbol{\sigma}}^2_{xx}}{\partial g_{ij}} + \frac{\partial \mathbf{A}_c^d}{\partial g_{ij}} \overline{\boldsymbol{\sigma}}^2_{xx} (\mathbf{A}_c^d)^T + \mathbf{A}_c^d \overline{\boldsymbol{\sigma}}^2_{xx} \left(\frac{\partial \mathbf{A}_c^d}{\partial g_{ij}} \right)^T + \frac{\partial \mathbf{W}_3(\mathbf{G})}{\partial g_{ij}} = \mathbf{0} \tag{4.74}$$

the following expression is obtained

$$\begin{aligned} \frac{\partial J}{\partial g_{ij}} = \frac{1}{2} \operatorname{Tr} \Bigg[\frac{\partial \mathbf{W}(\mathbf{G})}{\partial g_{ij}} \, \overline{\boldsymbol{\sigma}}^2_{xx} \; + \; \boldsymbol{\Lambda} \, \Bigg(\frac{\partial \mathbf{A}_c^d}{\partial g_{ij}} \overline{\boldsymbol{\sigma}}^2_{xx} (\mathbf{A}_c^d)^T + \ldots \\ \ldots + \mathbf{A}_c^d \overline{\boldsymbol{\sigma}}^2_{xx} \left(\frac{\partial \mathbf{A}_c^d}{\partial g_{ij}} \right)^T + \frac{\partial \mathbf{W}_3(\mathbf{G})}{\partial g_{ij}} \Bigg) \Bigg] \end{aligned} \tag{4.75}$$

A compact form of the gradient can be expressed as follows

$$\frac{\partial J}{\partial g_{ij}} = \frac{1}{2} \operatorname{Tr} \left[\mathbf{M}_1 \frac{\partial \mathbf{G}}{\partial g_{ij}} \right] \tag{4.76}$$

where

$$\mathbf{M}_1 = 2\left[\mathbf{C}\,\overline{\boldsymbol{\sigma}}_{xx}^2\left(\mathbf{C}^T\mathbf{G}^T\mathbf{W}_{vv} - (\mathbf{A}_c^d)^T\boldsymbol{\Lambda}\mathbf{B}\right) - \mathbf{D}_n\mathbf{W}_{nn}(\mathbf{B}_n - \mathbf{B}\mathbf{G}\mathbf{D}_n)^T\boldsymbol{\Lambda}\mathbf{B}\right] \tag{4.77}$$

4.3.3 Design with time delay

The discrete-time design presented in the previous section can be improved by including a time delay information representing the elapsed time between the instant at which the sensor signal is measured and the instant at which the control voltage is applied. This delay naturally occurs in all digital implementations. Indeed, it is due to the acquisition time of the analog-to-digital converter, the time needed to perform all the computations related to the control law and the time of the digital-to-analog conversion. The presence of a delay may introduce closed-loop instability if it is large and not properly considered in the design process.

In the technical solution of the problem at hand a delay of 100µs has been estimated. If the maximum working frequency is 2kHz, the minimum sampling period results 500µs, so in our case. A modified model should thus be able to represent a delay shorter than or equal to the sampling period, at most.

From literature [38], it is possible to extract the procedure to reformulate the system dynamics including a time delay

$$\dot{\mathbf{x}}(t) = \mathbf{A}\mathbf{x}(t) + \mathbf{B}\mathbf{v}(t - t_d) + \mathbf{B}_{dn}\mathbf{d}(t) \tag{4.78}$$

Here t_d is the time delay and could be expressed as a fraction of the sampling period Δt as follows

$$t_d = (1 - m)\Delta t\,, \qquad 0 \leqslant m \leqslant 1 \tag{4.79}$$

By calling $\eta = (k+1)\Delta t - \tau$, for $m \neq 1$, the discrete solution between two consecutive intervals can be found with

$$\mathbf{x}_{k+1} = A^d\mathbf{x}_k \,+\, \mathbf{B}^{d2}\mathbf{u}_k \,+\, \mathbf{B}^{d1}\mathbf{u}_{k-1} \,+\, \mathbf{B}_{dn}^d\mathbf{d}_k \tag{4.80}$$

where

$$\begin{aligned}
\mathbf{A}^d &= e^{\mathbf{A}\Delta t} \\
\mathbf{B}^{d1} &= \int_{m\Delta t}^{\Delta t} e^{\mathbf{A}\eta}\mathbf{B}\,d\eta \\
\mathbf{B}^{d2} &= \int_{0}^{m\Delta t} e^{\mathbf{A}\eta}\mathbf{B}\,d\eta \\
\mathbf{B}_{dn}^d &= \int_{0}^{\Delta t} e^{\mathbf{A}\eta}d\eta\mathbf{B}_{dn}
\end{aligned}$$

The integrals of $\mathbf{B}^{d1}$ and $\mathbf{B}^{d2}$ can be computed and expressed in terms of known matrices

$$\begin{aligned}\mathbf{B}^{d1} &= \mathbf{A}^{-1}\left[\mathbf{A}^{d} - \mathbf{A}^{dm}\right]\mathbf{B} \\ \mathbf{B}^{d2} &= \mathbf{A}^{-1}\left[\mathbf{A}^{dm} - \mathbf{I}\right]\mathbf{B}\end{aligned} \tag{4.81}$$

with

$$\mathbf{A}^{dm} = e^{\mathbf{A}m\Delta t}$$

At this point the only critical aspect is dealing with discrete time dynamic equations that are no more first order. To insert the result in the developed discrete-time design, it is necessary to reduce the equations to first order. This is possible by augmenting the state as follows

$$\begin{Bmatrix}\mathbf{x}_{k+1} \\ \tilde{\mathbf{u}}_{k+1}\end{Bmatrix} = \begin{bmatrix}\mathbf{A}^{d} & \mathbf{B}^{d1} \\ \mathbf{0} & \mathbf{0}\end{bmatrix}\begin{Bmatrix}\mathbf{x}_{k} \\ \tilde{\mathbf{u}}_{k}\end{Bmatrix} + \begin{bmatrix}\mathbf{B}^{d2} \\ \mathbf{I}\end{bmatrix}\left\{\mathbf{u}_{k}\right\} + \begin{bmatrix}\mathbf{B}_{d}^{d} & \mathbf{B}_{n}^{d} \\ \mathbf{0} & \mathbf{0}\end{bmatrix}\begin{Bmatrix}\mathbf{d}_{k} \\ \mathbf{n}_{k}\end{Bmatrix} \tag{4.82}$$

It should be adapted to the augmented system also the output and performance equations

$$\mathbf{y}_{k} = \begin{bmatrix}\mathbf{C} & \mathbf{0}\end{bmatrix}\begin{Bmatrix}\mathbf{x}_{k} \\ \tilde{\mathbf{u}}_{k}\end{Bmatrix} + \mathbf{D}_{n}^{d}\,\mathbf{n}_{k} \tag{4.83}$$

$$\mathbf{z}_{k} = \begin{bmatrix}\mathbf{C}_{z} & \mathbf{0}\end{bmatrix}\begin{Bmatrix}\mathbf{x}_{k} \\ \tilde{\mathbf{u}}_{k}\end{Bmatrix} \tag{4.84}$$

The limit cases of this system are the absence of delay, $m = 1$, that corresponds to $\mathbf{B}^{d1} = \mathbf{0}$ and $\mathbf{B}^{d2} = \mathbf{B}^{d}$, and the $t_d = \Delta t$ case, that presents $\mathbf{B}^{d1} = \mathbf{B}^{d}$ and $\mathbf{B}^{d2} = \mathbf{0}$

It should be highlighted that the introduction of a time delay does not modify the steps to be carried out for the design of the discrete-time controller, but it changes the system conversion procedure from continuous to discrete. The great difference, apart from the weighting matrices definitions adapted to the augmented state, lie in the increased size of the state that augments by a number of variables equal to the control points.

4.4 Preliminary assessment

With the aim of having a preliminary assessment of the above design procedures on a simple problem, a mechanical model made of a chain of n_m masses connected by linear springs and viscous dampers was built. Despite its simplicity, the model resembles the main dynamic properties of a vibrating structural system like the mirror shell under investigation.

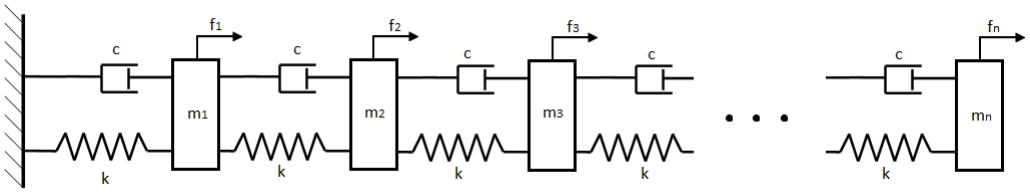

Figure 4.1: Preliminary Assessment: mass-spring-damper system

n_m	6
m	10 kg
k	30 N/m
c	0.2 Ns/m

Table 4.1: System parameters

4.4.1 Problem and design settings

The system data are reported in table 4.1. Masses, springs and dampers are all equal and spatially disposed as shown in figure 4.1. The equation describing the system dynamics assumes the simple form

$$\mathbf{M}\,\ddot{\mathbf{s}} + \mathbf{C}\,\dot{\mathbf{s}} + \mathbf{K}\,\mathbf{s} = \mathbf{f} \tag{4.85}$$

The corresponding state space formulation is

$$\begin{Bmatrix} \dot{\mathbf{s}} \\ \ddot{\mathbf{s}} \end{Bmatrix} = \begin{bmatrix} \mathbf{0} & \mathbf{I} \\ -\mathbf{M}^{-1}\mathbf{K} & -\mathbf{M}^{-1}\mathbf{C} \end{bmatrix} \begin{Bmatrix} \mathbf{s} \\ \dot{\mathbf{s}} \end{Bmatrix} + \begin{bmatrix} \mathbf{0} \\ \mathbf{M}^{-1} \end{bmatrix} \mathbf{f} = \mathbf{A}\mathbf{x} + \mathbf{B}\mathbf{f} \tag{4.86}$$

The output vector includes both position and velocity of the masses, in order to simulate both position measure and its derivative. In this trivial problem, filters on the sensor channels have not been included. Thus, the output equation takes the simple form

$$\begin{Bmatrix} \mathbf{y}_s \\ \mathbf{y}_{\dot{s}} \end{Bmatrix} = \begin{bmatrix} \mathbf{I} & \mathbf{0} \\ \mathbf{0} & \mathbf{I} \end{bmatrix} \begin{Bmatrix} \mathbf{s} \\ \dot{\mathbf{s}} \end{Bmatrix} + \begin{bmatrix} \mathbf{0} \\ \mathbf{0} \end{bmatrix} \mathbf{f} = \mathbf{C}\mathbf{x} + \mathbf{D}\mathbf{f} \tag{4.87}$$

The performance accounts for both $\mathbf{s}$ and $\dot{\mathbf{s}}$. In this way, it is possible to design a control law aimed at both correct positioning and active damping. Accordingly, the performance equation is expressed as

$$\mathbf{z} = \begin{bmatrix} \mathbf{I} & \mathbf{0} \\ \mathbf{0} & \mathbf{I} \end{bmatrix} \begin{Bmatrix} \mathbf{s} \\ \dot{\mathbf{s}} \end{Bmatrix} = \mathbf{C}_z\mathbf{x} \tag{4.88}$$

The weighting matrices are set as follows

$$\mathbf{W}_{zz} = \begin{bmatrix} \rho_s \mathbf{I} & \mathbf{0} \\ \mathbf{0} & \rho_{\dot{s}} \mathbf{I} \end{bmatrix} \tag{4.89}$$

$$\mathbf{W}_{ff} = \rho_f \mathbf{I} \tag{4.90}$$

thus involving three weights, ρ_s, $\rho_{\dot{s}}$ and ρ_f. The control design, and so the closed-loop response of the system, can be largely affected by the values of these weights, and in particular by their relative magnitude. Since in this preliminary assessment we are not interested in the achievable performance of the controller but the aim is only to validate the procedure, the three weights were arbitrarily set as follows

$$\rho_s = 1\,, \qquad \rho_{\dot{s}} = 100\rho_s\,, \qquad \rho_f = 0.006\rho_s \tag{4.91}$$

4.4.2 Optimal and suboptimal control

A first check was carried out to study the convergence of the suboptimal control solution to the solution obtained using a full state feedback optimal control. It can be actually verified that, if the output matrix $\mathbf{C}$ is an identity matrix having the same dimensions as the state matrix, the whole state enters the feedback line, making the control law assuming the same form of the full state feedback:

$$\mathbf{f} = -\mathbf{G}\mathbf{y} = -\mathbf{G}\mathbf{C}\mathbf{x} = -\mathbf{G}\mathbf{I}\mathbf{x} = -\mathbf{G}\mathbf{x} \tag{4.92}$$

The results obtained with the numerical optimization of the suboptimal cost function have thus been compared with the results of a Linear Quadratic Regulator (LQR).

The starting point for the suboptimal optimization problem was a disturbed version of the optimal solution. The gain matrices resulting from the two design procedures are reported as histograms in figures 4.2 and 4.3. Each element is represented by a column with height proportional to its value, positioned in the xy plane in correspondence of its location inside the matrix.

The matrices could be both split into two square blocks. The first block, corresponding to the first six columns, contains the proportionality factors of the position measures, while the second block contains the gains corresponding to the feedback of the velocity variables. At first sight, the closed similarity between the two results is evident. This similarity is also shown by plotting the relative error matrix, as reported in figure 4.4. It should be specified that errors related to gain elements lower than 5 have been omitted. This is due to the fact that most of those gains were really closed to 0

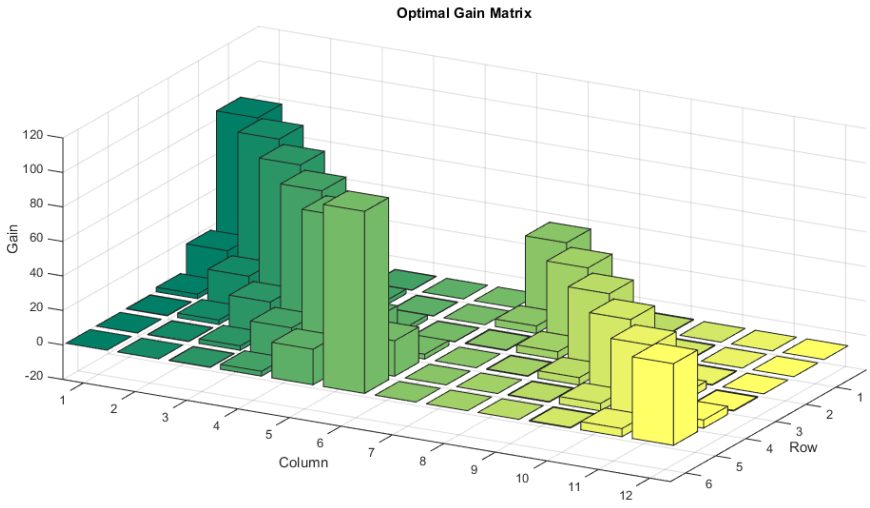

Figure 4.2: Preliminary Assessment: optimal gain matrix

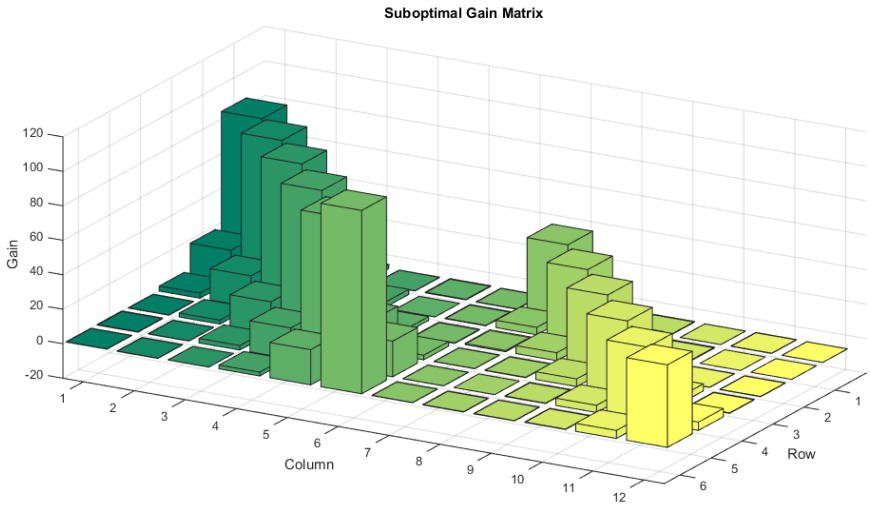

Figure 4.3: Preliminary Assessment: suboptimal gain matrix

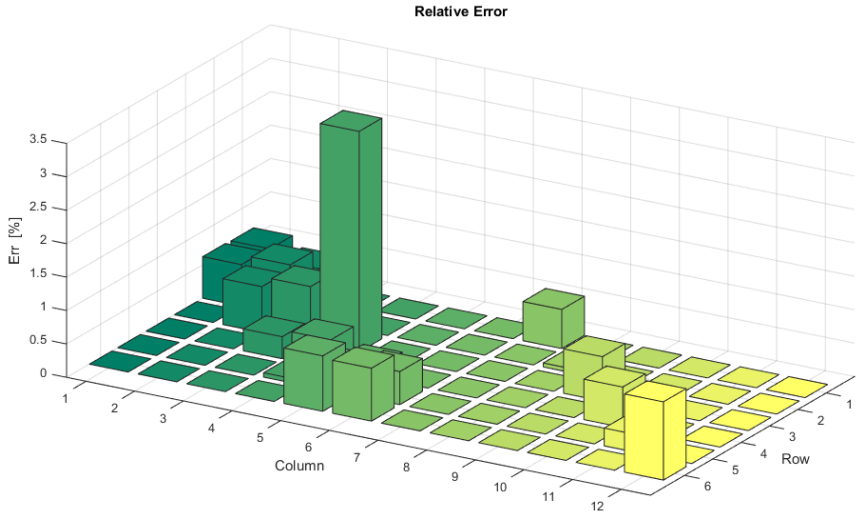

Figure 4.4: Preliminary Assessment: relative error matrix

and thus even a small discrepancy yields huge relative errors, without substantial meaning. It could be also noted that the greatest errors belong to the smallest gains. Another interesting aspect to be noticed is the strong diagonal dominance of the gain matrix. This characteristic suggests that a fully decentralized approach could produce in this case similar performances as the centralized controller.

4.4.3 Constraints on the structure of the gain matrix

To test the capability of the design procedure to introduce some constraints on the structure of the gain matrix, a decentralized suboptimal PD control has been imposed first. Then, the same controller has been designed with the additional constraint of using the same proportional and derivative gain for all the actuators.

It can be seen in figure 4.5 that the centralized optimal solution and the PD decentralized solution give nearly identical closed-loop responses. Also the minimum values of the cost function are very similar. The optimal value is $J_{opt} = 4064,69$, whereas the suboptimal solution yields $J_{PD} = 4067,60$.

When the same P and D gains are imposed for all control channels, the difference between the two responses slightly increases, although it is still difficult to note a substantial loss of performance with respect to the previous cases. As expected, the minimum value of the cost function rises up to $J_{ePD} = 4123,61$, due to the additional constraint on the optimization procedure.

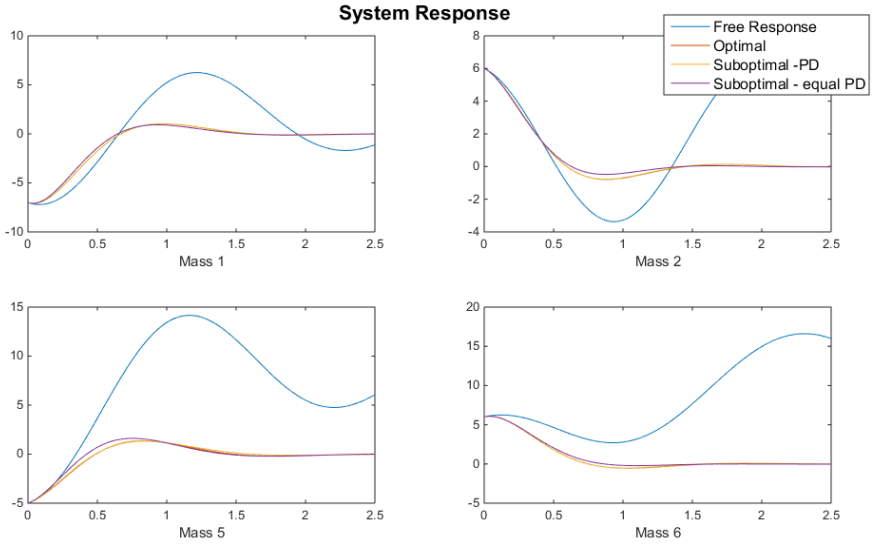

Figure 4.5: Constrained Solutions - system response

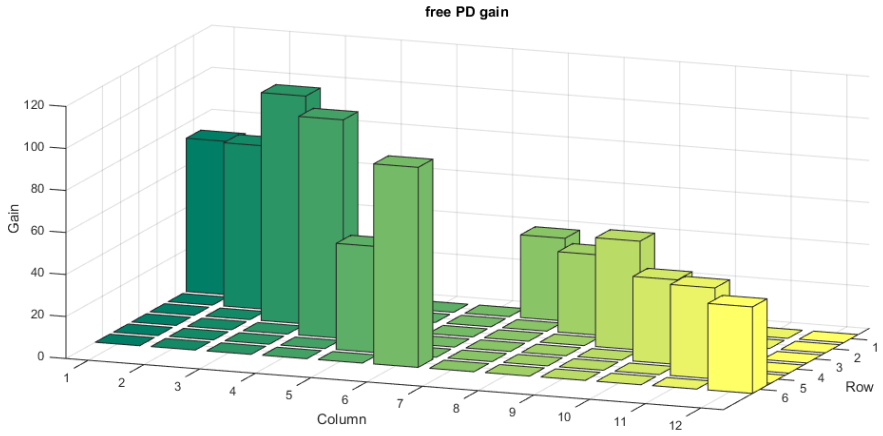

Figure 4.6: Free PD gain matrix

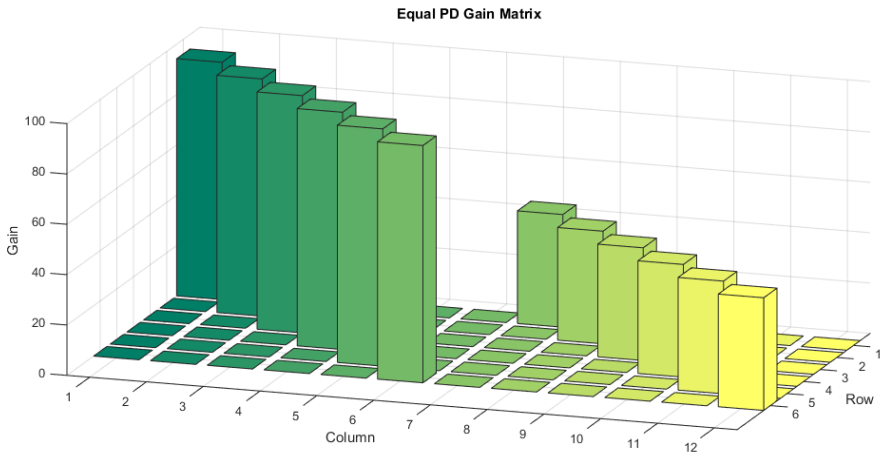

Figure 4.7: Equal PD gain matrix

4.4.4 Continuous and discrete-time controllers

A final check has been done to validate the discrete-time formulation. As the sampling frequency increases, the gains from the discrete-time design are expected to converge to the gains of the continuous-time design. To observe this phenomenon, different optimization processes have been run, for a fixed PD controller, with increasing control frequency. Results are reported in figure 4.8. Moving towards lower frequencies, reduction in the gains values clearly emerges to avoid unstable behaviors. Figure 4.9 also shows a comparison between a continuous and a 5Hz discrete implementation of the PD control, respectively adopting as control gains couples $[\,94,24\,;\,44,75\,]$ and $[\,45,97\,;\,35,18\,]$.

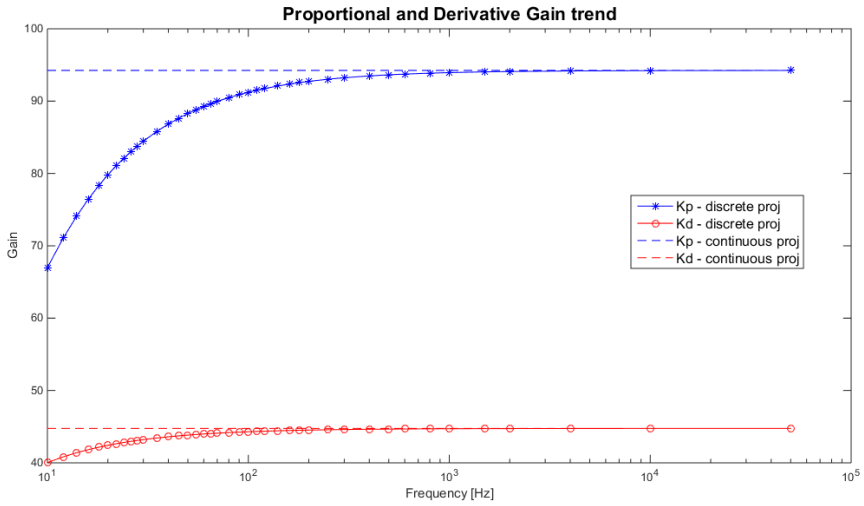

Figure 4.8: Discrete Time Project - PD gains trend with frequency

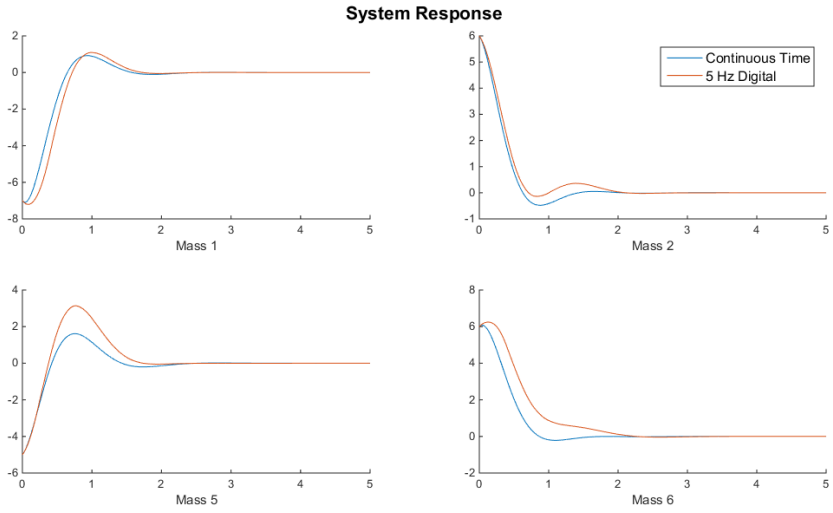

Figure 4.9: Continuous vs Discrete Time Project Response

Chapter 5

Control Synthesis and Implementation

In this chapter, the combined feedforward-feedback control system previously described is applied to the P45 secondary mirror model. First, an ideal continuous-time design is carried out. The related closed-loop simulations can provide a reference benchmark achievable performance of the proposed approach. Then, three possible different implementations of the above reference design are discussed, along with their advantages and limitations. Finally, through extensive simulations, an off-design performance analysis limited to key modeling parameters is presented, in order to study the sensitivity of the nominal design to realization or integration errors and to simulate off-design operational conditions.

5.1 Simulations Settings

The synthesized control laws and the related hardware architectures described in this chapter have been tested with simulations under space representative conditions.

The dynamic model that simulate the mirror structural response (see Eq. 2.27) includes 100 modes, that is the entire set of available modes, in order to observe any possible excitation of the highest frequencies modal components.

External and internal disturbances have been added, to test the control system rejection capability. The force disturbance vector $\mathbf{f}_d$ is composed of a quasi-static component representing relevant environmental disturbances, since typical telescopes operational conditions produce constant or very low frequency effects. Large and flexible structures may be subjected to thermal loads, gravity gradient or inertial loads. These aspects have been investigated

arriving to the conclusion that thermal loads constitute the most relevant source of errors. The gravitational gradient, even for very large optics, and the inertial loads of slow attitude maneuvers produce indeed effects several order of magnitude lower than temperature gradients. Thus, missing a real satellite integrated model, plausible temperatures profiles have been used to deduce equivalent force loads to be counteracted by the mirror shape control system when compensating the thermo-elastic structural response of the shell. Data have been retrieved from JWST thermal simulations [39] and the maximum temperature variations have been used to modulate linear and harmonically varying temperature profiles.

The measure noise $\mathbf{n}$ has been instead tuned according to previous experiences with similar hardware [8]. Thus Gaussian noise has been assumed, with standard deviation $\sigma_n = 3 \times 10^{-9}$m.

The system comprises a suitable on-board processor unit, which is equipped with proper analog-to-digital and digital-to-analog converters as physical interfaces to the capacitive sensors and the voltage-driven voice-coil actuators. Both AD and DA converters are assumed to have 16 bits. The AD reading process must cover a range of 1mm, which is the maximum distance between the mirror and the backplate. The DA operation covers a range of $\pm 2,5$V, which is the maximum voltage applied to the voice-coils. With a 16 bit AD converter, the 1mm range corresponds to a resolution of about 15nm. This clearly represents a severe limitation if the position error of the mirror must lie within 10nm with respect to the reference.

In addition, voltage noise has been added on the actuator's circuit, according to the characteristics of the adopted hardware. In particular, being the voltage noise intensity at most equal to the quantum amplitude, this disturbance has been introduced in the full digital implementation case simply by neglecting one bit availability, while in the other cases by setting the $3\sigma_v$ value equal to the bit amplitude.

The maximum sampling frequency simulated has been 2kHz, which is a reasonable value according to the limited capabilities of space on-board hardware and to the related need for low power consumption.

5.2 Design settings

In what follows, the feedback gain matrix has been designed using the stochastic approach. This methodology showed more sensibility and flexibility with respect to the deterministic version. This is probably due to a better capability of the white-noise disturbances to excite the system.

Concerning the definition of the performance, as previously proposed in

the preliminary assessment, both position and velocity have been included to obtain a minimization of the positioning error while adding active damping. Thus, to insert those quantities in the performance vector $\mathbf{z}$, evaluated at the actuators positions, it is possible to recall Eq. (2.6) and write

$$\mathbf{z} = \begin{Bmatrix} \mathbf{u} \\ \dot{\mathbf{u}} \end{Bmatrix} = \begin{bmatrix} \mathbf{\Phi} & \mathbf{0} & \mathbf{0} & \mathbf{0} & \mathbf{0} & \mathbf{0} \\ \mathbf{0} & \mathbf{\Phi} & \mathbf{0} & \mathbf{0} & \mathbf{0} & \mathbf{0} \end{bmatrix} \begin{Bmatrix} \mathbf{q} \\ \dot{\mathbf{q}} \\ \mathbf{i} \\ \mathbf{u}_m \\ \mathbf{z} \\ \mathbf{J} \end{Bmatrix} = \mathbf{C}_z \mathbf{x} \tag{5.1}$$

The weighting matrices related to performance and control effort have been defined with embedded tunable parameters to have a direct control of the relative weight of the different elements. As it is hard to anticipate the importance of an actuation point with respect to any other point or to introduce specific limitations for some actuators, only three weights have been used, one for each group of velocities, positions and control voltages. The result is a performance weighting matrix defined as

$$\mathbf{W}_{zz} = \begin{bmatrix} \rho_u \mathbf{I} & \mathbf{0} \\ \mathbf{0} & \rho_{\dot{u}} \mathbf{I} \end{bmatrix} \tag{5.2}$$

and a control effort weighting defined as

$$\mathbf{W}_{vv} = \begin{bmatrix} \rho_v \mathbf{I} \end{bmatrix} \tag{5.3}$$

After a detailed preliminary analysis, the values of the three free parameters have been set to

$$\rho_u = 2.5 \times 10^9 \qquad \rho_{\dot{u}} = 1.0 \qquad \rho_v = 1.0$$

Another crucial design setting is the value of the weighted intensity of the white noise process representing the measurement noise $\mathbf{n}$ and the disturbance $\mathbf{f}_d$. They have been tuned separately, according to their different nature. Referring to Eq. (4.28), noise intensities have been defined as

$$\begin{aligned} \mathbf{W}_{dd} &= w_d \mathbf{I} \\ \mathbf{W}_{nn} &= w_n \mathbf{I} \end{aligned} \tag{5.4}$$

with

$$w_d = 1.0 \qquad w_n = 2.0 \times 10^{-14}$$

The above five parameters (ρ_u, $\rho_{\dot{u}}$, ρ_v, w_d, w_n) can be used to finely tune the design and, as a result, to obtain the desired closed-loop response. Their final value is the outcome of an iterative process which is aimed at achieving a satisfactory tradeoff among closed-loop performance and practical feasibility.

Beyond these settings, that directly influence the cost function and so the gain matrix, other specifications have to be set in order to obtain relevant results from the design process.

A first setting is related to the number of structural modes considered in the control design model of the mirror. A large number of modes would definitely increase the reliability of the model, reducing also the vulnerability to spillover effects. However, a large model would rise significantly the computational cost of the optimization procedure. This issue is rather limited for the P45 prototype, since it presents few natural frequencies falling in the low-frequency range, but it would require more attention for larger flexible mirrors with lower natural frequencies. In addition, larger order design models are computationally demanding when the optimization procedure has to be iterated many times or the searching for the minimum value of the cost function requires many steps to achieve the prescribed tolerance threshold. In such cases, the overall numerical optimization could even take many minutes, if not hours. In the present design, a total number of 17 modes has been considered. This choice guarantees a reduced size of the state-space matrices along with a model which is well representative of the dynamics of the system in the frequency range of interest. Indeed, the 17^{th} structural mode of the mirror has an undamped natural frequency of about 1100Hz. The reduced-order modal model can thus be considered reliable and the corresponding control design is believed to provide reliable results. Later, design solutions involving more modal shapes[1] has been verified. These anyway presented the same gains as results, proving the reliability of the chosen modal set.

The bandwidth of the filters on the sensor measurement is another design parameter. As already mentioned in section 2.1.3, the cutoff frequency of the filters can be set to properly limit the frequency content of the feedback signal and thus prevent high-frequency instabilities. However, a sufficiently large bandwidth has to be enforced to avoid an excessive limitation of the control capability. The selection of filters bandwidth involves the setting of the values a and b. In this work, they have been set to 400Hz, also to prevent aliasing effects at 1kHz control frequency.

Finally, a fully decentralized feedback PD control architecture was selected for the realization simplicity of such solution, as already discussed in

[1]Design solutions with 50 modes and with the entire available modal set has been investigated.

the previous chapters. According to the organization of the control design software, the user can easily select different and more complex architectures to be investigated, which could lead to more advanced closed-loop performance due to the distributed fully coupled dynamic nature of the problem.

Numerical Issues

Compared to the simple problem introduced in the previous chapter for the preliminary assessment of the feedback suboptimal control, the voltage-driven voice-coil actuated deformable mirror presents some differences. First of all, the two systems are characterized by natural damping factors which differ of several orders of magnitude. This fact, beyond generating very different decays of the dynamic response, raises severe numerical issues in the optimization algorithms, in particular it largely affects the convergence rate. Strictly speaking, this issue is related to the choice of the initial guess matrix $\mathbf{G}$, which must be a stabilizing gain matrix. The stability region of the space spanned by the elements of $\mathbf{G}$ considerably shrinks when damping significantly decreases. Consequently, in case of very small damping factors, it is extremely hard to find a stabilizing initial guess for the control gains and force the optimization method to move within the closed-loop stability region. Thus, it has been necessary to perform a series of continued optimization runs, starting from a virtually highly damped system and decreasing step by step the structural damping each time until reaching its estimated small value. Since in highly damped systems the structural poles lie sufficiently far from the imaginary axis, the method easily prevents the iterative solution from moving towards unstable regions. At each new run, the set of gains resulting from the previous run associated with an higher level of damping is taken as the initial guess for a system with decreased damping. In so doing, a satisfactory convergence of the optimization method to an initial stable guess is obtained.

5.3 Continuous-time design and simulations

Before dealing with practical implementations of the control law, a preliminary continuous-time simulation of the controlled dynamics of the P45 mirror has been carried out. As already mentioned, this analysis provides a theoretical reference of the achievable closed-loop performance. According to this framework, the system dynamics includes neither quantized variables nor discrete-time signals.

Based on the weighting matrices selected as discussed in the previous

K_P	$5528,6$
K_D	$9,1$

Table 5.1: Continuous Time control Project

section, the design of the PD static output optimal feedback controller using a continuous-time stochastic procedure resulted in the relatively high control gains reported in table 5.1. As widely described throughout all this thesis, the combined feedback-feedforward controller has the following form

$$\mathbf{V}_c(t) = \mathbf{V}_{c\,ff}(t) + \mathbf{V}_{c\,fb}(t) \tag{5.5}$$

where $\mathbf{V}_{c\,ff}(t)$ is the hybrid feedforward formulation of section 3.1.3

$$\begin{aligned} \mathbf{V}_{c\,ff}(t) = \mathbf{V}_{c\,ff,k} + \{\, [\urcorner\alpha\llcorner]\overline{\mathbf{V}}_{c,k} + (\mathbf{I} - [\urcorner\alpha\llcorner])\mathbf{V}_{c\,ff,k} - \mathbf{V}_{c\,ff,k} \,+ ... \\ ... + \mathbf{K}_v^*\,\mathbf{u}_{k+1}^r \,- (\,[\urcorner\alpha\llcorner]\,\overline{\mathbf{y}}_{u,k} + (\,\mathbf{I} - [\urcorner\alpha\llcorner]\,)\,\mathbf{u}_k^r\,)\,\}\,f_{sh}(t) \,+ ... \\ ... + \,[\,\mathbf{C}_v^*\,\dot{f}_{sh}(t) + \mathbf{M}_v^*\,\ddot{f}_{sh}(t)\,]\,(\mathbf{u}_{k+1}^r - \mathbf{u}_k^r) \end{aligned} \tag{5.6}$$

and $\mathbf{V}_{c\,fb}(t)$ is instead the feedback law in the form

$$\mathbf{V}_{c\,fb}(t) = -\mathbf{G}(\mathbf{y} - \mathbf{y}^r) = -\mathbf{G}\begin{Bmatrix}\mathbf{y}_u \\ \mathbf{y}_v\end{Bmatrix} + \mathbf{G}\begin{Bmatrix}\mathbf{u}_k^r + (\mathbf{u}_{k+1}^r - \mathbf{u}_k^r)f_{sh}(t) \\ \mathbf{0}\end{Bmatrix} \tag{5.7}$$

The closed-loop response of the system is governed by the following dynamics

$$\begin{aligned} \dot{\mathbf{x}}(t) = (\mathbf{A} - \mathbf{BGC})\,\mathbf{x}(t) \,+\, \mathbf{B}\,(\,\mathbf{V}_{c\,ff}(t) + \mathbf{G}\mathbf{y}^r(t)\,) \,+ ... \\ ... + \,[\,\mathbf{B}_d \quad (\mathbf{B}_n - \mathbf{BGD}_n)\,]\begin{Bmatrix}\mathbf{f}_d(t) \\ \mathbf{n}(t)\end{Bmatrix} \end{aligned} \tag{5.8}$$

A sample response is reported in figures 5.1, 5.2 and 5.3, where both the real and the measured position are plotted. One can clearly observe the net improvement of the closed-loop response with respect to the already good pure Oxymoronic feedforward response (fig.3.7). The response is fully bounded within the 10nm limits.

A general idea of the global closed-loop performance over the whole mirror surface can be gathered by analyzing the position error. The maximum error is reported in figure 5.5 at each time step. It clearly shows the strong capability of the control system to stabilize the shell, with an accurate tracking of the reference positioning even during the transients between two consecutive step variations. A quantitative measure of the positioning quality over the whole surface is given by the time history of the RMS error, which is showed in figure 5.6. Another quantity which measures the performance of

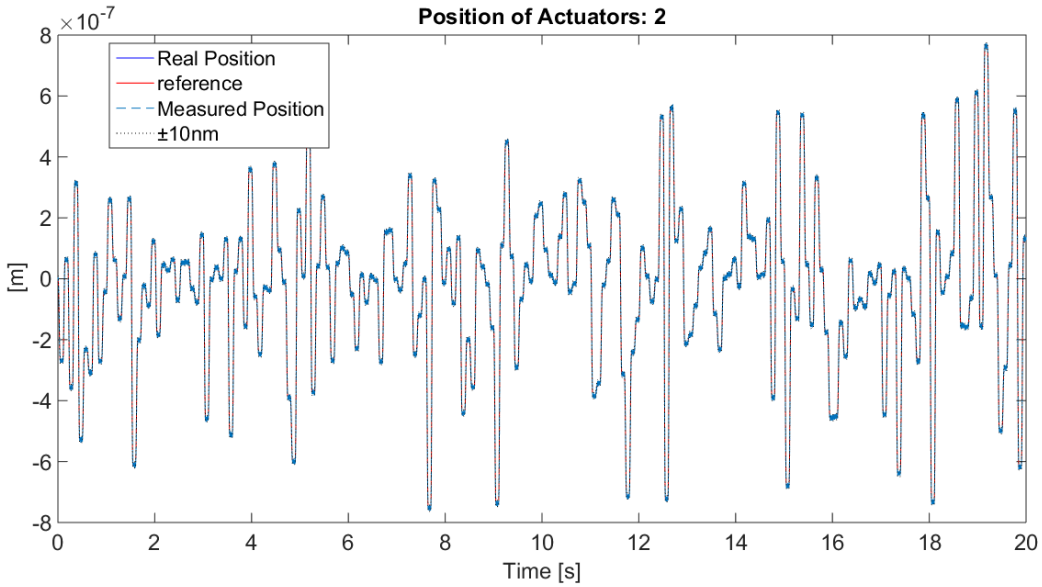

Figure 5.1: Ideal System - response

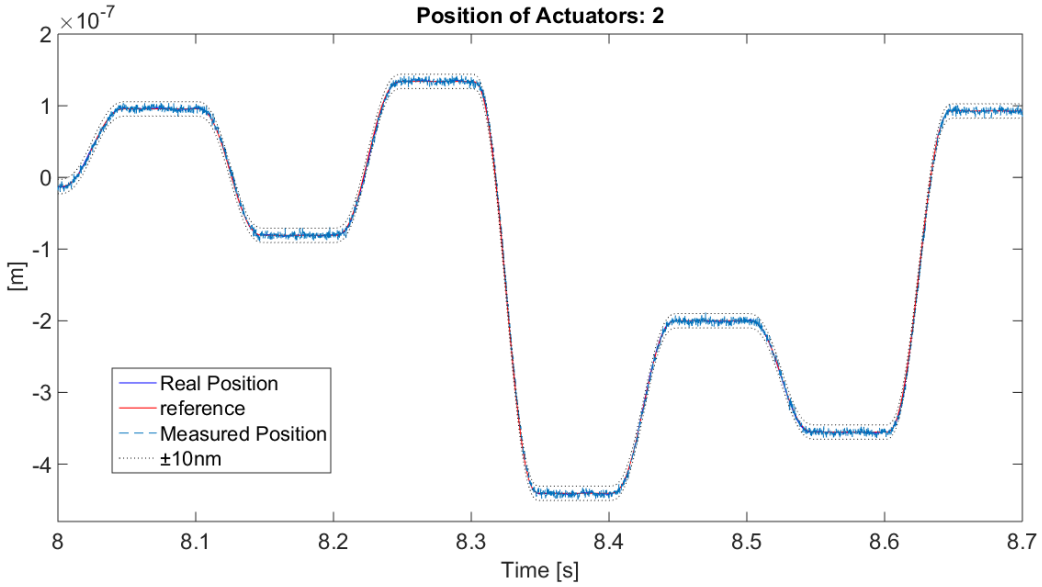

Figure 5.2: Ideal System - response detail

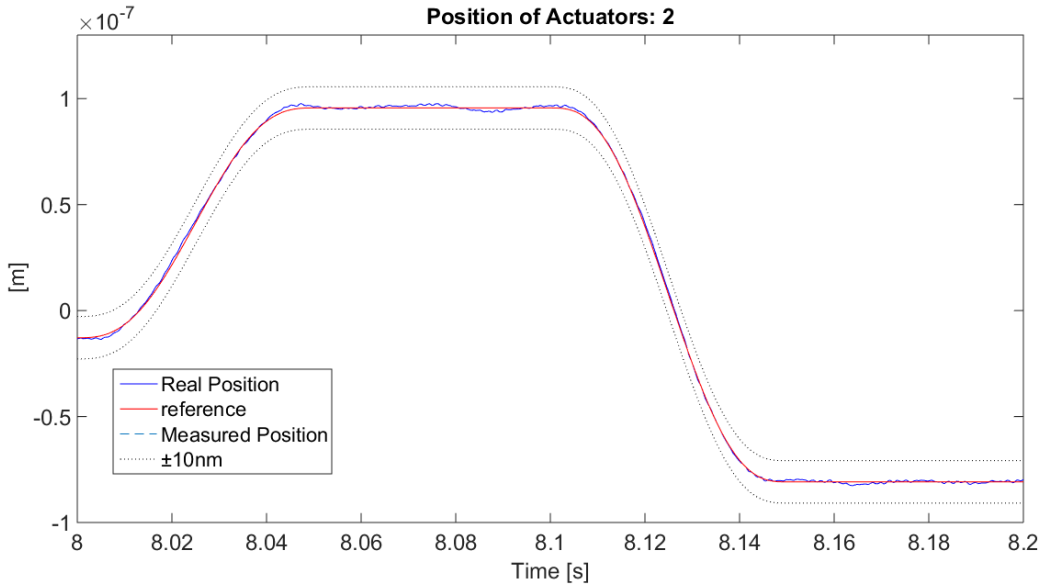

Figure 5.3: Ideal System - response detail

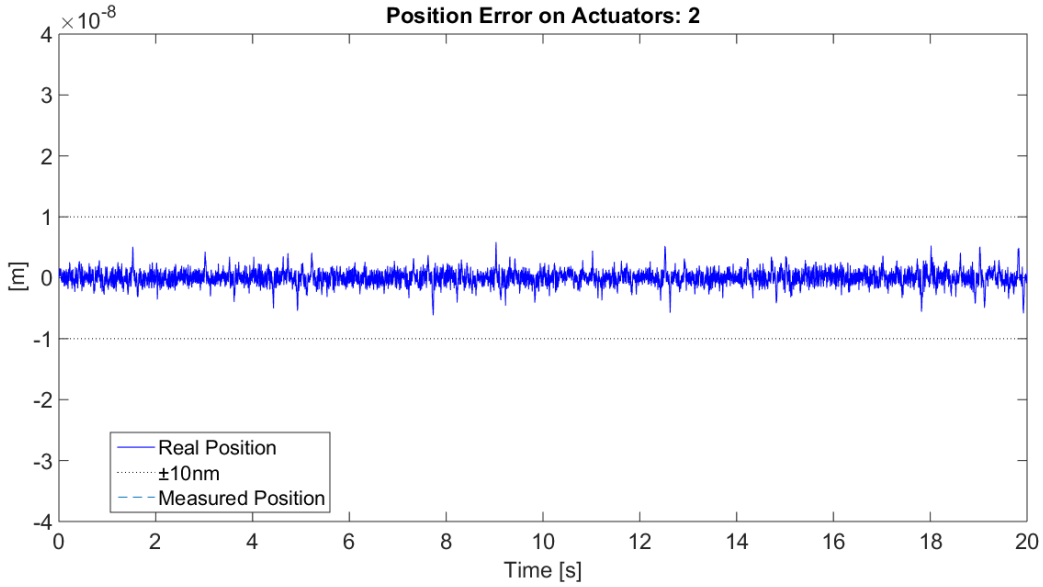

Figure 5.4: Ideal System - error

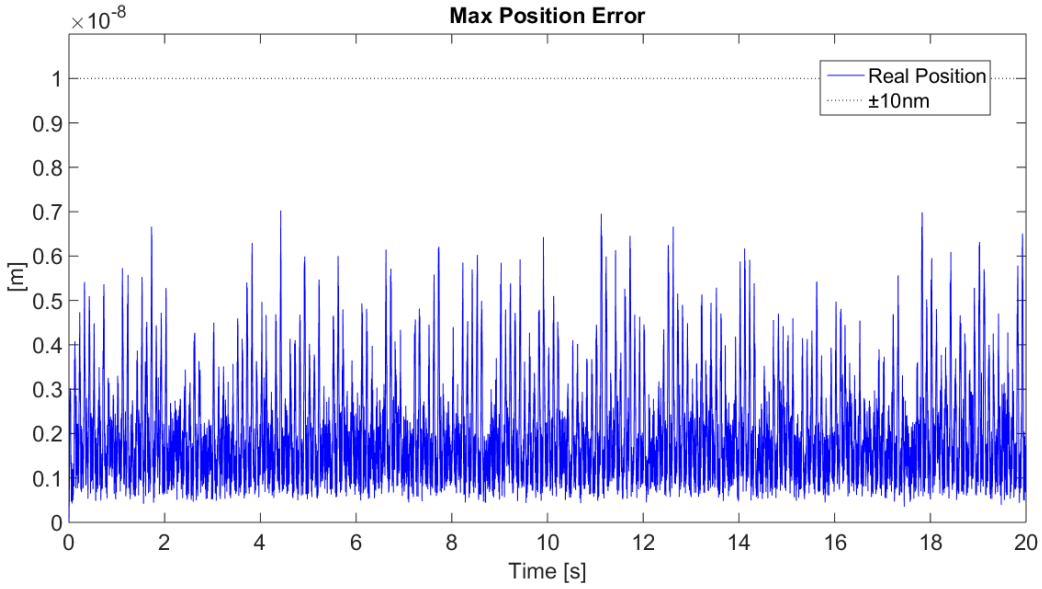

Figure 5.5: Ideal System - maximum error over the surface

the present control system is the RMS error computed in the time interval corresponding to the steady state part of the commands. This quantity, reported in figure 5.7, results to be around 1nm, that is far below the required level.

Finally, an analysis on the voltages required by the control system was performed to check possible saturation. This is shown in figure 5.8, where it can be seen that the saturation value of $\pm 2,5$V is never exceeded.

5.4 Three different control implementations

In this section, three different practical implementations of the combined feedback-feedforward controller of the P45 mirror are studied. The first approach realizes the control system almost entirely with analog components to reproduce the ideal case behavior in the most accurate way. The other two solutions, noticing the impossibility to avoid a digital interface with the rest of the corrective control chain, partially or fully discard the analog components, assigning their tasks to the on-board computer, in search for a tradeoff between system complexity and performances.

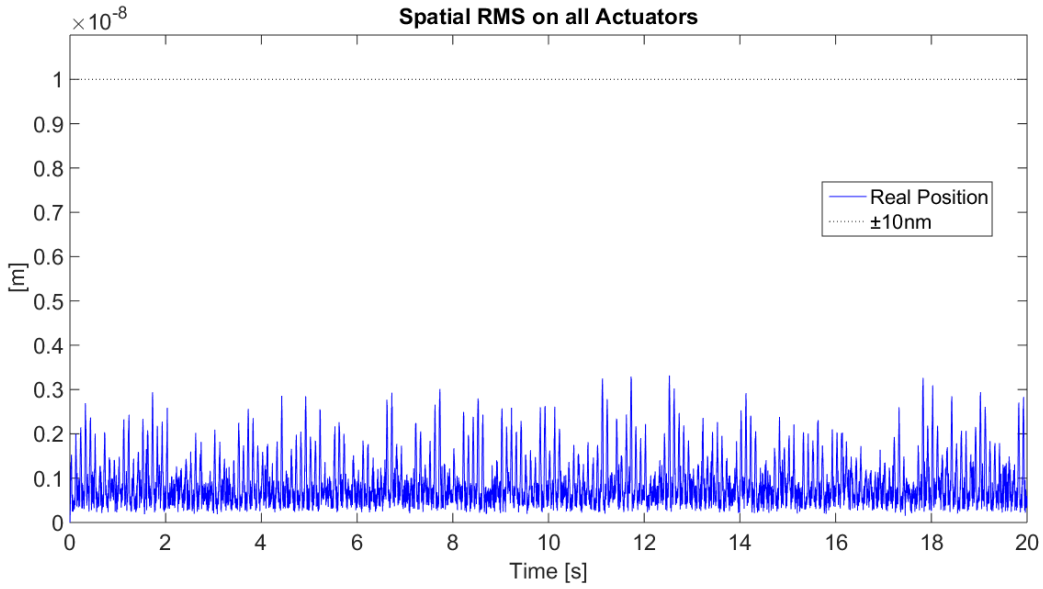

Figure 5.6: Ideal System - error rms over the surface

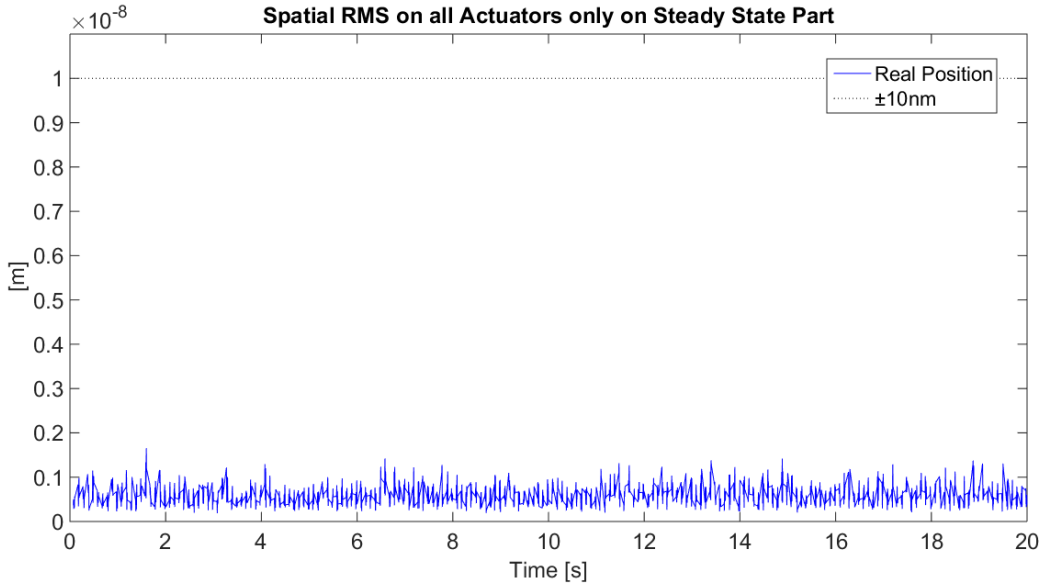

Figure 5.7: Ideal System - error rms only on steady state step part

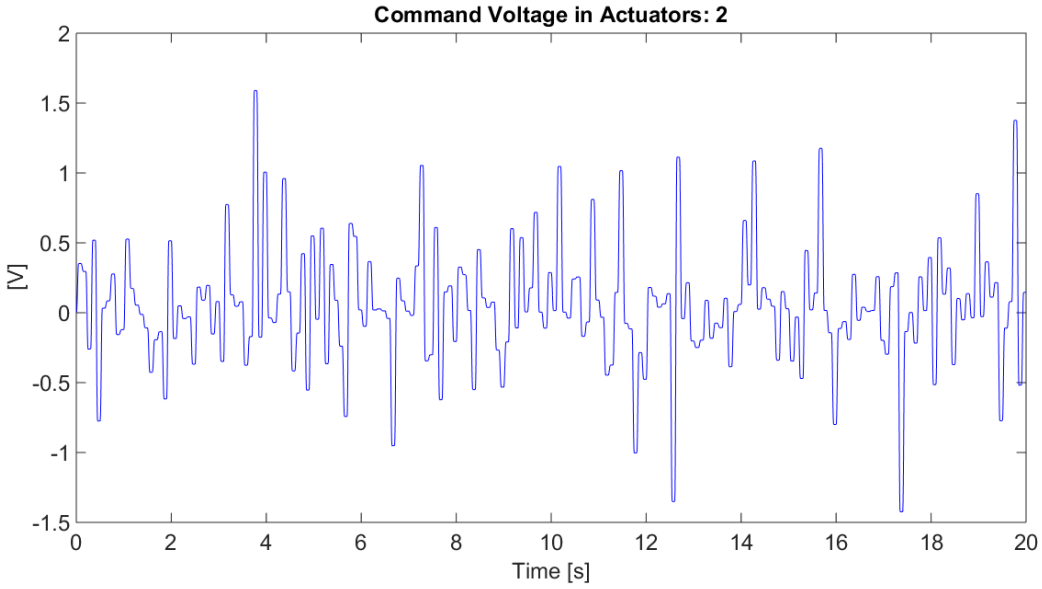

Figure 5.8: Ideal System - control voltage

5.4.1 Almost fully analog implementation

The first approach for a practical implementation of the proposed control scheme is an analog implementation. This should indeed produce the closest response to the theoretical continuous-time case. Obviously the interface with the mirror shape generator, that process data coming from the wave front sensor, necessarily implies a digital part of control hardware, that has to be used also to compute the oxymoronic term of the feedforward. This DA conversion avoids the complete analog transcription of the control project, but its worsening effect is limited only to the static part of the commands, that results affected by voltage quantization. As the digital part of the system is not used for the feedforward shaping, an analog way of implementing the smoothing task was devised. The basic idea was introducing an analog filter to produce a shaping effect similar to the analytic function and then to adopt an electrical circuit for obtaining the PD feedback action.

This solution allows the system to work directly at the lower command frequency. Indeed, the electronics has just to provide the 10Hz command voltage steps, that, once passed through the filter, are properly smoothed before entering the actuator. The result is a significant power saving in the electronic part, that can avoid higher working frequencies, but, on the other hand, the increased number of analog components to realize the circuits has to be properly evaluated. Obviously, the outputs of the analogue shaping do not have the same dynamical characteristics of the ideal analytic version,

but for sure their frequency content is band-limited.

To simulate the presence of the additional analog shaping filter, its dynamics has been added to the existing state space representation. A second-order filter was assumed. Accordingly, its transfer function in the Laplace domain can be written as

$$V_s = \frac{\omega_f^2}{s^2 + 2\,\xi_f\,\omega_f s + \omega_f^2} V \tag{5.9}$$

To be introduced in the state matrix, a time-domain version is needed. We can write

$$\ddot{V}_s + 2\,\xi_f\,\omega_f \dot{V}_s + \omega_f^2\,V_s = \omega_f^2\,V \tag{5.10}$$

which yields

$$\begin{Bmatrix} \dot{V}_s \\ \ddot{V}_s \end{Bmatrix} = \begin{bmatrix} 0 & 1 \\ -\omega_f^2 & -2\,\xi_f\,\omega_f \end{bmatrix} \begin{Bmatrix} V_s \\ \dot{V}_s \end{Bmatrix} + \begin{bmatrix} 0 \\ \omega_f^2 \end{bmatrix} V \tag{5.11}$$

where V_s is the static shaped voltage to be fed into the actuators.

Since all the shaping filters are considered to be equal, it is possible to modify the overall mirror dynamics expressed in Eq. (2.27) by augmenting the state as follows

$$\begin{Bmatrix} \mathbf{q} \\ \dot{\mathbf{q}} \\ \mathbf{i} \\ \mathbf{u}_m \\ \mathbf{z} \\ \mathbf{V}_s \\ \dot{\mathbf{V}}_s \end{Bmatrix}$$

As a result, the state matrix becomes

$$\mathbf{A} = \begin{bmatrix} \mathbf{0} & \mathbf{I} & \mathbf{0} & \mathbf{0} & \mathbf{0} & \mathbf{0} & \mathbf{0} \\ -[\diagdown \omega_i^2 \diagdown] & -[\diagdown 2\xi_i\omega_i \diagdown] & K_t\mathbf{\Phi}^T & \mathbf{0} & \mathbf{0} & \mathbf{0} & \mathbf{0} \\ \mathbf{0} & -\frac{K_e}{L}\,\mathbf{\Phi} & -[\diagdown \frac{R}{L} \diagdown] & \mathbf{0} & \mathbf{0} & [\diagdown \frac{1}{L} \diagdown] & \mathbf{0} \\ b\mathbf{\Phi} & \mathbf{0} & \mathbf{0} & -[\diagdown b \diagdown] & \mathbf{0} & \mathbf{0} & \mathbf{0} \\ \mathbf{0} & \mathbf{0} & \mathbf{0} & [\diagdown a \diagdown] & -[\diagdown a \diagdown] & \mathbf{0} & \mathbf{0} \\ \mathbf{0} & \mathbf{0} & \mathbf{0} & \mathbf{0} & \mathbf{0} & \mathbf{0} & \mathbf{I} \\ \mathbf{0} & \mathbf{0} & \mathbf{0} & \mathbf{0} & \mathbf{0} & -[\diagdown \omega_f^2 \diagdown] & -[\diagdown 2\xi_f\omega_f \diagdown] \end{bmatrix}$$

and the input and output matrices are given respectively, by

$$\mathbf{B}_{ff} = \begin{bmatrix} \mathbf{0} \\ \mathbf{0} \\ \mathbf{0} \\ \mathbf{0} \\ \mathbf{0} \\ \mathbf{0} \\ [\ulcorner \omega_f^2 \urcorner] \end{bmatrix}$$

$$\mathbf{C} = \begin{bmatrix} \mathbf{0} & \mathbf{0} & \mathbf{0} & \mathbf{I} & \mathbf{0} & \mathbf{0} & \mathbf{0} \\ \mathbf{0} & \mathbf{0} & \mathbf{0} & [\ulcorner a \urcorner] & -[\ulcorner a \urcorner] & \mathbf{0} & \mathbf{0} \end{bmatrix}$$

The previous input matrix, now called $\mathbf{B}_{fb}$, is maintained separately, as the feedback action is directly sent to the actuators.

The control gains derived from the continuous-time design are used (see table 5.1). The system simulated is represented by

$$\begin{aligned} \dot{\mathbf{x}}(t) = (\mathbf{A} - \mathbf{B}_{fb}\mathbf{G}\mathbf{C})\,\mathbf{x}(t) \;+\; \mathbf{B}_{ff}\,(\,\mathbf{V}_{c_{ff},k} + \mathbf{G}\mathbf{y}_k^r\,) \;+\; ... \\ ... + [\,\mathbf{B}_d \quad (\mathbf{B}_n - \mathbf{B}\mathbf{G}\mathbf{D}_n)\,] \begin{Bmatrix} \mathbf{f}_d(t) \\ \mathbf{n}(t) \end{Bmatrix} \end{aligned} \tag{5.12}$$

where $\mathbf{V}_{c_{ff},k}$ includes only the static part of the feedforward, without the shaping function. The response reported in figures 5.9, 5.10, 5.11 shows the peculiar fast climbs of the analog filter, that induce quickly damped oscillations. The result is relevant errors in the transient part of the commands (figures 5.12, 5.13, 5.14), but a steady state mean error (figure 5.15) well below the 10nm boundary. This latter performance is indeed dictated only by the static quantization voltage error.

It should be noticed the absence of the mass and damping feedforward terms. These has been discarded in this implementation due to the excessive complexity involved in the analog realization of a circuit capable also of extracting the shaping derivatives and scaling them to the correct value. The amount of power consuming components involved would indeed produce an unbearable request of energy. It could be also added that the mirror could be classified as a stiffness dominated system, thus the dominant feedforward part is the $\mathbf{K}_v^*$ proportional one and the loss of the other two terms only marginally affected the results.

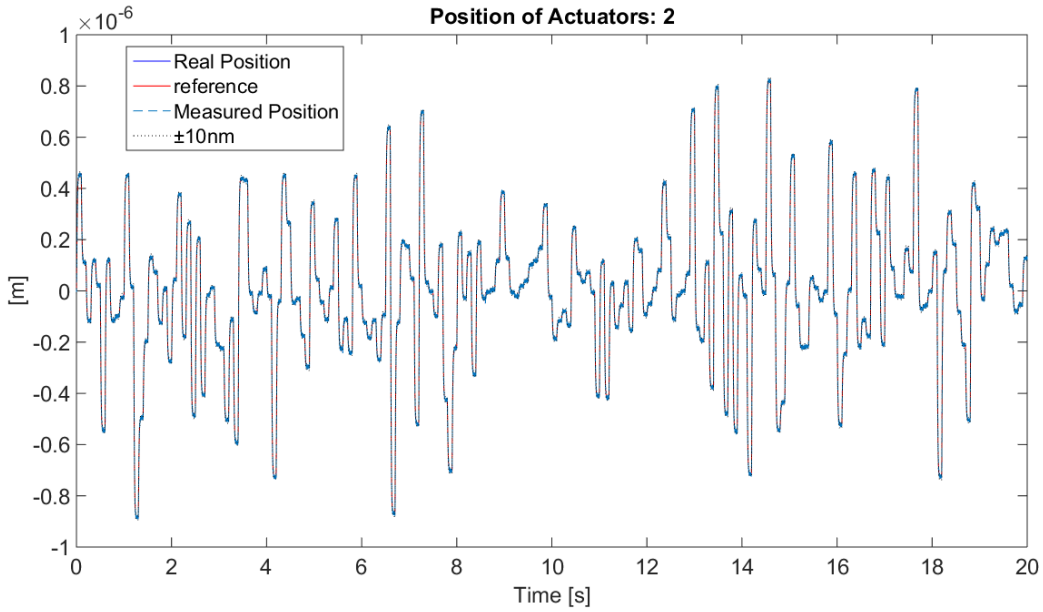

Figure 5.9: Full Analog System - response

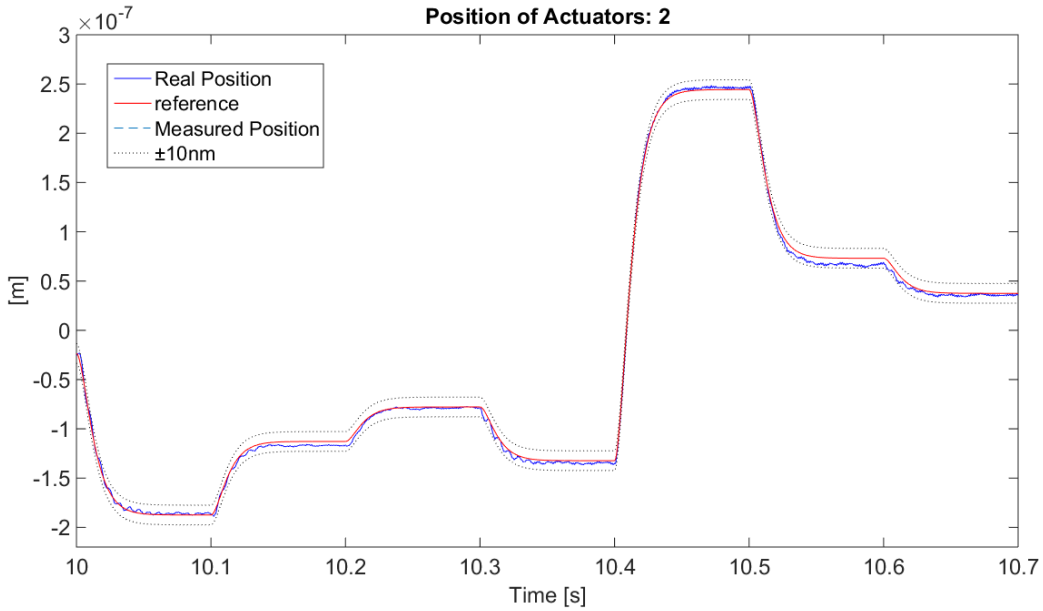

Figure 5.10: Full Analog System - response detail

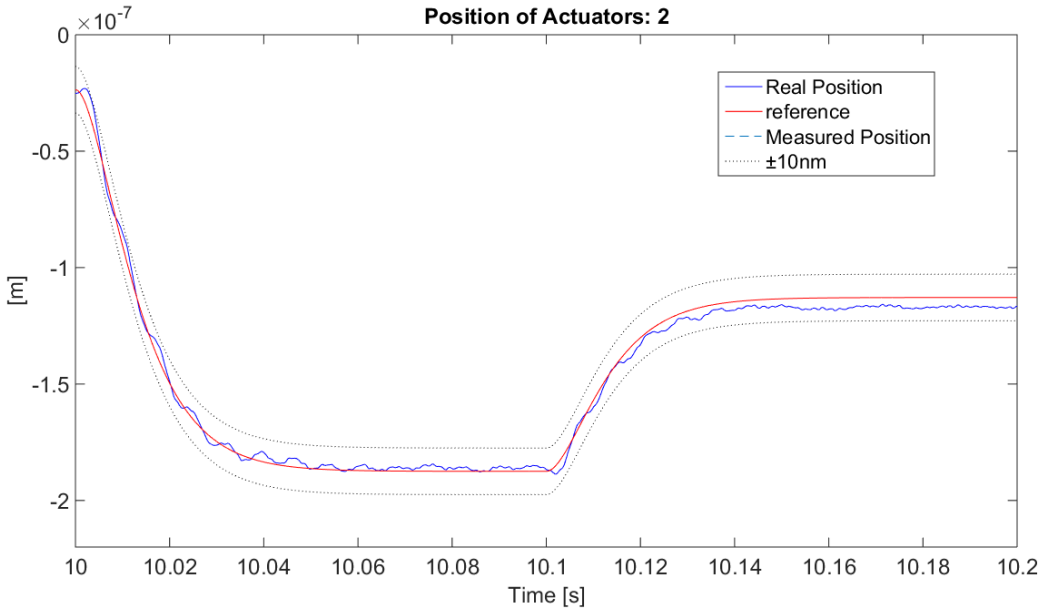

Figure 5.11: Full Analog System - response detail

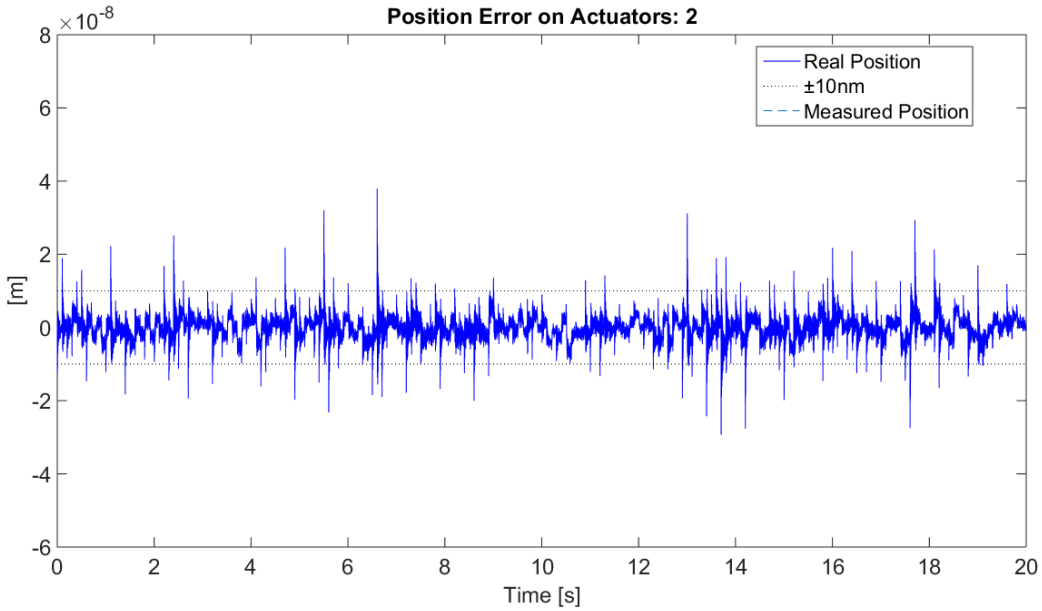

Figure 5.12: Full Analog System - error

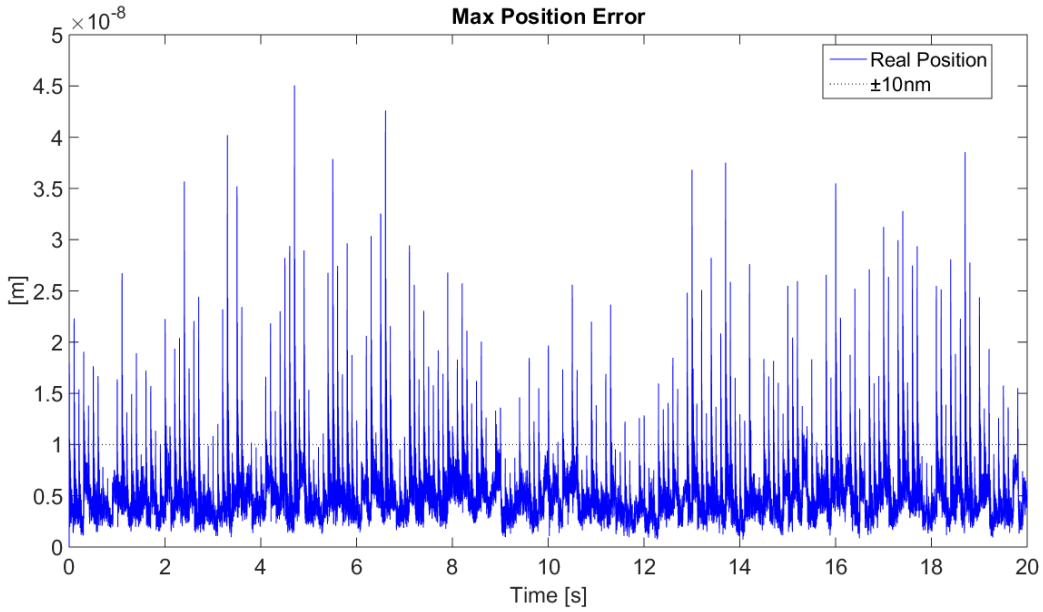

Figure 5.13: Full Analog System - maximum error over the surface

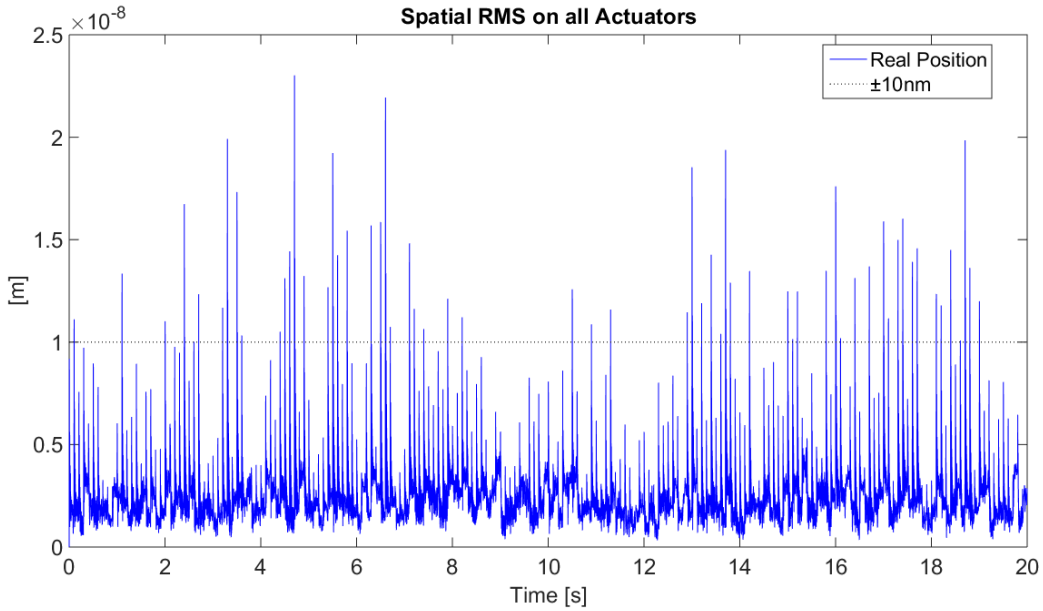

Figure 5.14: Full Analog System - error rms over the surface

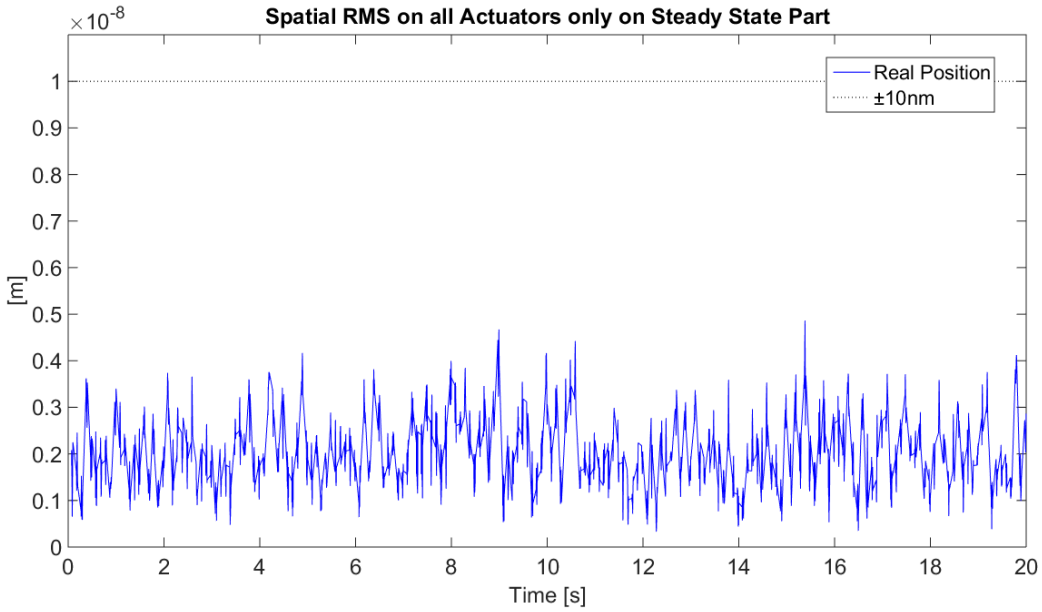

Figure 5.15: Full Analog System - error rms on steady state step part

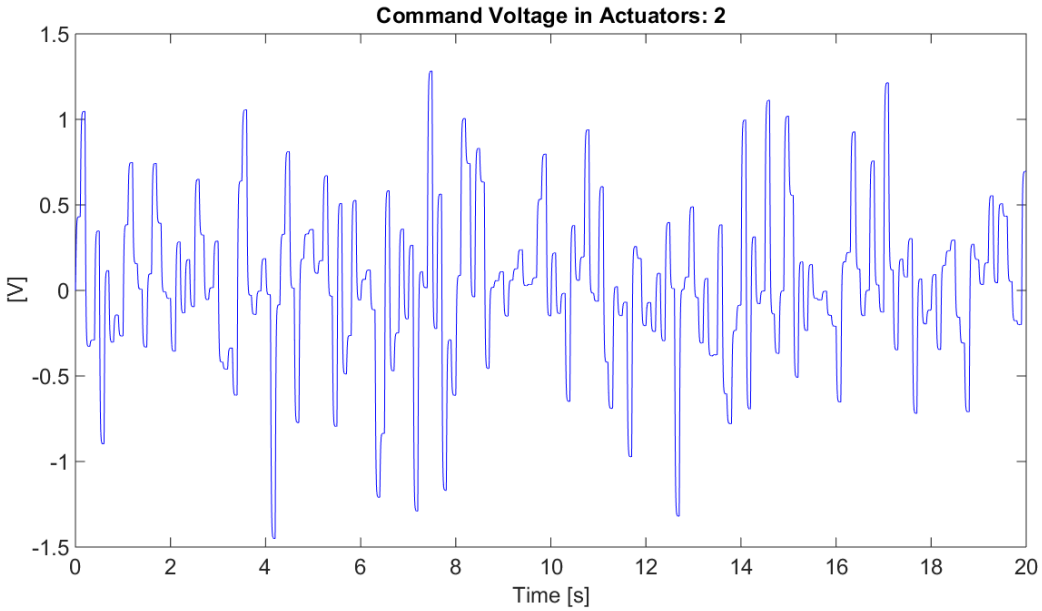

Figure 5.16: Full Analog System - control voltage detail

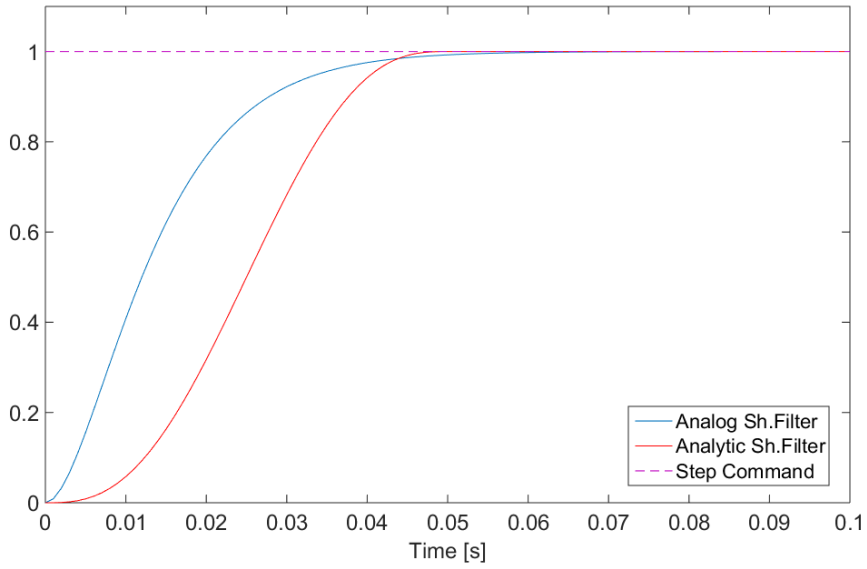

Figure 5.17: Analog shaping filter tuning

Analog Shaping Filter

To implement an effective shaping filter having the transfer function represented by Eq. (5.9), the characteristic parameters ω_f and ξ_f must be tuned to obtain a dynamic behavior which is similar to the analytic shaping in terms of shape and rising time. The damping coefficient of the two poles has been set $\xi_f = 1.0$, corresponding to the critical value, so that the correct smooth shape of the response without overshooting is obtained. The frequency of the poles was tuned to regulate the response promptness. It has been set $\omega_f = 140\text{rad/s}$ to obtain a settling time to 1% of the reference within half the command length. A comparison between the analytic and the analog versions of the filter is reported in figure 5.17.

The physical implementation of the filter can be obtained using an electric circuit with passive and reactive elements of the kind in figure 5.18, where the only active component is an OpAmp. The resistance and capacitance values can be set according to the relation $\omega_f = 1/RC$. This kind of filter has to be applied on each actuation line, thus it has to be proportionally taken into account in the power consuming components budget.

PD Electric Circuit

The analog implementation involves also an electric circuit to realize the PD controller. It is thus necessary to design also a control circuit able to both

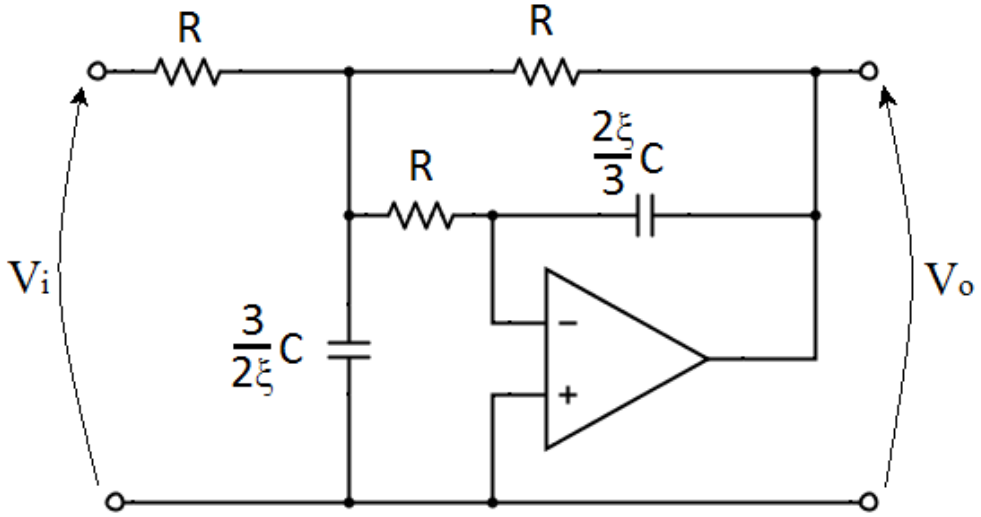

Figure 5.18: Analog shaping filter circuit [40]

amplify and derive the sensor outputs. From classical PID theory, it has been taken a general PD scheme as reported in figure 5.19. The relation governing the described system is

$$V_o = -\frac{R_2}{R_1}\left(V_i + R_1\, C\, \frac{dV_i}{dt}\right) \tag{5.13}$$

The proportional gain can be imposed by properly exploiting

$$K_P = \frac{R_2}{R_1} \tag{5.14}$$

and accordingly the derivative gain

$$K_D = \left(\frac{R_2}{R_1}\right) R_1\, C \tag{5.15}$$

5.4.2 Analog implementation of the feedback part

The second approach which can be adopted for the practical implementation of the combined feedback-feedforward control under investigation relies on realizing only the feedback action through an analog electric circuit and to digitally implement the smoothing action, avoiding thus the use of the

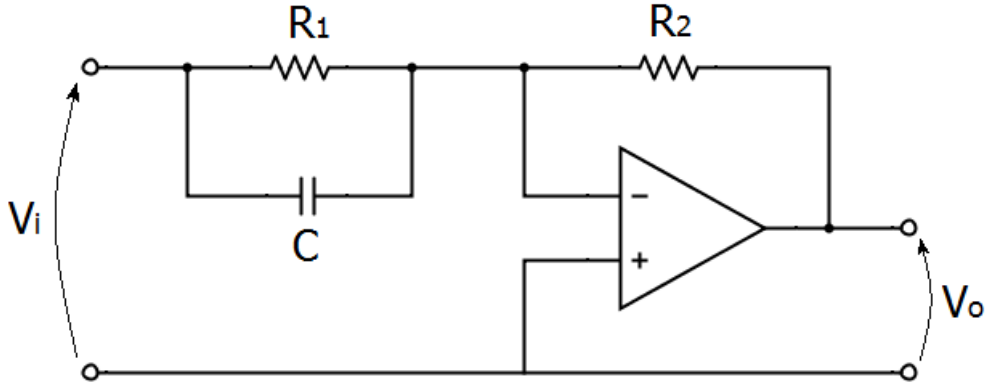

Figure 5.19: PD electrical circuit [41]

amount of operational amplifiers, required by the shaping filters. It is indeed to notice the impossibility to fully discard the digital components, that can be thus exploited also for realizing the correct analytic shaping. It is obvious that this choice, if on one side reduces the number of analog components, on the other side forces the calculator to send signals at a higher frequency.

The same architecture presented in the previous section is used to provide the desired PD control gains. As a result, the feedback control part is completely analog and is only affected by the circuit noise. Accordingly, the feedback controller can still be effectively designed following the continuous-time formulation presented in the previous section, i.e., the control gains reported in table 5.1 can be used. On the other side, the feedforward part of the control system and the reference signal are digitally realized. Therefore, the quantization effects introduce a limited resolution in the reference position, which marginally affect the accurate positioning of the mirror and the transient smoothness of the commanded signals.

The control law thus implemented presents a mixed continuous-piecewise form

$$\mathbf{V}_{c,j} = \mathbf{V}_{cff,j} + \mathbf{V}_{cfb,j}(t) \tag{5.16}$$

where $\mathbf{V}_{cff,j}$ is still given by Eq. (5.23), whereas the feedback term becomes

$$\begin{aligned} \mathbf{V}_{cfb,j}(t) &= -\mathbf{G}(\mathbf{y}(t) - \mathbf{y}_j^r) \\ &= -\mathbf{G}\begin{Bmatrix}\mathbf{y}_u(t)\\ \mathbf{y}_v(t)\end{Bmatrix} + \mathbf{G}\begin{Bmatrix}\mathbf{u}_k^r + (\mathbf{u}_{k+1}^r - \mathbf{u}_k^r) f_{sh}(t_j)\\ \mathbf{0}\end{Bmatrix} \end{aligned} \tag{5.17}$$

The system response is then computed using a continuous time simulation

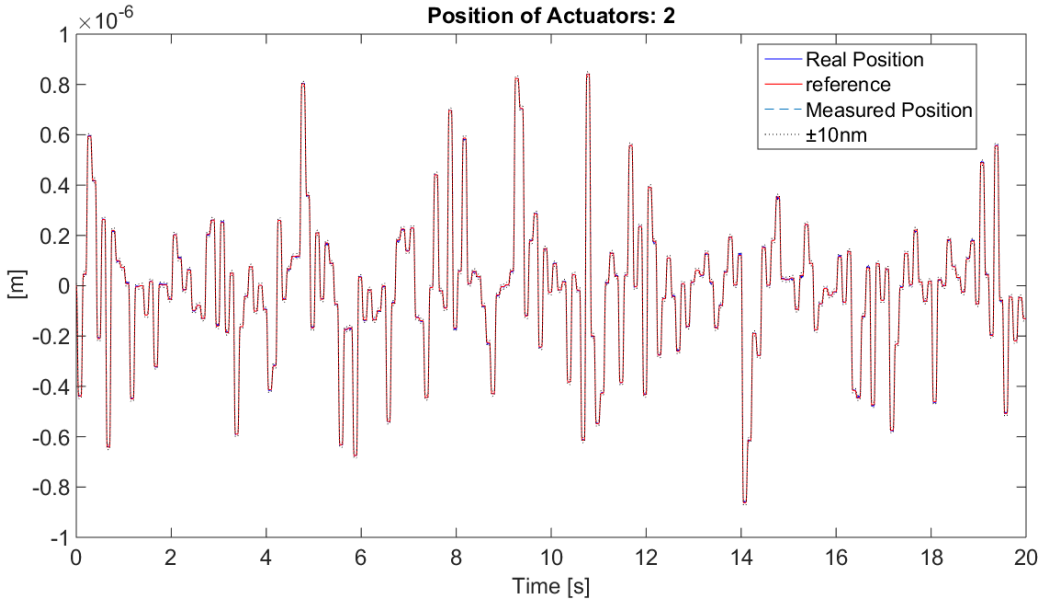

Figure 5.20: Analog Feedback - response

along each control interval. The system simulated can be described as follows

$$\begin{aligned}\dot{\mathbf{x}}(t) = (\mathbf{A} - \mathbf{BGC})\,\mathbf{x}(t) \;+\; \mathbf{B}\,(\,\mathbf{V}_{c_{ff},j} + \mathbf{G}\mathbf{y}_j^r\,) \;+ \ldots \\ \ldots + \,[\,\mathbf{B}_d \quad (\mathbf{B}_n - \mathbf{BGD}_n)\,]\left\{\begin{matrix}\mathbf{f}_d(t)\\ \mathbf{n}(t)\end{matrix}\right\}\end{aligned} \tag{5.18}$$

The results in terms of mirror positioning immediately show a similar performance compared to the almost full analog case. An actuator response is reported in figures 5.20, 5.21 and 5.22. The error analysis shown in figures 5.23, 5.24, 5.25, 5.26 highlights dynamical characteristics not yet at full continuous time level, but still considerable good. The maximum and rms values of the position error over the mirror surface exhibit oscillatory transients with marginal peaks crossing the tolerance boundaries. Nevertheless, the steady state error fully satisfies the closed-loop requirements, reaching maximum values of about 6nm.

A specific comment about the control frequency should be given. Indeed, within the present hybrid analog-digital architecture, the only terms subjected to a digital implementation and thus affected by the values of the control frequency are the feedforward voltage and the reference position voltage. Modifying the frequency would affect only the smoothness of those signals, without having any effect on the effectiveness of the feedback action. It is thus possible to tune the control frequency with the aim of finding a tradeoff between power consumption and smoothness quality of the input sig-

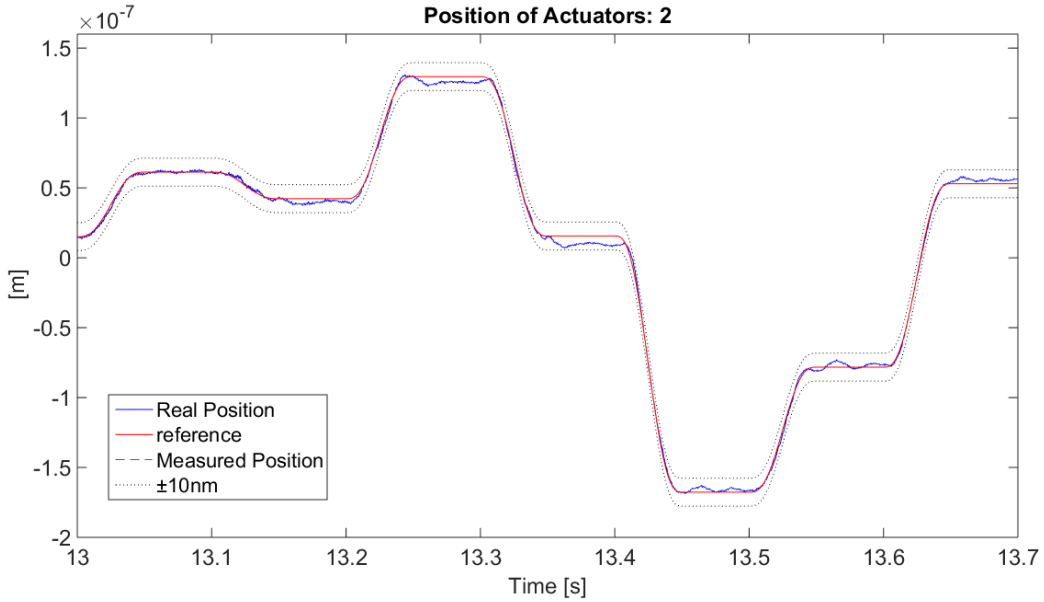

Figure 5.21: Analog Feedback - response detail

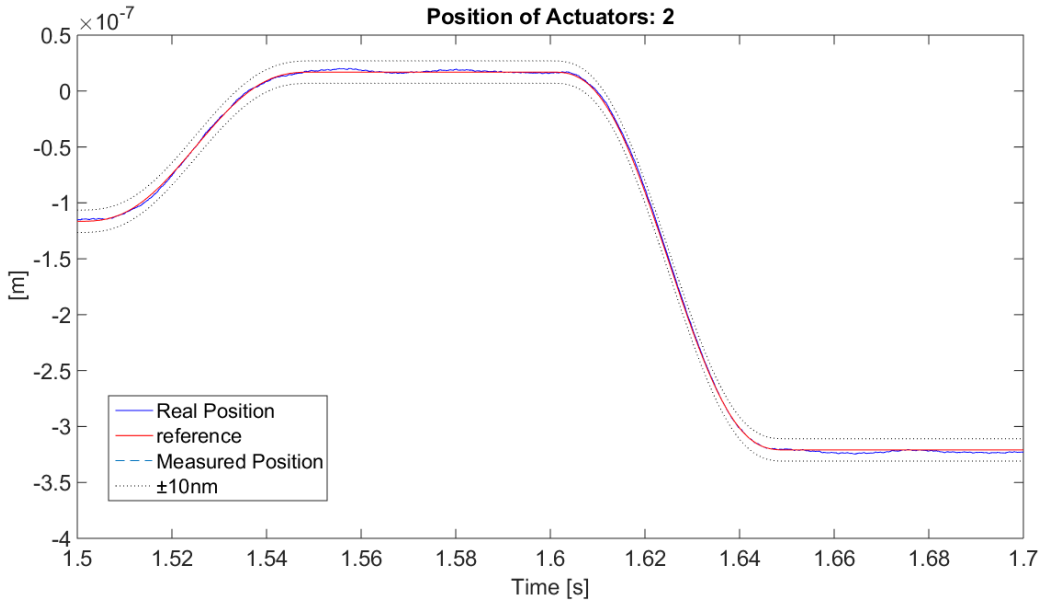

Figure 5.22: Analog Feedback - response detail

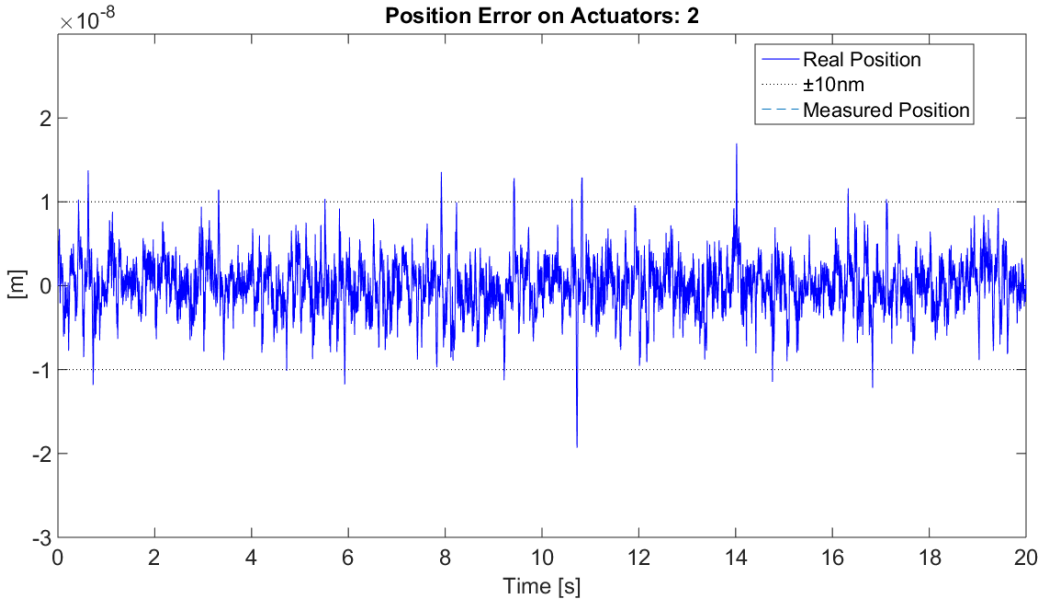

Figure 5.23: Analog Feedback - error

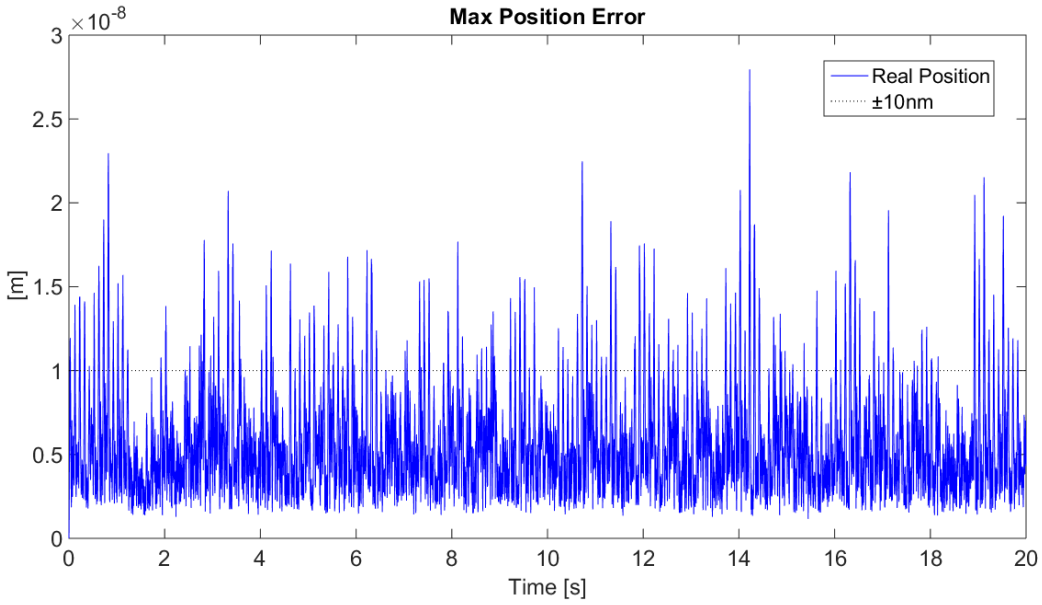

Figure 5.24: Analog Feedback - maximum error over the surface

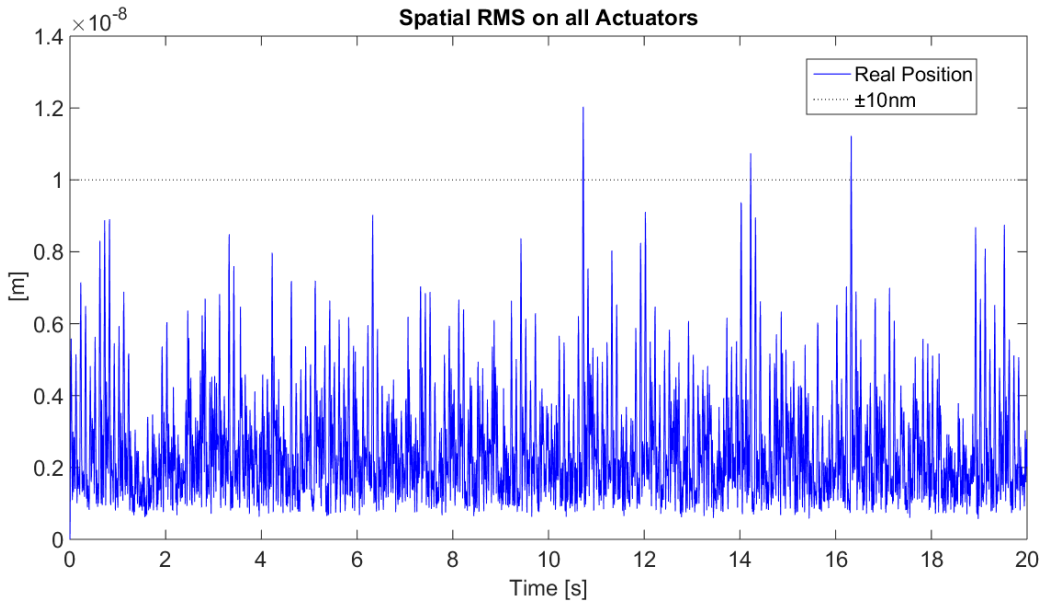

Figure 5.25: Analog Feedback - error rms over the surface

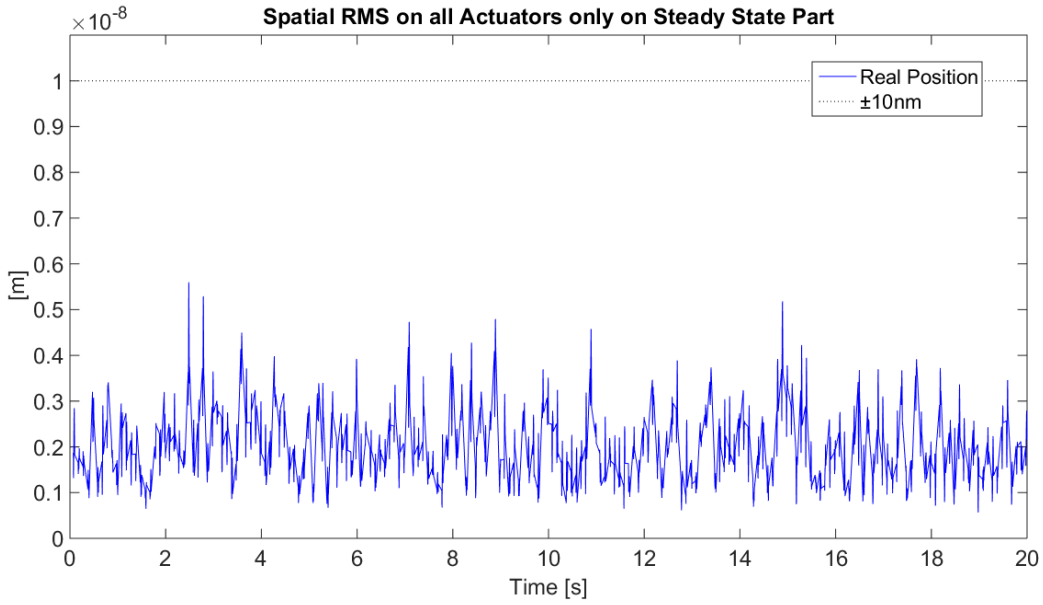

Figure 5.26: Analog Feedback - error rms only on steady state step part

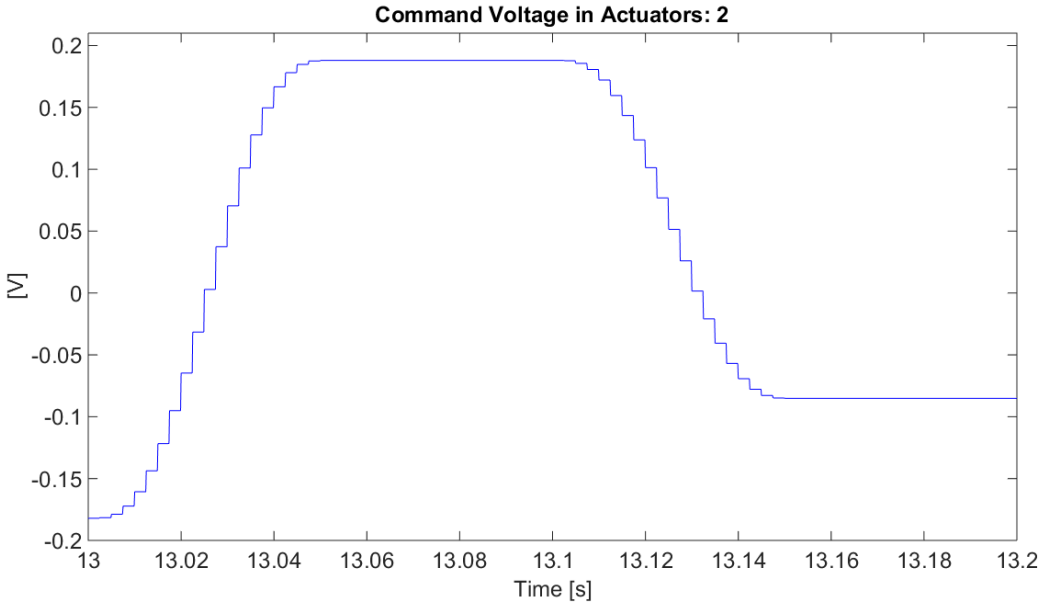

Figure 5.27: Analog Feedback (400Hz sampled inputs) - control voltage

nals. It is noted that a reduced control frequency increases the amplitude of the small steps used to approximate the smooth shaping filter expression (see figure 5.27), increasing the energetic content of the signal at high frequencies. The minimum frequency reachable without deeply affecting the performance is 400Hz. It is evident in figures 5.28, 5.29 and 5.30 how the rough piecewise voltage commands excite the low damped high frequency structural modes. The steady state response shown in figure 5.32 still falls within the required boundaries, even if there are evident oscillations that substantially raise its average value.

5.4.3 Discrete-time design and fully digital implementation

The final approach is based on a fully digital implementation of the combined feedback-feedforward control at a sampling frequency of 2kHz.

In a fully digital implementation, sensor measurements are first acquired and then the corresponding information can be numerically elaborated as required. Therefore, the velocity variables involved in the derivative action of the feedback controller can be obtained by numerical differentiation of the sensor positions. According to the pseudo differentiator equation (2.21), it is possible to derive a finite-difference representation of the derivative operation, ready to be coded in the processor unit. The time-domain representa-

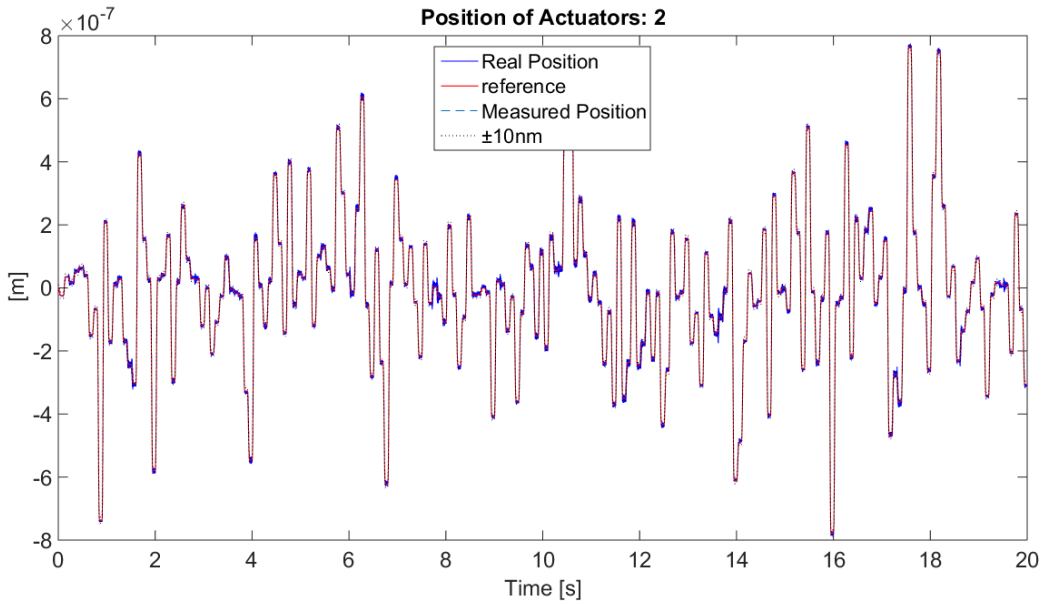

Figure 5.28: Analog Feedback (400Hz sampled inputs) - response

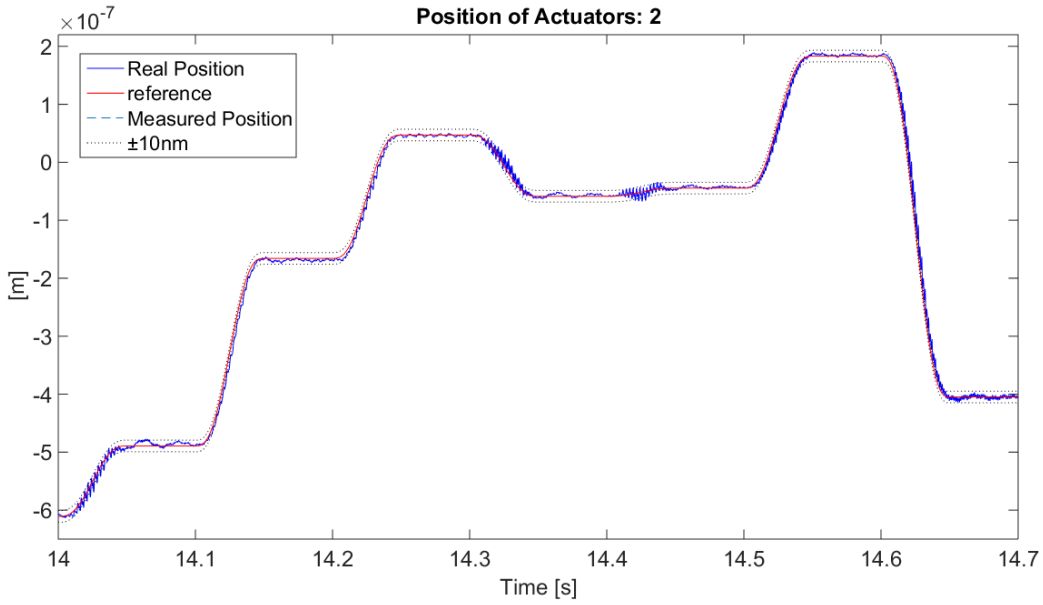

Figure 5.29: Analog Feedback (400Hz sampled inputs) - response detail

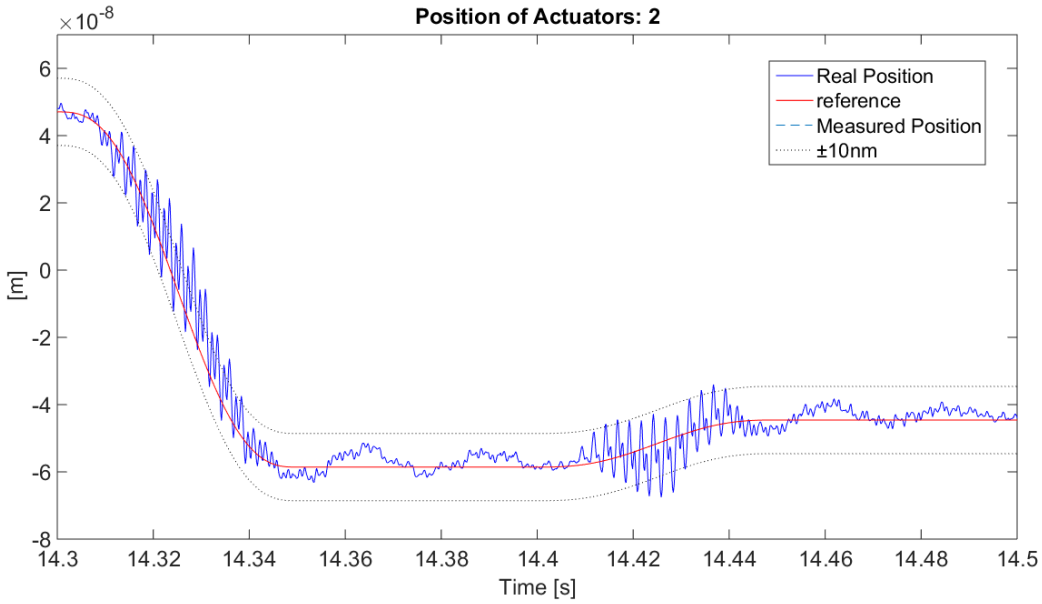

Figure 5.30: Analog Feedback (400Hz sampled inputs) - response detail

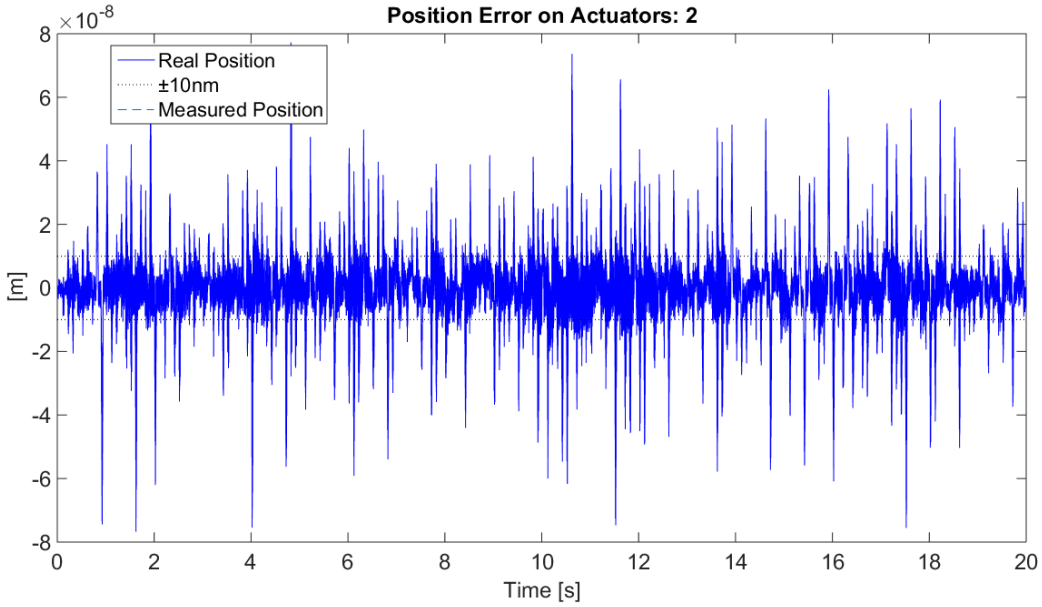

Figure 5.31: Analog Feedback (400Hz sampled inputs) - error

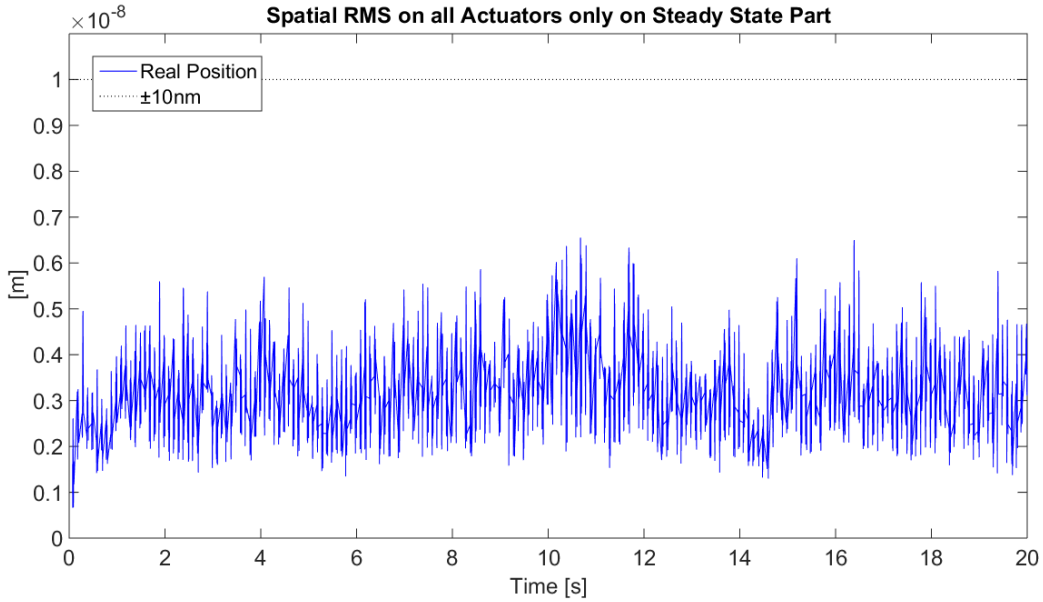

Figure 5.32: Analog Feedback (400Hz sampled inputs) - error rms on steady state step part

tion of the differentiation filter is

$$\dot{y}_v + a\, y_v = a\, \dot{y}_u \tag{5.19}$$

Then, using the Euler method for approximation of the derivatives, the following finite-difference equation is obtained

$$\frac{y_{v,k} - y_{v,k-1}}{\Delta t} + a\, y_{v,k} = a\, \frac{y_{u,k} - y_{u,k-1}}{\Delta t} \tag{5.20}$$

which yields

$$y_{v,k} = \frac{y_{v,k-1} + a\,(y_{u,k} - y_{u,k-1})}{1 + a\,\Delta t} \tag{5.21}$$

Due to the relatively low sampling frequency assumed in this approach, the continuous-time controller was unable to give satisfactory results. Hence, the discrete-time formulation has been exploited to have a design which properly accounts for the digital implementation of the control system. Using the same settings reported in section 5.2, with only small differences to adapt the system to the absence of derivative and integral filters, a discrete-time suboptimal feedback control has been designed. The time delay has been set to one complete sampling period, which represents an overestimated upper-bound margin of the actual time required to perform the computations associated with the control action. The resulting gains are reported in table 5.2.

K_P	$1672,1$
K_D	$3,1$

Table 5.2: Discrete Time control Project with delay

A significant reduction of both values is worth noting with respect to the continuous-time design. This limitation results from the need of avoiding closed-loop instability.

The discrete-time version of the control law expressed in Eq. (5.5) can be written as follows

$$\mathbf{V}_{c\,,j} = \mathbf{V}_{c\,ff\,,j} + \mathbf{V}_{c\,fb\,,j} \tag{5.22}$$

where j is the 2kHz control step index, not to be confused with the 10Hz command step. Being the control voltage a piecewise step function, for the j^{th} control step that goes from t_j to t_{j+1}, it could be specified the term

$$\begin{aligned}\mathbf{V}_{c\,ff\,,j} = \mathbf{V}_{c\,ff,k} + \{\,[\urcorner\alpha_{\llcorner}]\overline{\mathbf{V}}_{c,k} + (\mathbf{I} - [\urcorner\alpha_{\llcorner}])\mathbf{V}_{c\,ff,k} - \mathbf{V}_{c\,ff,k} + ... \\ ... + \mathbf{K}_v^*\,\mathbf{u}_{k+1}^r - (\,[\urcorner\alpha_{\llcorner}]\,\overline{\mathbf{y}}_{u,k} + (\,\mathbf{I} - [\urcorner\alpha_{\llcorner}]\,)\,\mathbf{u}_k^r\,)\,\}\,f_{sh}(t_j) + ... \\ ... + [\,\mathbf{C}_v^*\,\dot{f}_{sh}(t_j) + \mathbf{M}_v^*\,\ddot{f}_{sh}(t_j)\,]\,(\mathbf{u}_{k+1}^r - \mathbf{u}_k^r)\end{aligned} \tag{5.23}$$

and the delayed feedback term

$$\begin{aligned}\mathbf{V}_{c\,fb\,,j} &= -\mathbf{G}(\mathbf{y}_{j-1} - \mathbf{y}_{j-1}^r) \\ &= -\mathbf{G}\begin{Bmatrix}\mathbf{y}_{u\,,j-1}\\ \mathbf{y}_{v\,,j-1}\end{Bmatrix} + \mathbf{G}\begin{Bmatrix}\mathbf{u}_k^r + (\mathbf{u}_{k+1}^r - \mathbf{u}_k^r)f_{sh}(t_{j-1})\\ \mathbf{0}\end{Bmatrix}\end{aligned} \tag{5.24}$$

The discrete time system assumes thus the form

$$\begin{aligned}\dot{\mathbf{x}}_{j+1} = \mathbf{A}\mathbf{x}_j + \mathbf{B}\,(\,\mathbf{V}_{c\,ff\,,j} - \mathbf{G}\,\mathbf{y}_{j-1} + \mathbf{G}\,\mathbf{y}_{j-1}^r\,) + ... \\ ... + [\,\mathbf{B}_d \quad -\mathbf{B}\mathbf{G}\mathbf{D}_n\,]\begin{Bmatrix}\mathbf{f}_d\\ \mathbf{n}\end{Bmatrix}\end{aligned} \tag{5.25}$$

With the feedback gain matrix resulting from the above discrete-time design, the closed-loop response of the system was simulated. Figures 5.33, 5.34 and 5.35 show that the closed-loop dynamics is largely affected by discrete-level inputs and the adoption of control gains of limited magnitude. The position history presents a more stable behavior than the open loop version. However, even if it remains close to the reference, the actual position has difficulty in converging to the correct value. The error (see figures 5.36,5.36) clearly exceeds 10nm boundaries and the steady state performance (see figure 5.38) does not meet the prescribed requirements. This is due both to the selected low value of control frequency and to quantization effects related to

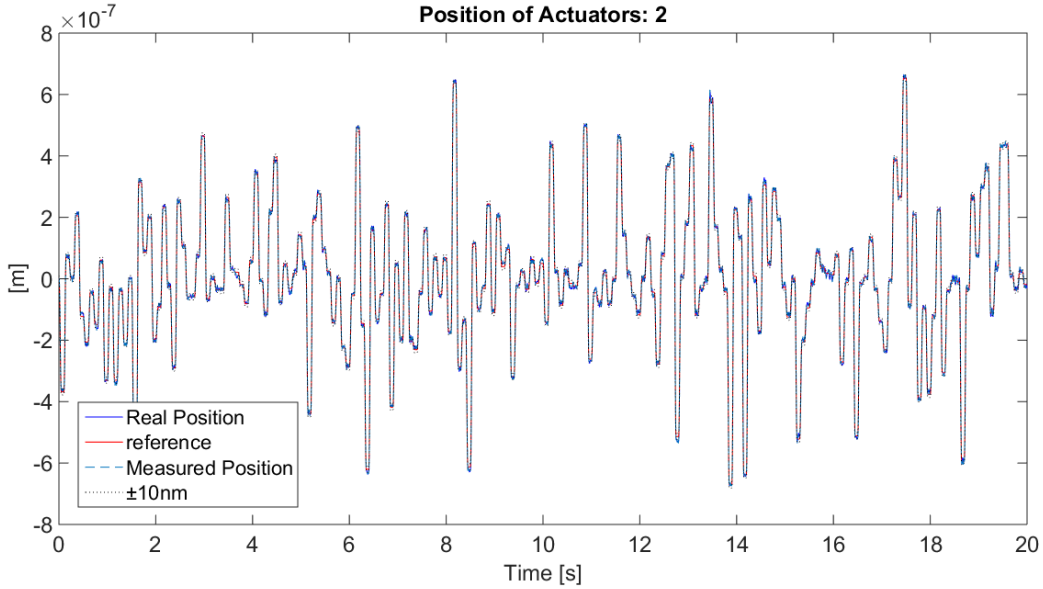

Figure 5.33: Full Digital System (2kHz) - response

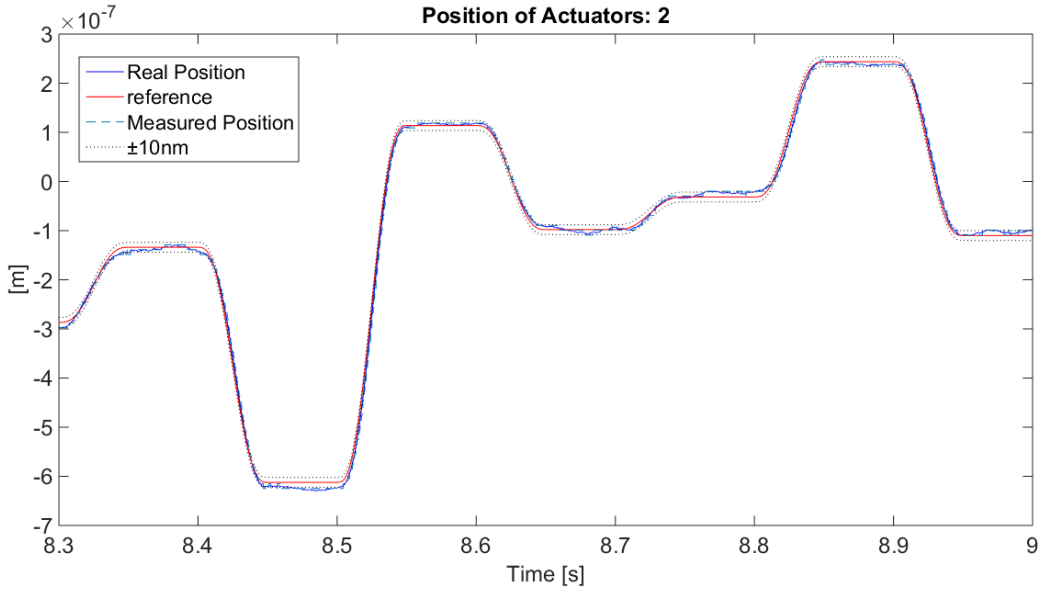

Figure 5.34: Full Digital System (2kHz) - response detail

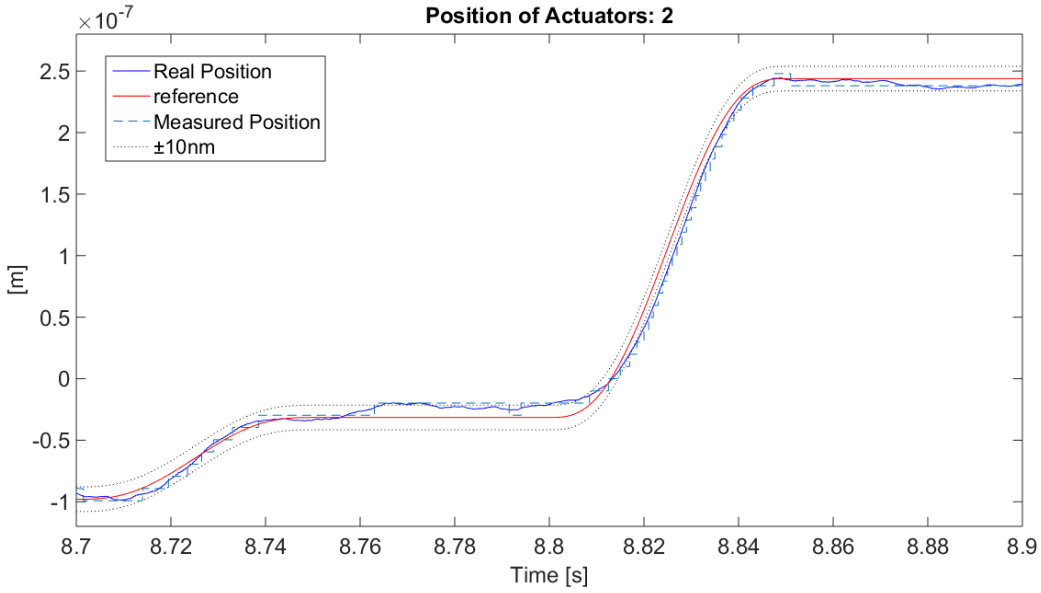

Figure 5.35: Full Digital System (2kHz) - response detail

the finite resolution of AD and DA converters, that, on the contrary of the previous analog cases, deeply affect also the feedback control.

It should be finally highlighted that this third solution, despite completely discarding the analog circuits of the previous cases, force the on-board computer to work at a higher frequency and to perform more tasks due to the necessity to numerically compute also the feedback voltage.

Quantization effects

If the control hardware is correctly designed, the presence of discrete-level sensor and control signals would not significantly affect the control effectiveness. This implies that the design of the controller and the choice of the hardware for its digital implementation should be carried out in a collaborative procedure for best performance. This approach should typically involve the selection of the most suitable devices that can guarantee the successful implementation of the control law.

The present control problem exhibits a peculiar situation. The feedforward control term requires to generate a quasi-static part whose order of magnitude is in the unit voltage range, whereas the feedback action results in a contribution which is several orders of magnitude lower, mainly due to the small control gains allowed by the prevention of structural instability. This fact, along with the limited number of bits of the DA converter, implies that the resolution of the feedback voltage is very low. In particular, the

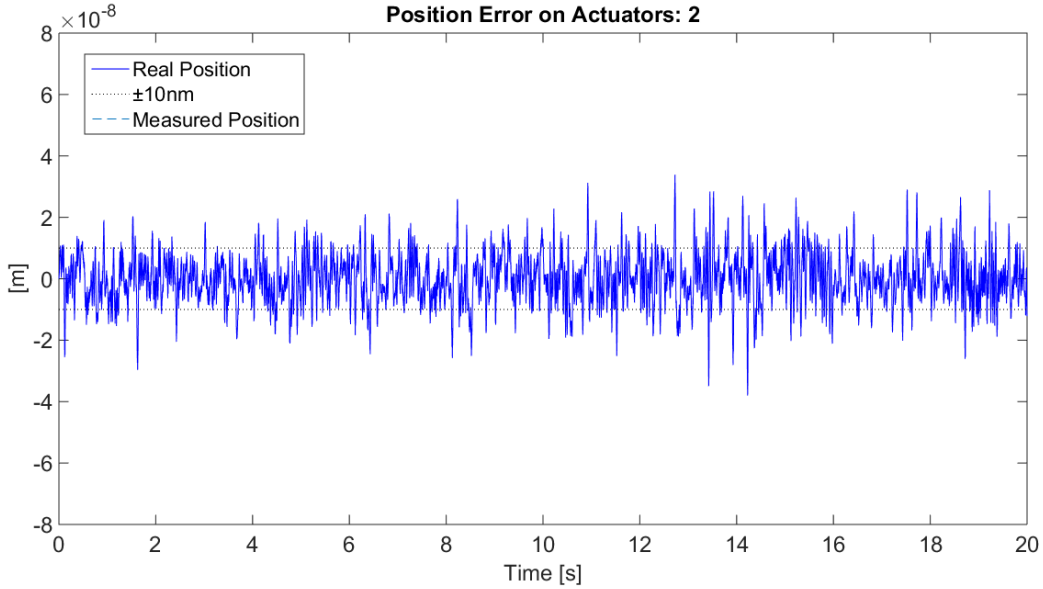

Figure 5.36: Full Digital System (2kHz) - error

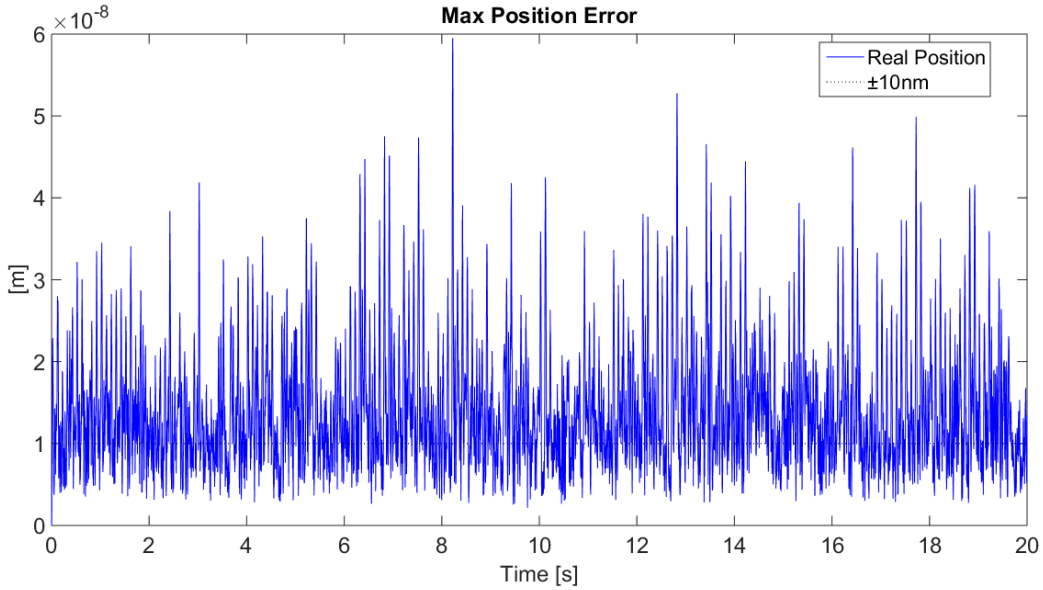

Figure 5.37: Full Digital System (2kHz) - maximum error over the surface

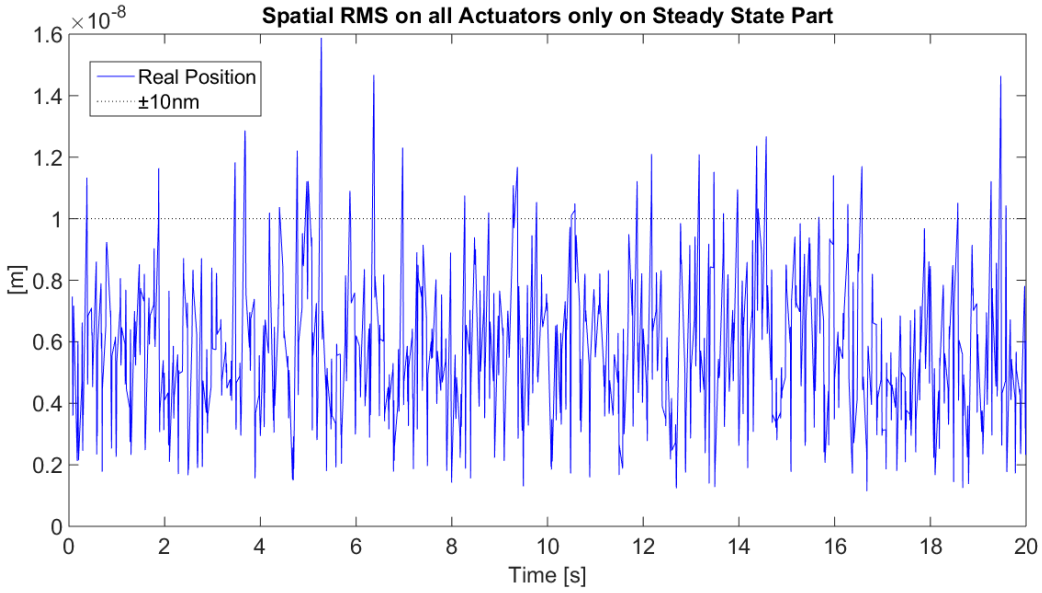

Figure 5.38: Full Digital System (2kHz) - error rms on steady state step part

amplitude of the feedback voltage is smaller than the quantization level. As a result, the feedback control action becomes a bang-bang control, as shown in figure 5.39, and the beneficial effect provided by the feedback contribution is completely lost.

Another quantization effect, presents also in the previous analog solutions, is related to the error introduced in the static positioning by the quantized reference. Indeed, half a quantum error in the voltage value commanding the static positioning of the mirror corresponds to an error of several nanometers. To show this effect, a specific simulation has been carried out, where the system has been driven by a high fidelity feedforward scheme with a control voltage offset of half a quantum. Results are summarized in figures 5.40 and 5.41. It is worth mentioning that, since the offset in the voltage signal is equal and with the same sign over the whole surface, there is a cumulative effect on the static positioning that amplifies the error. Nevertheless, it is clear that the requirements on the accurate positioning and the effects due to the quantization of the voltage are of the same order. Such a behavior calls this fully digital implementation into question for obtaining the required precision on the shape of the mirror.

This solution clearly is not acceptable without tolerating a steady state error which does not satisfy the closed-loop requirements. A potential alternative could be the adoption of AD and DA converters having more bits, in order to increase the resolution of the quantized output and input signals.

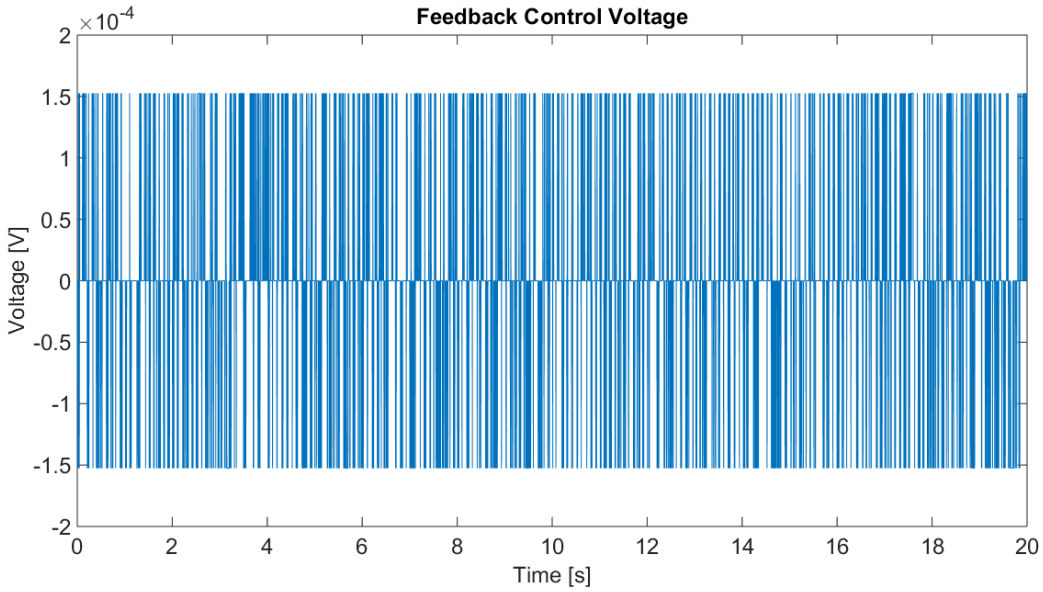

Figure 5.39: Full Digital System (2kHz) - FB control voltage

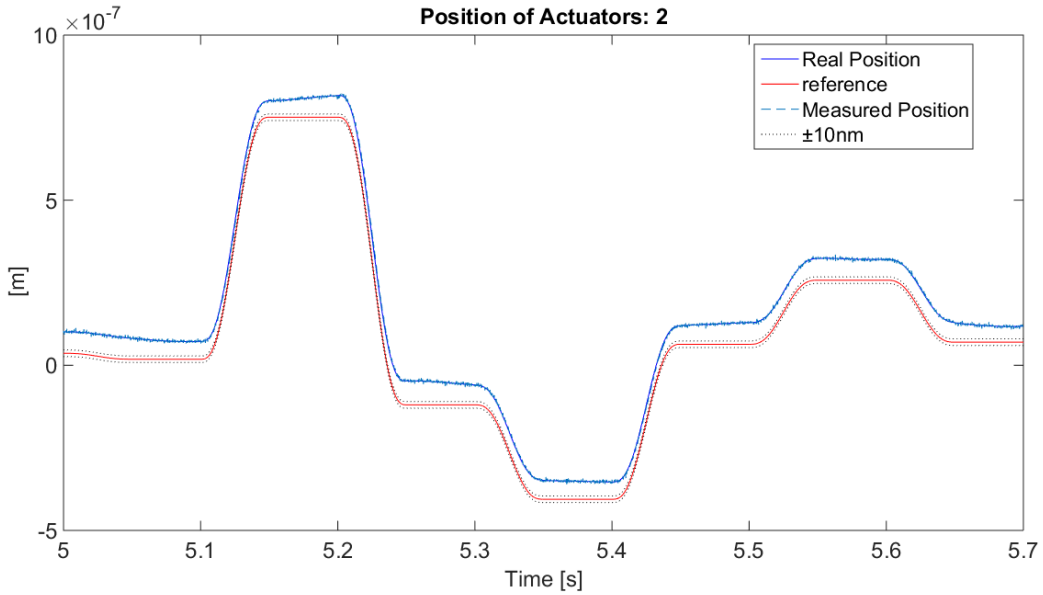

Figure 5.40: Half Quantum Voltage Offset - response

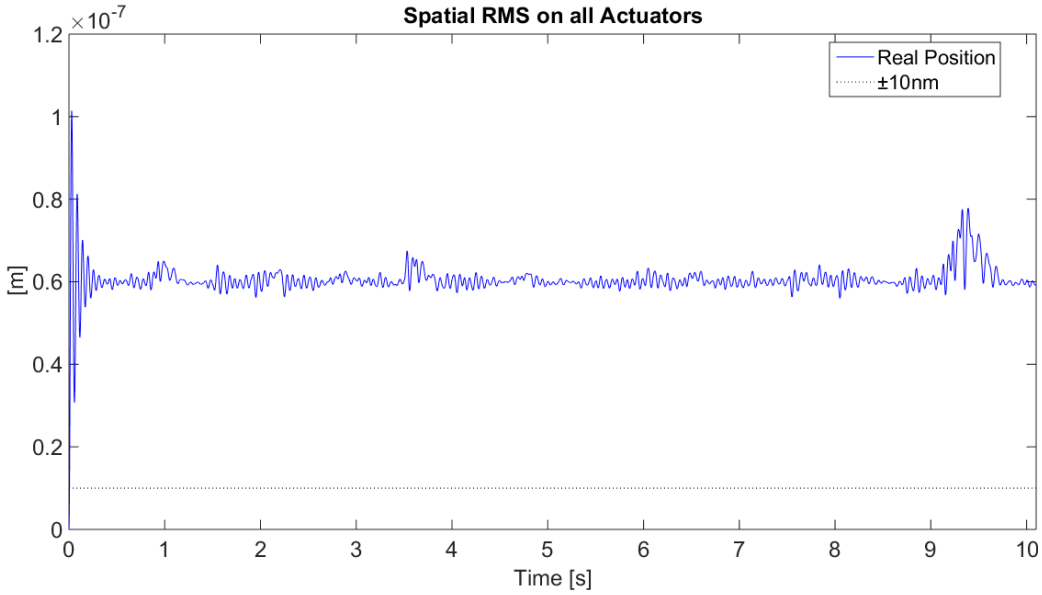

Figure 5.41: Half Quantum Voltage Offset - error rms over the surface

An analysis has been carried by simulating input/output devices having 17 bits. All the other parameters are kept fixed. The response shown in figure 5.42 still suffers from a slow convergence to the reference position. Instead, it can be observed from the steady state error depicted in figure 5.43 that one bit more is enough in achieving the required accuracy. However, it must be stressed that AD and DA converters with a large number of bits would be more energy-consuming and so their adoption should be critically evaluated.

5.4.4 Solutions Comparison

In this final section the three implementable solutions are briefly compared. The main criterion used is a preliminary components budget, summarizing their number and characteristics.

This also constitutes a qualitative indication of the power consumption of the embarked hardware, that on a spacecraft usually is an important parameter due to the limited available resources. Thus only the active elements, that differentiate the various configurations, are reported.

It should be underlined that, in the analog cases, each actuation channel has its own filter and PD controller, whose components thus should be accounted many times as the actuation channels are. This summary is reported in table 5.3.

A detailed study should be done for identifying the less consuming so-

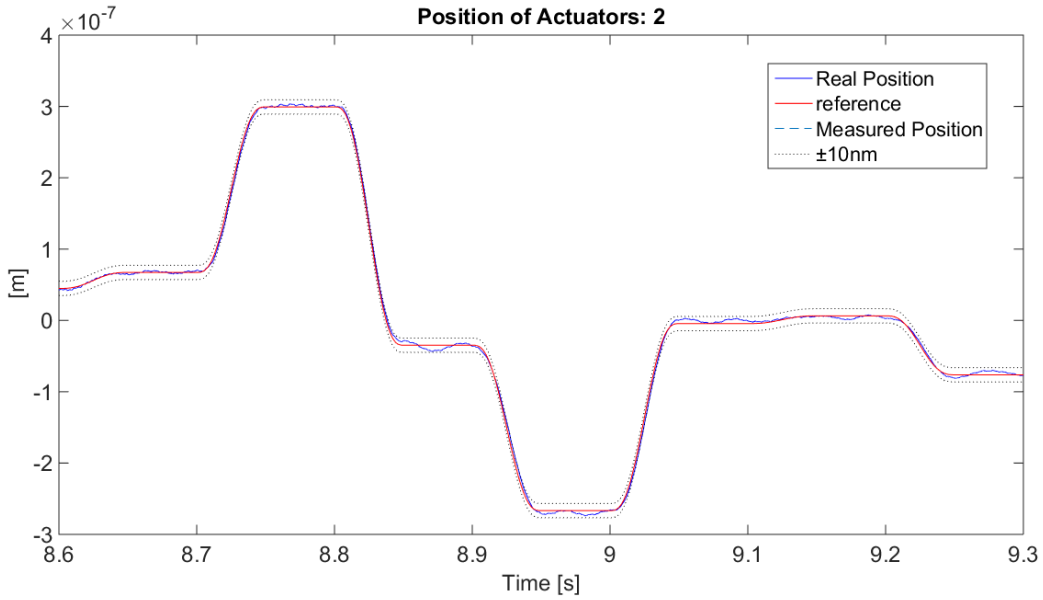

Figure 5.42: 17 Bits Digital Implementation - response

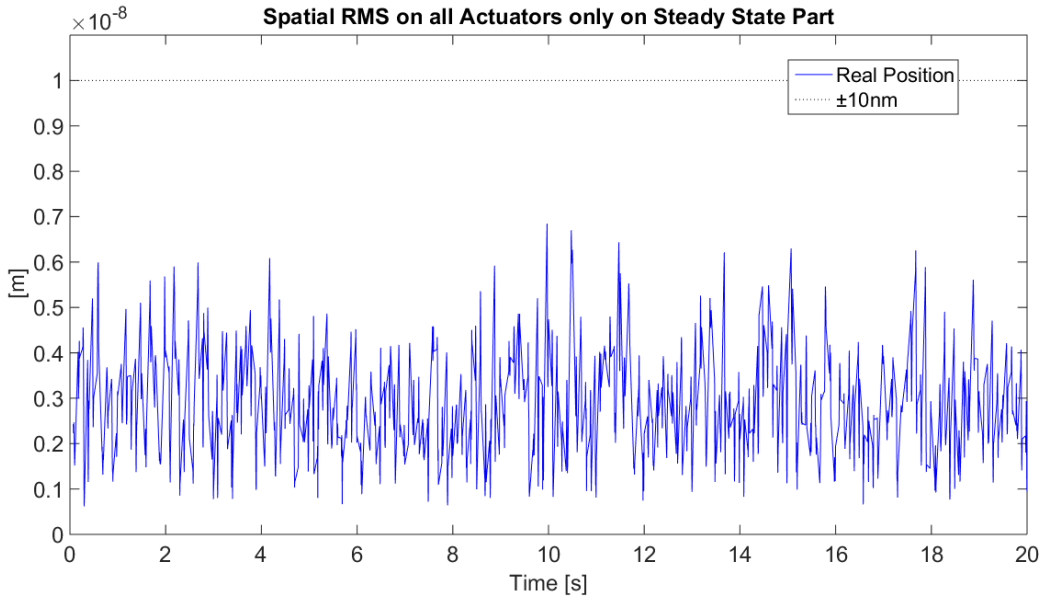

Figure 5.43: 17 Bits Digital Implementation - error rms on steady state step part

Solution	Processor	DA conv.	Sh.Filters	PD Circuits
Almost Fully Analog	10Hz	16 bits	45 OpAmps	45 OpAmps
Analog Feedback	400Hz $\leq$	16 bits	–	45 OpAmps
Fully Digital	2000Hz	17 bits $\leq$	–	–

Table 5.3: Comparative Components Budget

lution, considering the on-board processor frequency and its computational loads, the DA converters differences and the operational amplifiers number.

5.5 Off-Design Key Parameters Analysis

The final part of this work is related to simulations of the control system performance with off-design modeling parameters. Since the controller is designed upon a nominal dynamic model, it is worth studying the closed-loop response to variations of some parameters, in order to test the robustness of the solution. The goal of the present analysis is to check the effect of unavoidable uncertainties in the realization and implementation of the system and to get a measure of the closed-loop performance under off-design operational conditions.

The first analyzed parameter is the voice-coil efficiency η. This quantity is an overall property of the actuator summing up all the device parameters and represents a crucial characteristic to quantify the capability of the controlled system to damp out vibrations. As already mentioned its value changes with the amplitude of the gap between mirror and backplate, thus it is important to check the control effectiveness when moving from the nominal position.

An uncertainty is instead related to the value of structural damping of the mirror. Even though an exact measure of damping is difficult, we have shown that the modal damping ratios will have practically null values in the operating conditions of the telescope and thus should not significantly participate to the mirror stabilization. It is however safe verifying the absence of spillover effects in the high frequency range even with modified ξ values.

On the opposite side, it is also interesting to study the system response when both the natural and voice-coil induced damping have higher values compared to those used in the nominal model. This analysis could be useful

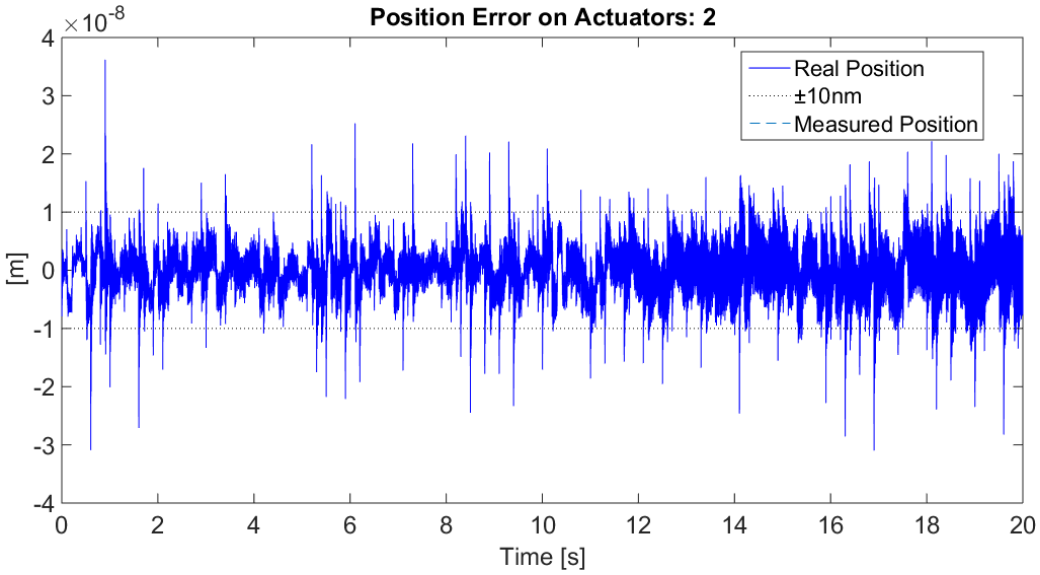

Figure 5.44: Test for $\eta = 0.35$ - error accumulation

in checking excessive dissipation effects, that could impede the system to promptly follow the reference position.

Finally, the whole design has been conducted on a FEM model of the mirror, that could be considered similar to the result of an identification process, thus presenting errors in modes and frequency. It is thus necessary to test the control design with modified dynamical characteristics, both in terms of $\mathbf{\Phi}_i$ and ω_i.

5.5.1 Voice-coil induced damping

The nominal value for the motor efficiency is set to $\eta = 0.4$, corresponding to the middle elongation position of the actuator. This value changes with the actuator stroke, so that upper and lower bounds can be identified. To span the whole set of possible working conditions, even when small changes in the actuators design occur, overestimated limit values have been considered. In particular, the upper and lower bounds have been set to $\eta = 0.5$ and $\eta = 0.35$, respectively.

The upper limit values present no great differences compared to the nominal value. The error levels are nearly identical and the closed-loop performance is still dominated by the quantization effect when a fully digital implementation is considered. Problems arise instead with a lower damping level. Indeed, control gains are the results of a design procedure based on an assumed damping assurance. The application of such gains to a system

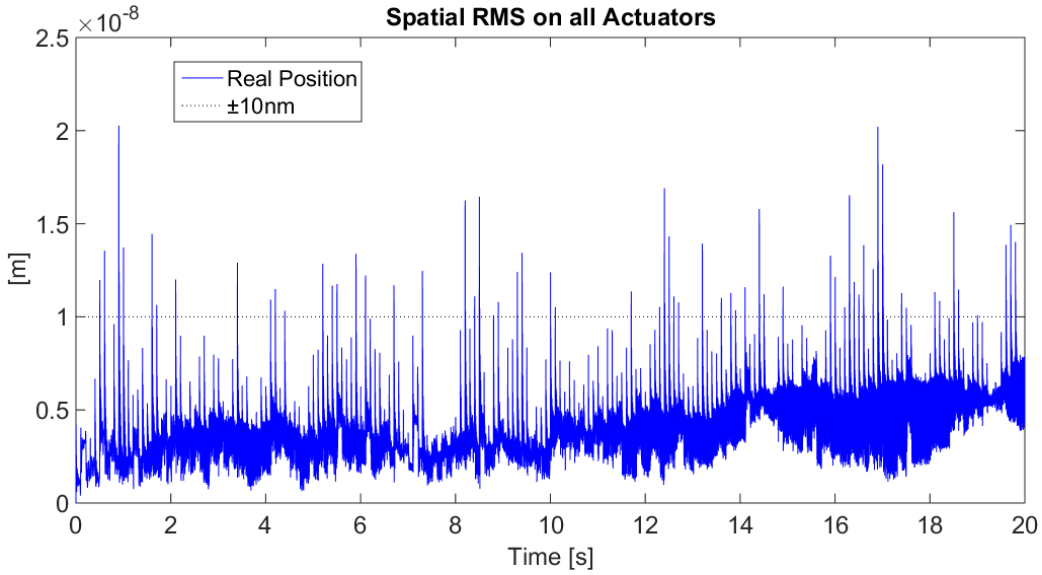

Figure 5.45: Test for $\eta = 0.35$ Test - rms error

K_P	$4737,6$
K_D	$8,9$

Table 5.4: Continuous Time Revised Gains

having a lower value of damping induces vibrations that are barely absorbed (see figures 5.44 and 5.45). This is due to the large and broad excitation of the mirror dynamics resulting from the adoption of a rather aggressive feedback control. When η assumes low values, the exciting dynamics is not sufficiently damped by the voltage-driven voice-coils.

In such a case, the solution could be to increase the weight related to the control effort in the definition of the cost function. A larger weighting of the control effort leads to a reduction of the control gains. If properly tuned, this reduction can be limited so that the closed-loop performance is still satisfactory, but the resulting design is more robust with respect to variations of the voice-coils efficiency. For example, a re-designed PD controller with the gains reported in table 5.4 shows a stable behavior in case of η reduction (figures 5.46 and 5.47) and still acceptable results in the nominal case (figure 5.48).

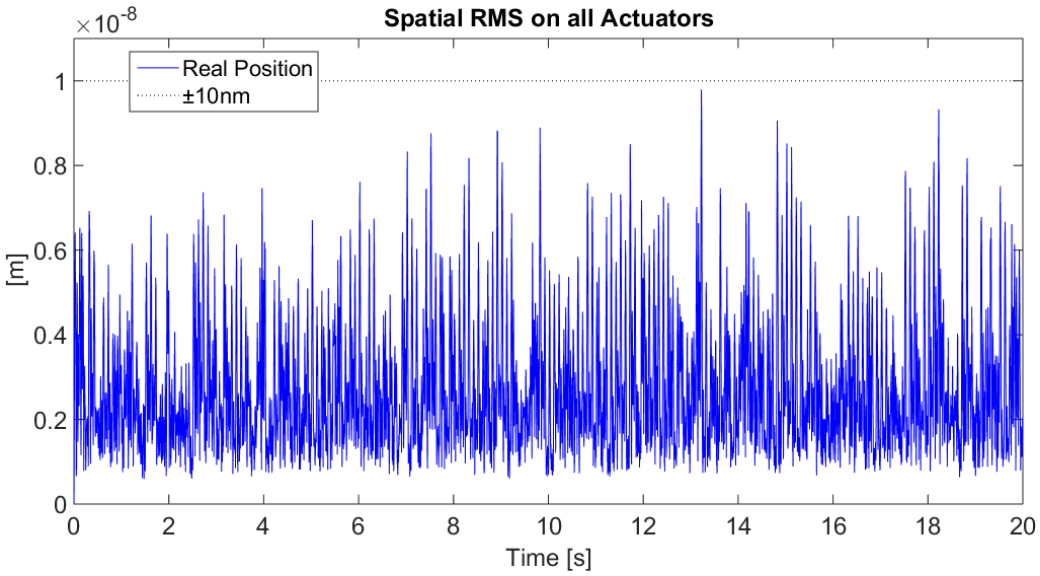

Figure 5.46: Revised Gains - rms error for $\eta = 0.35$ case

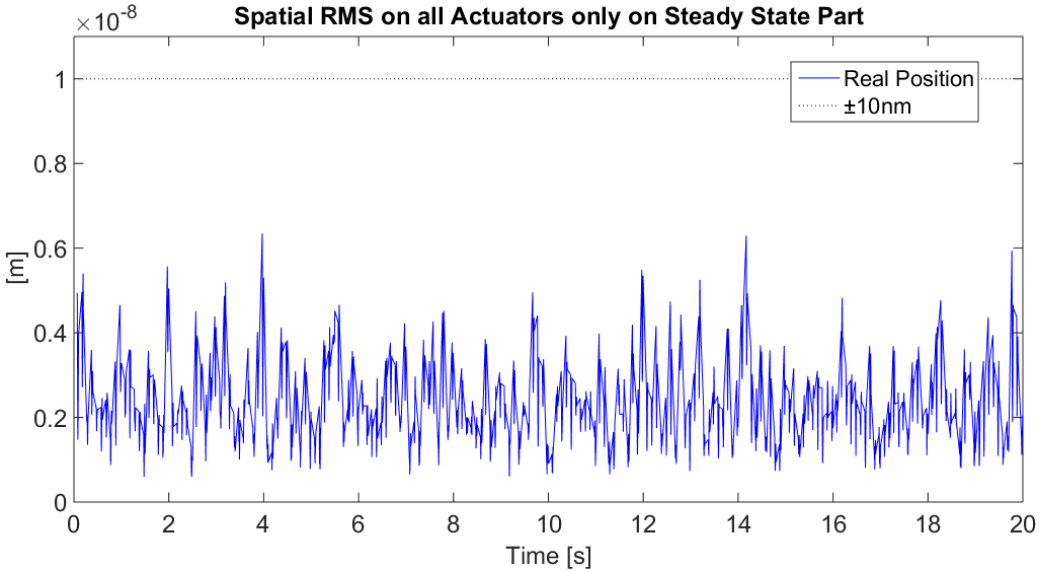

Figure 5.47: Revised Gains - steady state error rms for $\eta = 0.35$ case

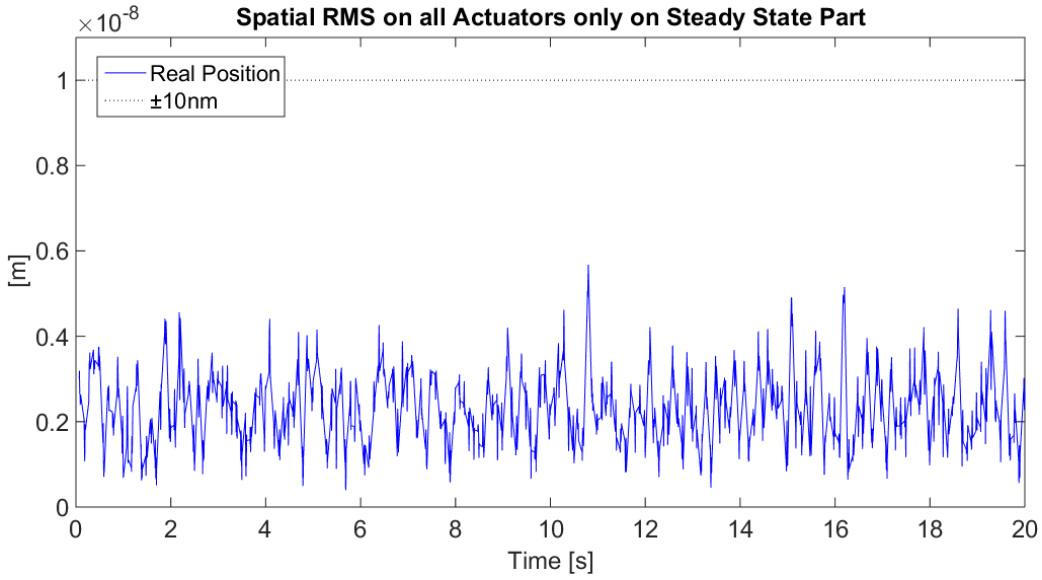

Figure 5.48: Revised Gains - steady state error rms for $\eta = 0.4$ case

5.5.2 Structural damping

The second parameter analyzed has been the structural damping ξ. It was assumed to study the effect of large variations, ranging from $\xi = 1.5835 \times 10^{-5}$ as best case to $\xi = 1.5835 \times 10^{-11}$ as worst case.

Both cases did not show substantial changes with respect to the nominal case. This could be due to the practically nihil damping that does not affect the system response. Indeed, the positioning performance and damping is guaranteed only by eddy currents associated to the voice-coil.

5.5.3 Modal Model

A robustness analysis was finally carried out by evaluating errors in the modal parameters of the mirror. To simulate such discrepancies, both modal shapes and frequencies have been corrupted for obtaining a slightly different dynamical model. This has been possible thanks to the direct availability of the mirror modal model.

A random deviation has been added to the natural frequencies. The intensity of such error has been regulated to obtain discrepancies between the design and simulation model in the order of 2% for the lower frequencies and up to 4% for the higher ones, as reported in figure 5.49. Such amount of inaccuracy in the knowledge of natural frequencies appears to be reasonable according to an usual modal testing procedure.

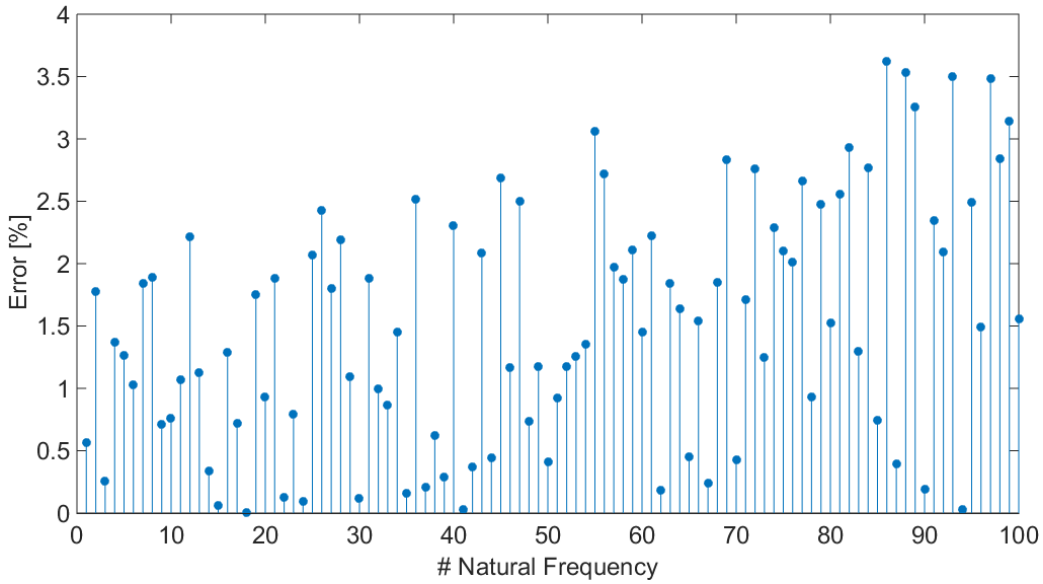

Figure 5.49: Error on natural frequencies

Instead, the introduction of a reasonable deviation for the modal shapes is less trivial. The following procedure has been devised. Random errors have been added to the eigenvector components. To quantify the effect of those errors and their plausibility, the Modal Assurance Criterion (MAC) has been adopted. The standard deviation of the error has been tuned until diagonal elements in the MAC matrix achieved values in the order of $0,90$. The matrix has been computed using the exact given modes and the corrupted ones and is reported in figure 5.50. This criterion is a geometrical similarity index and thus presents extra diagonal elements different from zero not only because of inserted errors, but also because modes are orthogonal only through the mass and stiffness matrix.

All the implementable solutions turned out to have a robust behavior, maintaining good performances along with the modified modal model. The only difference observed is the impossibility to reduce the frequency in the feedback analog solution down to 400Hz (figure 5.51). The limit frequency reachable is actually 900Hz.

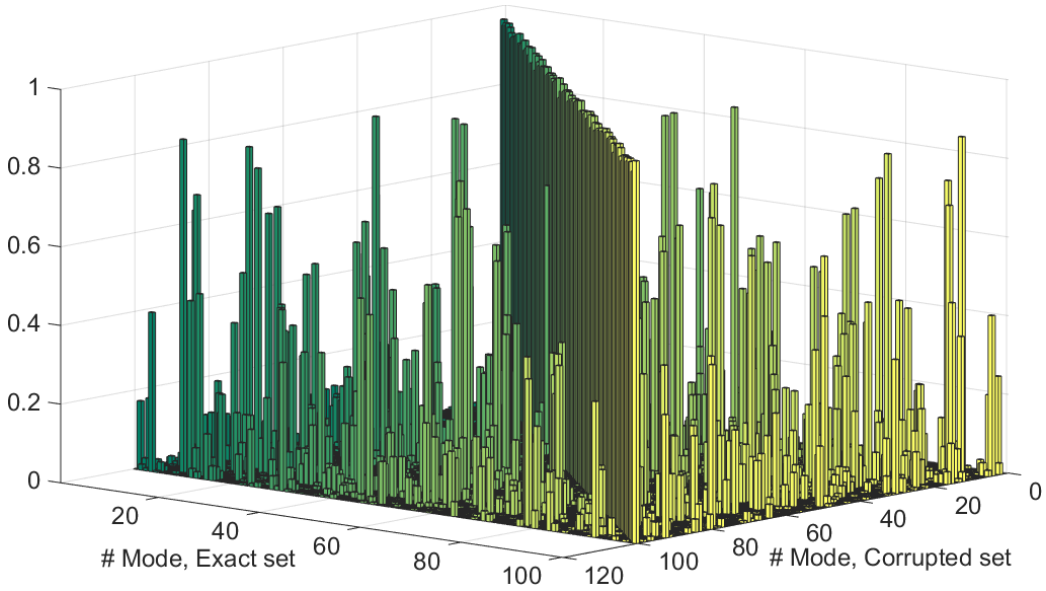

Figure 5.50: Modal Assurance Criterion

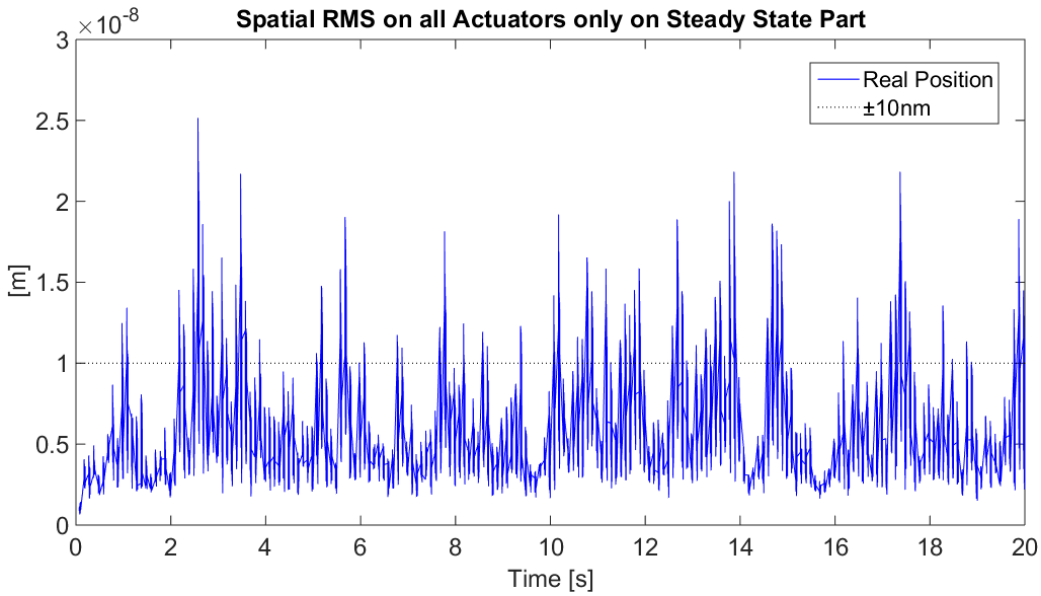

Figure 5.51: FB Analog Solution (400Hz sampled inputs) with corrupted modal model

Chapter 6

Final Remarks

This thesis work addresses the problem to transferring voice-coil actuation technology, developed for Earth based Active Optics, to space telescopes. This kind of actuation indeed exhibited good performance operating inside the atmosphere and this research proved its suitability also to an hypothetical secondary mirror for a space telescope.

For this purpose, the mirror modal model required a high number of modes to certify the absence of spillover in the high frequency range, but a reduced order model has been sufficient for the feedback control design, demonstrating the control capability to produce commands with limited frequency content.

Literature review revealed the practically nihil damping level existing in materials at cryogenic temperatures, that is the application condition of future space telescopes. Due to the impossibility to exploit aerodynamic damping arising from the squeezed air film between mirror and backshell, as it is done on Earth, it emerged the necessity to find an alternative to damp out vibrations.

Voice-coil voltage drive has been proposed and tested as solution. Simulations confirmed the net advantage in substituting current drive, required for high frequency responses, with the aforementioned alternative that revealed significant performances even with open loop control schemes. This proved possibility to exploit eddy currents to damp out vibrations.

Voltage drive and the consequent limited actuation bandwidth did not showed any interference with the control system promptness and confirmed also the validity of statically approximating the electric dynamics.

Along with these aspects, it has been also confirmed the effectiveness of the Hybrid feedforward control scheme developed during previous researches [8, 16, 17, 18]. Indeed, it has been possible limiting the vibration excitation of the optical surface using dynamic compensation terms and, at

the same time, eroding the static positioning errors, arising from uncertainties in the feedforward stiffness matrix, thanks to the hidden integral action.

Precise correction of typical optical aberrations has been obtained by supporting the Hybrid feedforward with a suboptimal decentralized static output feedback. ESA requests in terms of high demanding positioning precision and command frequency thus have been fulfilled.

Three implementable solutions have been proposed. From these latter it can be inferred the necessity to use analog components to express even the fine feedback voltage or, alternatively, to rely on DA converters with a higher number of bits.

The actuation technology and the control system designed showed good performances even under modeling uncertainties and off-design operational conditions, highlighting thus the solution robustness.

Further developments could include advancements of the digital control hardware to enhance its capability of expressing even the finer feedback action.

Dealing with the control project, it could be instead interesting including in the optimization process also other system parameters, like filters bandwidth, to obtain a globally optimal performance. In addition, more complex and daring structures could be adopted for the gain matrix, looking for a trade off between control performances and practical realization.

Finally, another investigation aspect could be the synthesis and test of voltage-driven voice-coil technology, along with the proposed control scheme, also for other mirrors with different sizes, materials and number of actuators.

Bibliography

[1] Marie Laslandes, Claire Hourtoule, Emmanuel Hugot, Marc Ferrari, Céline Lopez, Christophe Devilliers, Arnaud Liotard, and Frederic Chazallet. "Space active optics: performance of a deformable mirror for in-situ wave-front correction in space telescopes". In: *Proc. SPIE* 8442 (2012).

[2] Mauro Manetti, Marco Morandini, and Paolo Mantegazza. *Control System Design of Active Primary Mirror for the Advanced LIDAR Concept Satellite*. Politecnico di Milano, 2007.

[3] David C. Redding, Gregory Hickey, G. Agnes, P. Eisenhardt, J.J. Green, J. Krist, L. Peterson, K. Stapelfeldt, W. Traub, S. Unwin, and Werner M. *Active Optics for a 16-Meter Advanced Technology Large Aperture Space Telescope*. Jet Propulsion Laboratory, 2008.

[4] Marie Laslandes, Emmanuel Hugot, Marc Ferrari, Claire Hourtoule, Christian Singer, Christophe Devilliers, Céline Lopez, and Frédéric Chazallet. "Mirror actively deformed and regulated for applications in space: design and performance". In: *Optical Engineering* 52.9 (2013).

[5] Alessandro Zuccaro Marchi, Pascal Hallibert, Joao Pereira do Carmo, and Eric Wille. "Active optics for space applications: an ESA perspective". In: *Proc. SPIE* 9151 (2014).

[6] Christopher J. Burrows, Jon A. Holtzman, S.M. Faber, Pierre Y. Bely, Hashima Hasan, C.R. Lynds, and Daniel Schroeder. "The imaging performance of the Hubble Space Telescope". In: *The Astrophysical Journal* 369 (1991), pp. L21–L25.

[7] Jonathan P. Gardner, John C. Mather, Mark Clampin, Rene Doyon, Matthew A. Greenhouse, Heidi B. Hammel, John B. Hutchings, Peter Jakobsen, Simon J. Lilly, Knox S. Long, Jonathan I. Lunine, Mark J. Mccaughrean, Matt Mountain, John Nella, George H. Rieke, Marcia J. Rieke, Hans-Walter Rix, Eric P. Smith, George Sonneborn, Massimo Stiavelli, H.S. Stockman, Rogier A. Windhorst, and Gillian S. Wright.

"The James Webb Space Telescope". In: *Space Science Reviews* 123.4 (2006), pp. 485–606.

[8] Mauro Manetti. "High precision shape control of massively actuated, magnetically levitated, secondary adaptive mirrors for extremely large telescopes". Phd Thesis. Politecnico di Milano, 2010.

[9] J. W. Hardy, J. E. Lefebvre, and C. L. Koliopoulos. "Real-time atmospheric compensation". In: *JOSA* 67.3 (1977), pp. 360–369.

[10] Warren P. Mason. "Piezoelectricity, its history and applications". In: *The Journal of the Acoustical Society of America* 70.6 (1981), pp. 1561–1566.

[11] D. Damjanovic and R.E. Newnham. "Electrostrictive and piezoelectric materials for actuator applications". In: *Journal of Intelligent Material Systems and Structures* 3.2 (1992), pp. 190–208.

[12] Madec P.Y. "Overview of deformable mirror technologies for adaptive optics and astronomy". In: *Proc. SPIE* 8447 (2012), pp. 5–18.

[13] Roberto Biasi, Daniele Gallieni, Piero Salinari, Armando Riccardi, and Paolo Mantegazza. "Contactless thin adaptive mirror technology: past, present, and future". In: *Proc. SPIE* 7736 (2010).

[14] *Announcement of Opportunity: Active Optics correction chain for large monolithic mirrors*. European Space Agency. 2014.

[15] Mauro Manetti, Marco Morandini, and Paolo Mantegazza. "High precision massive shape control of magnetically levitated adaptive mirrors". In: *Control Engineering Practice* 18.12 (2010), pp. 1386–1398.

[16] Mauro Manetti, Marco Morandini, and Paolo Mantegazza. "Self-Tuning Shape Control of Massively Actuated Adaptive Mirrors". In: *IEEE Transactions on Control Systems Technology* 22.3 (2014), pp. 838–852.

[17] Mauro Manetti, Marco Morandini, Paolo Mantegazza, Roberto Biasi, Daniele Gallieni, and Armando Riccardi. "Modeling and control of massively actuated, magnetically levitated, adaptive mirrors". In: *IEEE International Conference on Control Applications*. 2010, pp. 860–866.

[18] Mauro Manetti, Marco Morandini, Paolo Mantegazza, Roberto Biasi, Daniele Gallieni, and Armando Riccardi. "Experimental validation of massively actuated deformable adaptive mirror numerical models". In: *Control Engineering Practice* 20.8 (2012), pp. 783 –791.

[19] *SCHOTT, glass made of ideas*. URL: `http://www.schott.com/`.

[20] R.J. Guyan. "Reduction of stiffness and mass matrices". In: *AIAA Journal* 3.2 (1965), p. 380.

[21] Roy R. Craig Jr. and Mervyn C.C. Bampton. "Coupling of substructures for dynamic analyses". In: *AIAA Journal* 6.7 (1968), pp. 1313–1319.

[22] Sondipon Adhikari. "Damping models for structural vibration". PhD thesis. University of Cambridge, 2001.

[23] Marie B. Levine and Christopher White. "Material damping experiments at cryogenic temperatures". In: *Optical Science and Technology, SPIE's 48th Annual Meeting*. International Society for Optics and Photonics. 2003, pp. 165–176.

[24] Chia-Yen Peng, Marie B. Levine, Lillian Shido, and Robert S. Leland. "Experimental observations on material damping at cryogenic temperatures". In: *Optical Science and Technology, the SPIE 49th Annual Meeting*. International Society for Optics and Photonics. 2004, pp. 44–62.

[25] C. Peng, M. Levine, L. Shido, M. Jacoby, and W. Goodman. "Measurement of vibrational damping at cryogenic temperatures for silicon carbide foam and silicon foam materials". In: *Proc. SPIE* 5868 (2005).

[26] Alain C. Carrier, Bruce Romney, and Roger Mihara. "Damping characteristics of composite petal structure for an 8-m diameter telescope at cryogenic temperature". In: *Proc. SPIE* 5487 (2004), pp. 1066–1083.

[27] Bill Black, Lopez Mike, and Anthony Morcos. "Basics of Voice Coil Actuators". In: *PCIM* (1993).

[28] N. Wavre and X. Thouvenin. "Voice-coil actuators in space". In: ESA Special Publication 374 (1995). Ed. by W. R. Burke, p. 227.

[29] S. Adhikari and J. Woodhouse. "Identification of Damping: part 1, viscous damping". In: *Journal of Sound and Vibration* 243.1 (2001), pp. 43 –61.

[30] Huibert Kwakernaak and Raphael Sivan. *Linear optimal control systems*. Wiley-interscience, 1972.

[31] Federico Fonte, Sergio Ricci, and Paolo Mantegazza. "Gust Load Alleviation for a Regional Aircraft Through a Static Output Feedback". In: *Journal of Aircraft* (2015).

[32] J. Nocedal and S. Wright. *Numerical Optimization*. New York: Springer, 2006.

[33] *Matlab Guide: Unconstrained Nonlinear Optimization Algorithms*. URL: `http://it.mathworks.com/help/optim/ug/unconstrained-nonlinear-optimization-algorithms.html`.

[34] C.C. Lin, K.H. Lu, and L.L. Chung. "Optimal discrete-time structural control using direct output feedback". In: *Engineering Structures* 18.6 (1996), pp. 472 –480.

[35] Shih-Yu Chu, Chi-Chang Lin, Lap-Loi Chung, Chang-Ching Chang, and Kuo-Haw Lu. "Optimal performance of discrete-time direct output-feedback structural control with delayed control forces". In: *Structural Control and Health Monitoring* 15.1 (2008), pp. 20–42.

[36] Rolf Isermann. *Digital control systems - Volume 2 : Stochastic control, multivariable control, adaptive control, applications*. 2nd Edition. Berlin: Springer-Verlag, 1991.

[37] Robert E. Skelton, Karolos M. Grigoriadis, and Tetsuya Iwasaki. *A unified algebraic approach to linear control design*. London: Taylor and Francis, 1998.

[38] Gene F. Franklin and Powell J. David. *Digital control of dynamic systems*. USA: Addison-Wesley, 1980.

[39] John D. Johnston, Joseph M. Howard, Gary E. Mosier, Keith A. Parrish, Mark A. McGinnis, A. M. Bluth, Kevin Kim, and Kong Q. Ha. "Integrated modeling activities for the James Webb Space Telescope: structural-thermal-optical analysis". In: *Proc. of SPIE*. Vol. 5487. 2004, pp. 600–610.

[40] Gianantonio Magnani, Gianni Ferretti, and Paolo Rocco. *Tecnologie dei sistemi di controllo*. 2nd Ed. Milano: McGraw-Hill, 2007.

[41] Karl J. Åström and Tore Hägglund. *Advanced PID control*. USA: Instrumentation, Systems, and Automation Society, 2006.